Task 3 Final Report
Windborne Debris Study
Contract Number 12-00005-00

Presented to the

Florida Building Commission
State of Florida Department of Business and Professional Regulation

by

Forrest J. Masters, Ph.D., P.E., masters@ce.ufl.edu, (352) 392-9537 x 1505
Kurtis R. Gurley, Ph.D., kgurl@ce.ufl.edu, (352) 392-9537 x 1508
David O. Prevatt, Ph.D., P.E. (MA), dprev@ce.ufl.edu, (352) 392-9537 x 1498

Graduate Students:

Brian Rivers
Audra Kiesling

Engineering School for Sustainable Infrastructure & Environment
University of Florida

1.1. Deliverables

The Contractor shall perform research related to rain deposition on the building façade. This research component will support the American Society of Civil Engineers (ASCE) Task Committee on Wind-Driven Rain Effects, which is developing serviceability requirements for wind-driven rain penetration resistance of buildings. The Committee is writing a report that provides guidelines for the design and installation of building products and systems intended to prevent water ingress from wind-driven rain. These guidelines will assist the practitioner in determining combinations of pressure loads and wetting requirements for these systems. The contractor is authorized to spend up to $85,863 on this task. This support may be used as matching funds for future grant proposals with a wind-driven rain focus. The Contractor shall submit the final ASCE report plus any supplemental information about project activities, as required.

2. Summary of Activities for Task 3

Dr. Masters is the chair of the ASCE Task Committee on Wind-Driven Rain Effects, which is part of the Technical Council on Wind Engineering. The purpose of this committee is to develop a first-of-its-kind report on the wind-driven rain effects, which will presumably become an ASCE monograph. The report not only contains the necessary information for future guidelines, but also provides a thorough overview of past work completed in wind-driven rain research. Wind driven rain research has been conducted for well over a half century, however, a comprehensive overview detailing the progress in this area has yet to be compiled. While the primary objective is to protect the built environment through engineering and construction methods, the report also provides detail of the meteorological aspects of wind-driven rain and the associated climatology. The primary research areas were identified: testing, simulation, data collection, and climatology, and previous works are summarized and combined to produce an in-depth review of these research topics. This report and an appendix summarizing research performed as part of the FY2012-13 scope of work are appended to this document.

In Fall 2012, a draft of the document was organized and reviewed to determine which subject areas were lacking in content or depth in order to identify areas of research that could be enhanced through testing. Experts in fields of meteorology, engineering, and building science were consulted for their expertise in content areas that called for highly specialized experience or research. Multiple areas of research were identified to enhance understanding and provide definitive results for addition to the report. One area of particular interest identified during the compilation of the ASCE wind driven rain report was the issue of water ingress through fenestration, especially residential windows. It was determined that a testing apparatus could be devised and constructed to shed light on this issue. The 2nd generation HAPLA, was redesigned to operate more efficiently and in a smaller area. The HAPLA was also modified to use a rain rack capable of variable rainfall intensities to simulate precipitation during hurricane wind loading conditions (development was funded from a different grant). Specimens were subjected to dynamic pressure loads and time-varying wind-driven rain conditions (a first). The load is fluctuated using a valve, which incorporates a servo motor to restrict the amount of air entering and exiting the system. The test chamber is an 8 ft. X 8 ft. x 2 ft. steel box which clamps the specimen against an air tight gasket. Inside the test chamber is a rain rack, which is a grid of evenly spaced nozzles, to simulate the rainfall at the rate appropriate for the given test. The amount of water passing through the window was collected in a container supported by a load cell, which was continuously monitored to capture the rate of ingress.

We anticipate the report will be submitted to ASCE by August 15 for outside peer-review. The research funded by this project is essentially complete. The end of the performance period nearly coincides with the defense date of the graduate student that performed the work described above. The Contractor will provide a copy of the final thesis to the program manager, if requested.

This copy of the report was produced expressly for the final report for a grant sponsored by the Florida Building Commission.

It is not the final copy that ASCE will publish, and is not intended for use by the public.

Wind-Driven Rain Effects on Buildings

Prepared by the

Task Committee on Wind-Driven Rain Effects
Environmental Wind Engineering Committee
Technical Council on Wind Engineering
American Society of Civil Engineers

Forrest J. Masters, Ph.D., P.E., M. ASCE (Ed.)

Acknowledgments

The organizers of this report are grateful for the support provided by ASCE to assemble this document. The Committee would also like to acknowledge the institutions that sponsored the research described herein, which include the Commonwealth Scientific and Industrial Research Organisation (CSIRO; Australia), the Division of Civil, Mechanical and Manufacturing Innovation (CMMI) at the National Science Foundation, the Florida Building Commission, the Florida Catastrophic Risk Management Center, the FWO-Flanders Fund for Scientific Research (Belgium), the Insurance Institute for Business & Home Safety (IBHS), and the State of Florida Division of Emergency Management.

List of Committee Members

The individuals serving on the Task Committee are:

1. Forrest J. Masters, Ph.D., P.E., M. ASCE, *Chair*
2. Paul Beers, M. ASCE
3. Bert Blocken, M. ASCE
4. Jan Carmeliet, Ph.D.
5. Arindam G. Chowdhury, Ph.D., M. ASCE
6. Anne D. Cope, Ph.D., P.E., M. ASCE
7. Thang Dao, Ph.D., M. ASCE
8. Yarrow Fewless, M. ASCE
9. Chuck Goldsmith, AIA, M.ASCE
10. Eric Haefli, M. ASCE
11. Anurag Jain, P.E., M. ASCE
12. Greg A. Kopp, Ph.D., P.Eng., M. ASCE
13. Michael Lacasse, M. ASCE
14. Jean-Paul Pinelli, P.E., M. ASCE
15. Timothy A. Reinhold, Ph.D., P.E., M. ASCE
16. Tom Smith, AIA, M. ASCE
17. Ted Stathopoulos, Ph.D., P.Eng., F. ASCE
18. S. Jeffrey Underwood, Ph.D.
19. John van de Lindt, Ph.D., P.E., M.ASCE
20. Peter J. Vickery, Ph.D., P.E., M. ASCE
21. Mark F. Williams, P.E., M. ASCE

The committee would also like to thank the following graduate students for their contributions and assistance writing this report:

- Audra Kiesling
- Brian Rivers

Glossary of Terms

Many fields study wind-driven rain, including wind engineering, meteorology and building science. Symbols and terminology vary in the literature, even within a single discipline; therefore a consistent set of notations was adopted for this report. Table 1.1 contains symbols and acronyms used herein. Alternative definitions are provided, where appropriate.

Table 1.1. Notation adopted in this report

Roman symbols

a	Parameter describing the logarithmic wind profile	
a_i	Weighting factor for time step i	-
b	Parameter in raindrop-size distribution of Best	mm
c	Integration constant	m/s
d	Raindrop diameter	mm
d_{LIMIT}	Limit base diameter for runoff	mm
d_{SPD}	Surface-pendent-drop base diameter	mm
d_{TRACE}	Diameter of trace droplets	mm
e_{AVG}	Averaging error	-
e_{wdr}	Wind-driven-rain error for the ratio Swdr/Sh	-
f(d)	Probability density of raindrop size (in air volume)	m^{-1}
$f_h(d)$	Probability density of raindrop size (through a horizontal plane)	m^{-1}
g	Gravitational constant	m/s^2
h	Reference grid spacing	m
h_e	Exterior surface heat-transfer coefficient	W/m^2K
h_i	Interior surface heat-transfer coefficient	W/m^2K
h_{IBL}	Height of the internal boundary layer (IBL)	m
k	Turbulent kinetic energy	m^2/s^2
k_P	Turbulent kinetic energy at point P	m^2/s^2

k_s	Physical roughness height	m
k_s^+	Non-dimensional physical roughness height	-
l	Mixing length	m
m	Parameter in raindrop-size distribution of Best	-
n	Number of terms	-
p	Instantaneous pressure	Pa
p	Order of the discretization scheme	-
p_c	Capillary pressure	Pa
p_e	Exterior vapour pressure	Pa
p_i	Interior vapour pressure	Pa
q	Parameter in raindrop-size distribution of Best	-
s_{TRACE}	Spacing between trace droplets	m
t	Time	s
y	Co-ordinate normal to the wall	m
y_0	Aerodynamic roughness length	m
y_P	Distance from point P to the wall	m
y_{ref}	Reference height	m
y *	Dimensionless wall co-ordinate y-star	-
y^+	Dimensionless wall co-ordinate y-plus	-
y_0^+	Largest roughness length	m
y_v	Physical thickness of the viscous sub-layer	m
y_v*	Dimensionless physical thickness of the viscous sub-layer	-
u, v, w	x, y and z component of the instantaneous wind-velocity vector	m/s
u', v', w'	Fluctuating part of u, v, w	m/s
u_τ	Friction velocity in wall function log-law (u-tau)	m/s
u*	Friction velocity in wall function log-law (u-star)	m/s

u^*_{ABL}	Friction velocity in ABL log-law	m/s
u+	Dimensionless fluid speed	-
v_x, v_y, v_z	x, y and z component of raindrop-velocity vector	m/s
x, y, z	Cartesian co-ordinates	m
z_b	Aspect (azimuth) of sloping soil surface	°
z_g	Direction from which the rain is coming	°

A	Size of collection area	m^2
A	Exponential roughness function	-
A1, A2	Constants	
A_d	Equivalent frontal area (based on equivalent diameter) of a raindrop	m^2
A_f	Area on a building facade	m^2
$A_f(d)$	Area on a building facade bounded by the end positions of raindrops of diameter d	m^2
A_g	Area of a horizontal surface at ground level	m^2
A_h	Area of a horizontal surface at a certain height above ground	m^2
$A_h(d)$	Area of a horizontal surface bounded by the injection positions of raindrops of diameter d	m^2
A_s	Area of a sloping soil surface	m^2
B	Width	m
B	Constant in logarithmic law-of-the-wall	-
C_1 … C_6	Integration constants	-
$C_{1\varepsilon}$, $C_{2\varepsilon}$	Constants/parameters in standard and realizable k-e turbulence model	-
C_d	Drag coefficient	-
C_s	Roughness constant	-
C_μ	Parameter in k-ε turbulence model	-

D	Magnitude of drag force	N
E	Empirical constant for wall roughness in wall function	-
E_{wdr}	Wind-driven-rain error	mm
F(d)	Fraction of liquid water in air with raindrops of diameter < d	-
G_k	Production of turbulent kinetic energy	kg/ms^3
H	Height	m
H	Higher order terms	
I_A	Airfield annual index	mm
I_S	Airfield spell index	mm
I_{WA}	Wall annual index	mm
I_{WS}	Wall spell index	mm
L	Length	m
M	Parameter in raindrop-size distribution of Best	-
O	Obstruction factor	-
P	Mean pressure	Pa
P	Centre point of the wall-adjacent cell	
R	Terrain roughness factor	-
R	Rain intensity	mm/h
R0	Meteorological rain intensity	mm/h
R*	Hydrological rain intensity	mm/h
R_h	Horizontal rainfall intensity	mm/h
$R_h(d)$	Specific horizontal rainfall intensity	mm/h
R_{wdr}	Wind-driven-rain intensity	mm/h
$R_{wdr}(d)$	Specific wind-driven-rain intensity	mm/h
Re	Reynolds number	-
Re_y	Local wall-based Reynolds number	-

Re_R	Relative Reynolds number	-
S	Rain sum	mm
S0	Meteorological rain sum	mm
S*	Hydrological rain sum	mm
S_{AREA}	Size of square areas on the collection surface	m^2
S_h	Horizontal rainfall sum	mm
$S_h(d)$	Specific horizontal rainfall sum	mm
S_{ij}	Mean strain rate	s-1
S_T	Modulus of the mean rate-of-strain tensor	s-1
S_{wdr}	Wind-driven-rain sum	mm
$S_{wdr}(d)$	Specific wind-driven-rain sum	mm
$S_{wdr\ AVG}$	Wind-driven-rain sum obtained based on averaged data	mm
$S_{wdr\ REF}$	Wind-driven-rain sum in the reference solution	mm
T	Topography factor	-
T_e	Exterior air temperature	K
T_i	Interior air temperature	K
T_{wdr}	Rainwater temperature	K
U, V, W	x, y, z component of mean wind-velocity vector	m/s
U	Mean streamwise horizontal wind speed (in x-direction)	m/s
$\tilde{U}$	Mean wind speed sensitised to pressure gradient	m/s
U_0	Reference wind speed	m/s
U_{avg}	Mean wind speed averaged along a vertical line	m/s
U_H	Reference wind speed at height H	m/s
U_{10}	Reference wind speed at 10 m height	m/s

U_P	Mean wind speed at point P	m/s
U_{ref}	Reference mean wind speed	m/s
U_{REL}	Relative mean wind speed (relative speed of air around a raindrop)	m/s
U_T	Fluid speed tangential to the wall	m/s
U_{WT}	Wind-tunnel speed	m/s
V_{SPD}	Surface-pendent-drop water volume	m^3
V_t	Terminal velocity of fall of a raindrop	m/s
W	Wall factor	-
Z	Resultant horizontal component of mean wind speed (not necessarily streamwise)	m/s

$\mathbf{g}$	Gravitational vector	m/s^2
$\mathbf{r}$	Position vector of a raindrop	m
$\mathbf{v}$	Instantaneous wind-velocity vector	m/s
$\mathbf{v}_{\mathbf{drop}}$	Raindrop-velocity vector	m/s

$\mathbf{D}$	Drag force	N
$\mathbf{G}$	Gravity force	N
$\mathbf{F}_{\mathbf{ARCH}}$	Archimedes force	N
$\mathbf{R}$	Rain-intensity vector	mm/h
$\mathbf{R}_{\mathbf{d}}$	Specific rain-intensity vector	mm/h

Greek symbols

α	(Adapted) Wind-driven-rain coefficient	s/m
α_P	Power-law exponent	-
$\alpha_{k,l}$, $\beta_{k,l}$, $\gamma_{k,l}$	Coefficients for catch-ratio interpolation	
β	Local inclination of sloping soil surface	°
β_e	Exterior surface vapour-transfer coefficient	s/m
β_i	Interior surface vapour-transfer coefficient	s/m
γ	Raindrop trajectory angle	°
γ_a	Advancing contact angle	°
γ_r	Receding contact angle	°
γ_s	Contact angle of a sessile drop on a horizontal surface	°
δ_{ij}	Kronecker delta	-
δU	Relative error in wind speed U	
ε	Turbulence dissipation rate	m^2/s^3
ε_h^d	Discretisation error	
ς	Factor in Taylor series expansion	
η	Catch ratio	-

η_d	Specific catch ratio	-
η_{free}	Free-field catch ratio	-
θ	Angle between wind direction and normal to the wall	°
κ	von Karman constant	-
κ_{wdr}	(Free) Wind-driven-rain coefficient	s/m
μ	Dynamic molecular viscosity	kg/ms
μ_t	Dynamic turbulent viscosity	kg/ms
ν	Kinematic molecular viscosity	m^2/s
ξ	Scalar variable (instantaneous)	
ξ'	Scalar variable (fluctuating part)	
ρ	Air density	kg/m^3
ρ_w	Water density	kg/m^3
σ_k	Turbulent Prandtl number for k	-
σ_ε	Turbulent Prandtl number for ε	-
σ_u	Standard deviation of turbulent fluctuations	m/s
τ_h	Truncation error on a mesh with reference spacing h	
τ_w	Wall shear stress	N/m^2

ϕ, Φ	Wind direction (degrees from north)	°
ϕ_h	Exact solution of discretized equations on a mesh with reference spacing h	

ΔB	Roughness function	-
Δt	Time step	s
Δt^e	Experimental time step	s
Δt^n	Numerical time step	s
Δx	Mesh spacing in x-direction	m
Δy	Mesh spacing in y-direction	m
Ξ	Scalar variable (mean)	
Φ	Exact solution of the differential or integral equations	

Subscripts

i, j, k, l, m, n	Counters	
i	Number of experimental time step	
j	Number of numerical time step	

Operators

div	Divergence operator	
grad	Gradient Operator	

Λ	Symbolic operator representing the exact solution of a system of equations	
L_h	Symbolic operator representing the algebraic equation system that results from discretisation of a system of equations on a mesh with reference spacing h	

Greek Symbol	**Name**	**Alternate Definitions**
η_d	Specific Catch Ratio	Local Effect Factor (LEF)
η	Catch Ratio	Local Intensity Factor (LIF)
Acronym	**Name**	**Alternate Definitions**
ABL	Atmospheric Boundary Layer	
BBRI	Belgian Building Research Institute	
BRE	Building Research Establishment	
BS	British Standard	
BSI	British Standards Institution	
BLWTL	Boundary Layer Wind Tunnel Laboratory	
BRS	Building Research Station	
CEN	European Committee for Standardization	
CFD	Computational Fluid Dynamics	
CIB	International Council for Research and Innovation in Building and Construction	
CSTB	Centre Scientifique et Technique du Bâtiment	
CTH	Chalmers University of Technology	
CV	Control Volume	
HAM	Heat-Air-Moisture Transfer Model	

HWA	Hot-Wire Anemometry	
LDA	Laser-Doppler Anemometry	
LOW	Law Of the Wall	
MRE	Multiple Rain Events	
NBRI	Norwegian Building Research Institute	
PMMA	PolyMethylMetAcrylate	
PTFE	PolyTetraFluoroEthylene	
PVC	PolyVinylChloride	
PWA	Pulsed-Wire Anemometry	
QUICK	Quadratic Upwind Interpolation for Convective Kinematics	
SIMPLE	Semi-Implicit Method for Pressure-Linked Equations	
SRE	Single Rain Event	
TUD	Technical University of Denmark	
TUE or TU/e	Eindhoven University of Technology	
WDR	Wind-Driven Rain	Driving Rain
WMO	World Meteorlogical Organisation	

Others		
----	Ensemble averaging or time averaging	

Chapter 1. Impact of Wind-Driven Rain on the Built Environment

Authors: Cope, Masters

Wind-driven rain is a complex interaction between individual raindrops of varying size and a wind-field varying in time and space, which in turn, influences the trajectory of the drops. The behavior of the driving rain is further complicated by local climate, topography, geometry of the building, and the location of the raindrops impinging on the building façade.

Wind-driven rain has had significant impacts on the built environment, particularly the building facade. When the exterior barrier is compromised, intrusion of wind-driven rain into the interior of the building can lead to mold, mildew and destruction of the contents inside. While significant improvements to the wind resistance of structures due to more stringent building codes following Hurricane Andrew in 1992, damage to structures due to water infiltration is still a recurring problem.

The aesthetics of a building are at risk from wind-driven rain due to soiling, discoloration, and staining of the building facade. When chemicals or minerals are present, either in the precipitation, or dispersed by the façade, efflorescence may occur, sometimes permanently staining the facade. As architectural styles evolve, the complexities of surface runoff increase, requiring more attention by designers to provide effective drainage plans to deter deterioration of the aesthetic quality of a structure.

While the need for guidance in designing for the effects of wind-driven rain has been recognized by architects and engineers in recent decades, a cohesive set of standards has not been produced. Wind-driven rain has multiple aspects which contribute to its deterioration of structures, many of which continue to be active areas of research in building science. The meteorological aspects of the phenomenon must be understood; therefore a satisfactory database of measurements and event specific data must be compiled to allow for comparison with prediction models. Water ingress through the building envelope must be understood on both a macroscopic and microscopic scale to determine the modes of water transport through the façade which allow for damage to the building's interior and contents. Scale model experiments and numerical methods need to be validated and refined to ensure their accuracy in predicting the wind-driven rain loads on a façade. All of the aforementioned areas are interrelated and rely on each other to provide data, means for validation and more advanced models. The many different aspects of wind-driven rain and its impact on the built environment must be taken into account in order to provide adequate guidance.

The purpose of this report is to provide in-depth overview of wind-driven rain impact on the built environment. This includes forming a basic understanding of hydrology, along with fundamental principles of meteorology to understand the origin and behavior of precipitation in its many forms. Climatology and atmospheric science are also briefly reviewed to elaborate on the type of meteorological event causing a building to be at risk of adverse effects from wind-driven rain. The built environment also has significant effects on the behavior of the wind-driven rain approach flow. The effects of the terrain and surrounding structures have been accounted for in different forms; a discussion of full-scale experiments conducted, semi-empirical models, and numerical methods is included. Along with a fundamental understanding of the behavior of wind-driven rain, this report provides guidance for practitioners and designers, as well as suggestions in the development of curriculum for continuing education and graduate engineering courses.

Chapter 2. Precipitation Systems

Authors: Underwood

2.1 Introduction

In undertaking the task of describing precipitation and the atmospheric processes that produce precipitation some limitation need to be applied. First the analysis will focus on precipitation processes that are common to portions of North America. From this spatially limited discussion fundamental elements can be extracted and applied to most mid-latitude locations. Second, only liquid precipitation will be considered when discussing WDR. A brief treatment of frozen precipitation will be offered to illustrate precipitation types but there will be no discussion of wind-driven frozen hydrometeors.

This section will first examine the hydrologic cycle—emphasizing those portions of the cycle that are essential for the understanding of WDR. The section will continue with an analysis of precipitation types and the distinguishing thermodynamic factors related to liquid and frozen precipitation. A short discussion of droplet formation will be offered which will inform later discussions of the physics of wind interaction with the droplet spectra. The bulk of this section will focus on four rainfall generating systems common across North America. The spatial and temporal distribution of these systems will inform the spatial and temporal distribution of WDR and suggest predictability of WDR under future climate scenarios. To provide coherence to this section, climatology of liquid precipitation will be presented, focusing on both the geographic nature of rainfall in North America and providing an examination of the seasonality of rainfall and the inter-annual variability of rainfall in the mid-latitudes. Finally, attention will be given to the statistical properties of rainfall across North America including the basis for rainfall intensity-duration-frequency curves and recurrence intervals for rainfall of varying intensity.

2.2 Hydrologic Cycle

Figure 2.1 below is a discrete representation of the hydrologic cycle with defined boundaries for sinks and sources of water (in all phases), distinct flux pathways between sources, and defined physical processes that operate on the water molecule during storage and flux in the system. Many textbooks include such a rendering of the hydrologic cycle and depending upon discipline (hydrology, soil science, oceanography, etc.) most authors explain and expand upon the hydrologic cycle in a phenomenon-centric stance. For example a soil scientist may describe rainfall as a component that facilitates infiltration—and then expand the discussion to movement, storage, and alteration of water in the soil. This author will be no different and will discuss the hydrologic cycle as the large scale system that brings together atmospheric elements that yield conditions favorable for WDR.

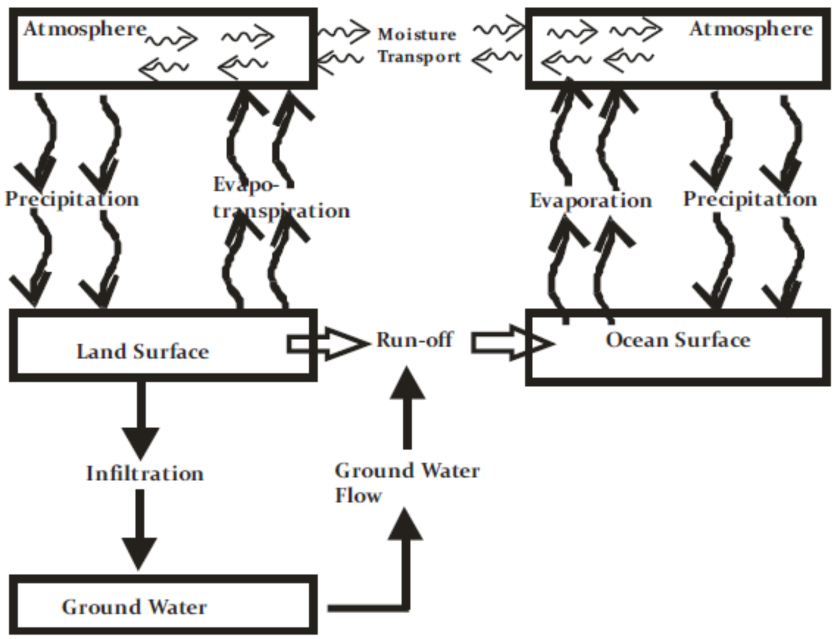

Figure 2.1. Basic illustration of the elements and fluxes in the hydrologic cycle.

Figure 2.2 is the representation of the hydrologic cycle as it influences WDR. In this figure there are numerous polygons of differing shades and colors, each representing a portion of the hydrologic cycle. The overlap of polygons may be seen as interdependent processes that directly influence both precipitation and wind regimes. For example at point “A” on Figure 2.2 there is a confluence of moisture transported from both continental air masses and maritime air masses. This moisture transport can be linked to precipitation processes in the mid-latitude such as frontal regimes and extra-tropical cyclones as well as tropical regimes such as land-falling tropical cyclones—both of which produce WDR. At point “B” in the figure land-surface evapotranspiration (latent heat flux) is highlighted. This flux is tied to soil moisture and influences mid-latitude moisture transport via convection, advection, and eventually cyclogenesis—again leading to rainfall and WDR at continental locations.

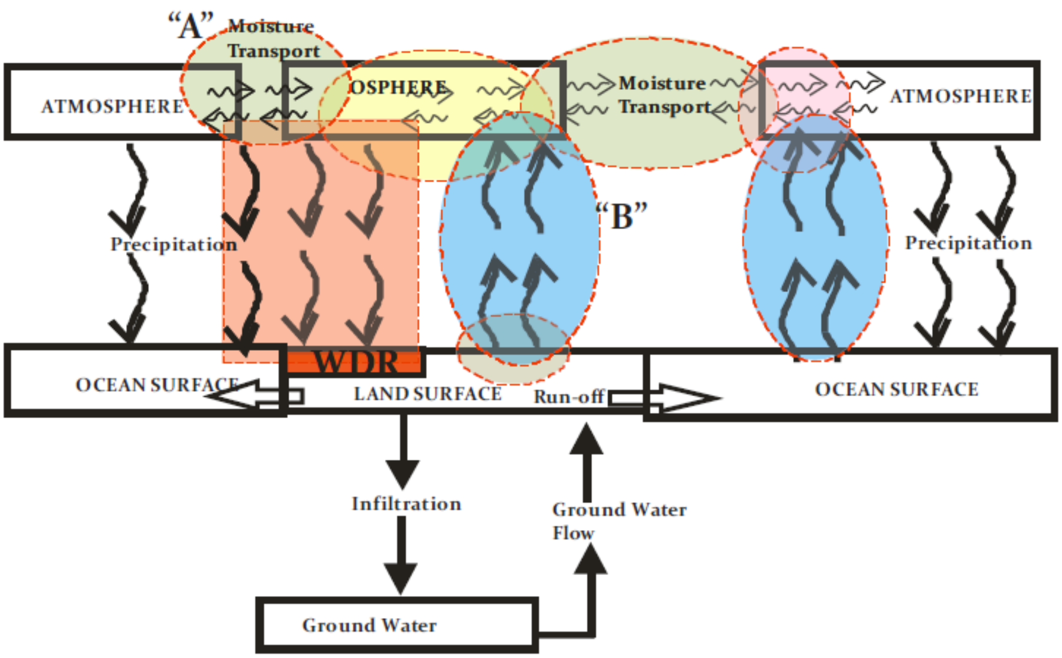

Figure 2.2. Advanced view of the WDR-centric hydrologic cycle.

2.3 Precipitation Type

As was seen above in the illustration of the hydrologic cycle, moisture is moved from surfaces (ocean and continental) via evaporation and transpiration and once in the atmosphere can exist for varying periods of time as water vapor. The water vapor may condense to form liquid water droplets, which in turn may freeze producing suspended ice crystals. Of course water vapor may bypass the liquid phase and directly form ice crystals in the upper troposphere. Liquid water may also change phases and return to vapor with evaporation in the atmosphere. In this section the discussion will focus on hydrometeor formation (water droplets and ice crystals) and the precipitation processes that deliver water to the earth's surface.

Water vapor as a component of the atmosphere ~~that~~ is quite variable with most of the earth-atmosphere water vapor confined to the lower portions of the troposphere. Though varying over space and time one can estimate that water vapor constitutes approximately four percent of the atmosphere's mass. Water vapor can be estimated by metrics which include relative humidity, absolute humidity, and mixing ratio. Dew point depression and precipitable water can also be an indicative of water vapor in the troposphere. When water vapor changes phase to ice (deposition), a freezing nuclei is usually present. The same is true for a phase change from vapor to liquid, in this case the nuclei is referred to as condensation nuclei.

The typical condensation or freezing nuclei diameter ranges from 0.01 to 0.2 mm and can be easily suspended in the atmosphere. The typical distribution of cloud droplets range from 20mm to 100mm in diameter. However to fall from suspension in the atmosphere droplets must grow to approximately 1000mm and very large rain drops can have a diameter of 5000mm. Liquid cloud droplets increase in size via collision and coalescence. During the cloud droplet's life cycle it will be influenced by both gravity and pressure gradients producing vertical and horizontal forces in the atmosphere. As these forces move the individual droplets within a cloud, collisions inevitably occur and with collisions the droplets coalesce—becoming larger. Once large enough to fall from suspension the raindrop will fall and continue to grow as it encounters more droplets. This is often referred to as a warm-cloud process as the entire process takes place with water in liquid phase and cloud temperature above 0°C.

At latitudes where mid and upper tropospheric temperatures are below 0°C a second process is at work to produce raindrops. This process has been referred to as the Bergeron-Findeisen process and is a cold-cloud process. In clouds with mixed phase hydrometeors (liquid and solid) Bergeron-Findeisen theory holds that ice crystals will grow at the expense of super-cooled liquid water within the cloud. This is based on the lower saturation vapor pressures adjacent to the surfaces of ice crystals compared to that of a liquid water droplet. With a lower surface vapor pressure ice crystals become freezing nuclei for super-cooled liquid water droplets in the cloud. As the ice crystals grow they also begin a fall toward the earth via gravity and on this fall they may continue to grow by riming and accretion. Whether a warm-cloud or cold-cloud process the raindrop size will be influenced by: 1) the total amount of liquid water present in the cloud; 2) the vertical thickness of the cloud; 3) the presence of updrafts and downdrafts (pressure gradient forcing) in the cloud: 4) the electrical charge of water droplets; and 5) the residence time of the droplet within the cloud.

As we are concerned mainly with rainfall and its interaction with wind in the near-surface environment it is important to distinguish an atmosphere that will produce rainfall from an atmosphere that will deliver frozen precipitation to the surface. This can be done by comparing the thermodynamic structure of the atmosphere coincident with hydrometeor formation. Figure 2.3, is a skew-t plot representing a number thermodynamic parameters in the troposphere. The skew-t diagram in this case represents an atmosphere in which snow would be the most likely form of precipitation to reach the ground. In this cold-cloud sounding precipitation formation is taking place in a layer between 800hPa and 550hPa. This entire layer is below 0°C; in fact the temperature at 600hPa is -22°C. The tropospheric layer from 800hPa to the surface is also below 0°C with surface temperature at -12C. With this vertical temperature configuration the typical hydrometeor impacting the surface would be an ice crystal (snow flake).

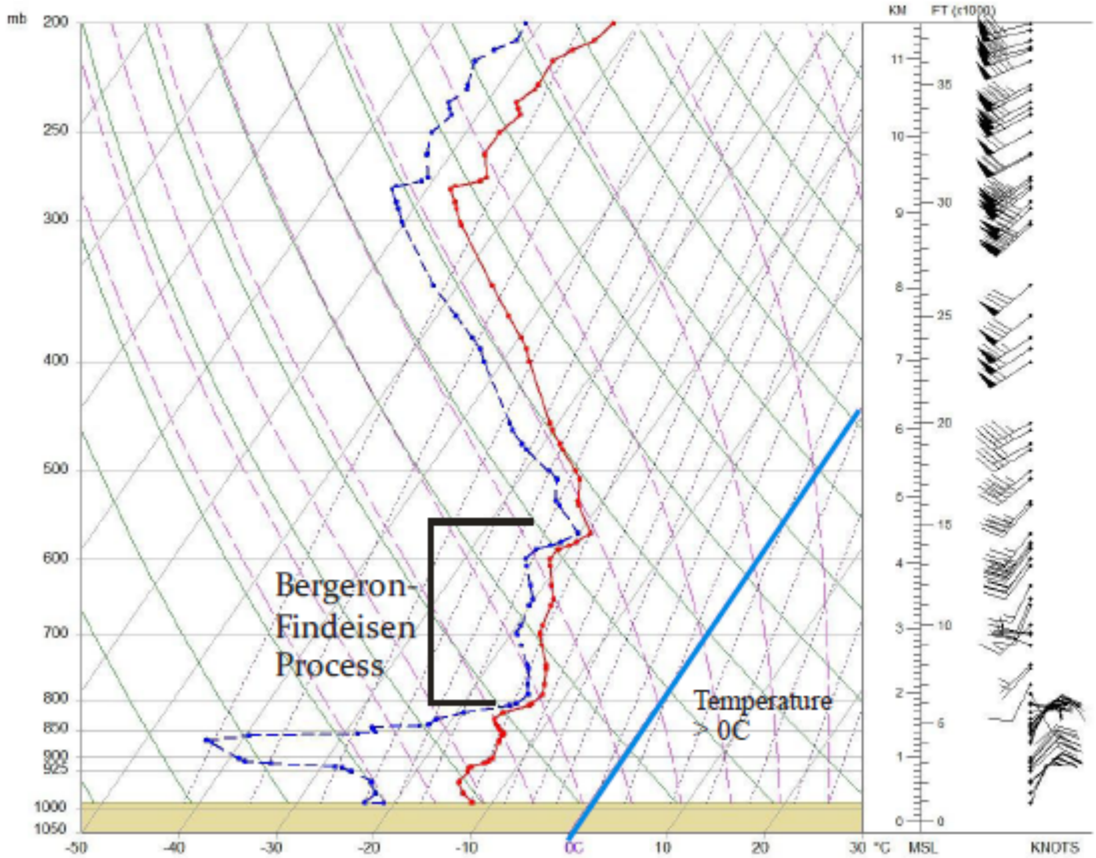

Figure 2.3. Atmospheric profile for snowfall.

In the atmospheric sounding analyzed on the skew-t plot in Figure 2.4, the same ice crystal growth mechanisms are at work in in the mid-troposphere; however, these ice crystals (snowflakes) fall through a portion of the lower troposphere where the air temperature is above 0°C. In this case the layer extends from 900hPa to 800hPa. As the ice crystals fall through this warm layer they melt into liquid hydrometeors. However, before reaching the earth's surface these liquid hydrometeors encounter a cold layer in the lowest portion of the troposphere (surface to 900hPa) and re-freeze into a frozen from of precipitation (sleet). The sleet profile is defined by a warm layer above a frozen surface with active hydrometeor growth via cold-cloud processes aloft in the troposphere.

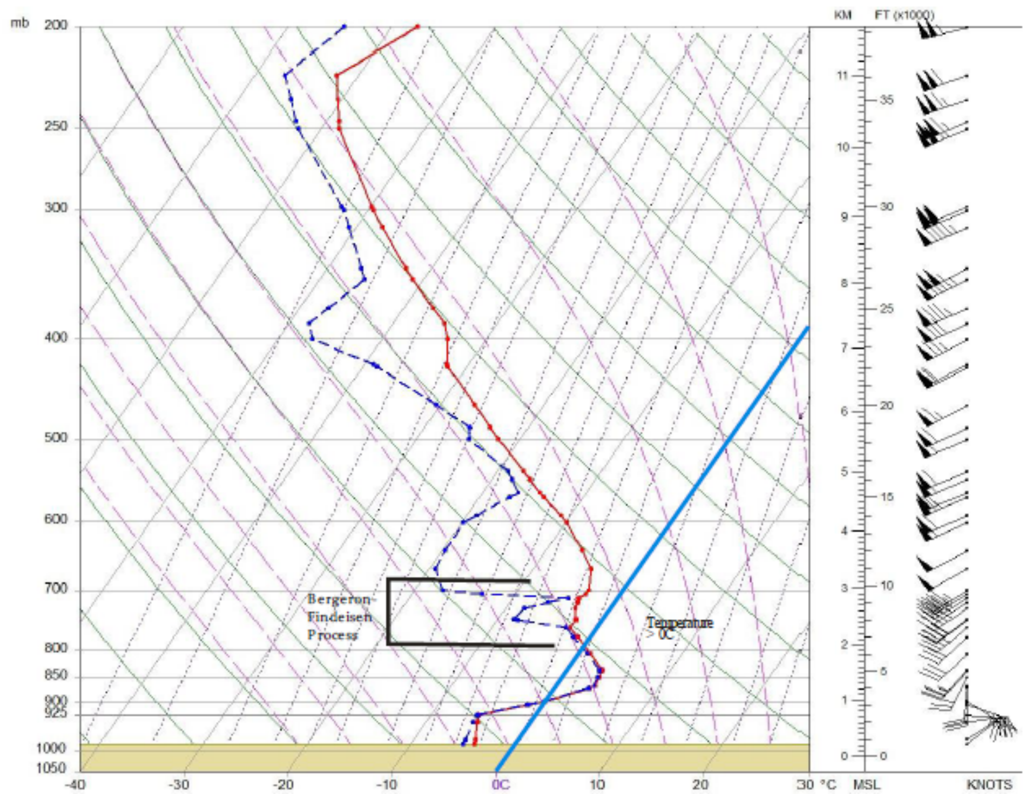

Figure 2.4. Atmospheric profile for sleet.

Finally, for WDR it is important to know the atmospheric structure that will produce liquid precipitation. This configuration is shown in Figure 2.5. In this case the Bergeron-Findeisen process is growing ice crystals in the atmospheric layer from 750hPa to 500hPa. The ice crystals that grow and fall from suspension enter a warm layer near 800hPa and the hydrometeors melt into liquid raindrops. The drops remain in liquid form as the temperature from 800hPa to the surface remains above 0°C. The temperature at the surface in this example is 9°C and rain is falling at the surface in this location. It should also be noted that along with the rainfall near-surface winds are sustained at 45knots which would suggest that WDR would be likely with this particular atmospheric configuration.

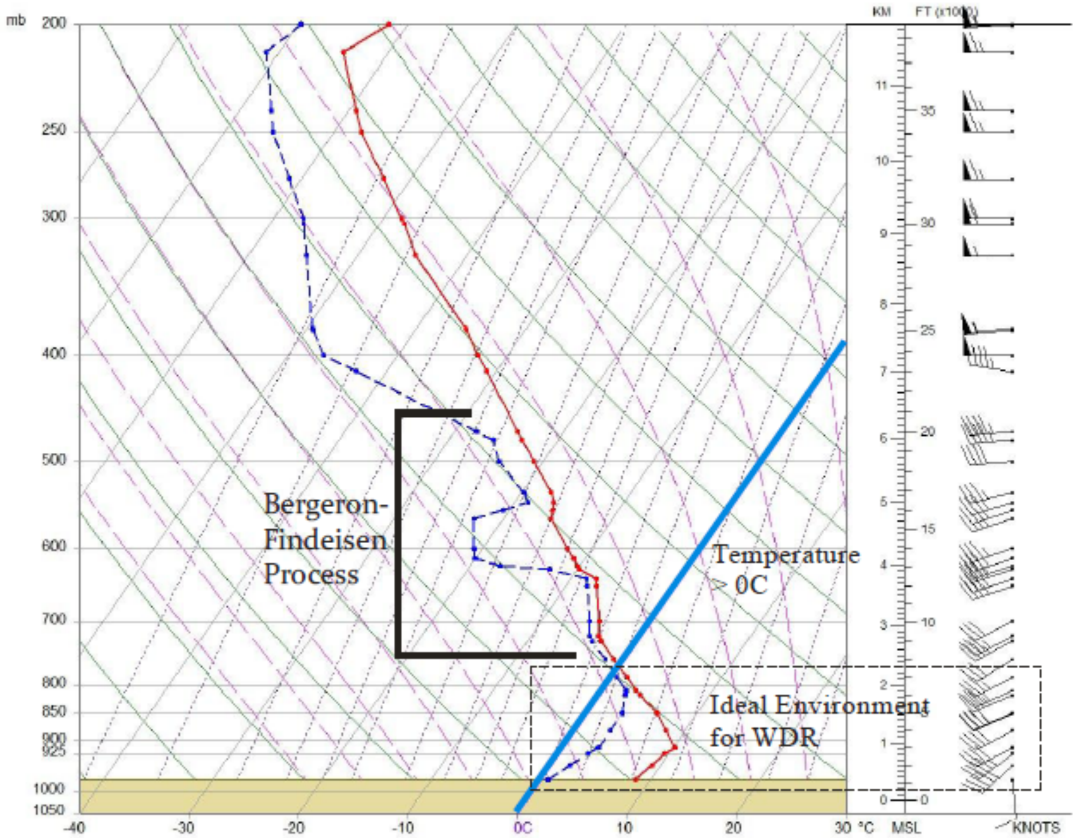

Figure 2.5. Atmospheric profile for rainfall.

2.4. Precipitation Events

2.4.1 Ideal Atmospheric Processes for WDR Generation (Mid-Latitude Cyclone)

Using the mid-latitudes as reference region there are a number of atmospheric processes and phenomena that produce sounding profiles similar to Figure 2.5 (providing both liquid precipitation and vigorous surface winds). The mid-latitude cyclone (MLC) is the most common precipitation producing mechanism and within the MLC WDR may be observed at locations adjacent to the cold and warm fronts as well as in conjunction with the central low pressure area associated with this circulation phenomenon. A model of the MLC is offered in Figure 2.6.

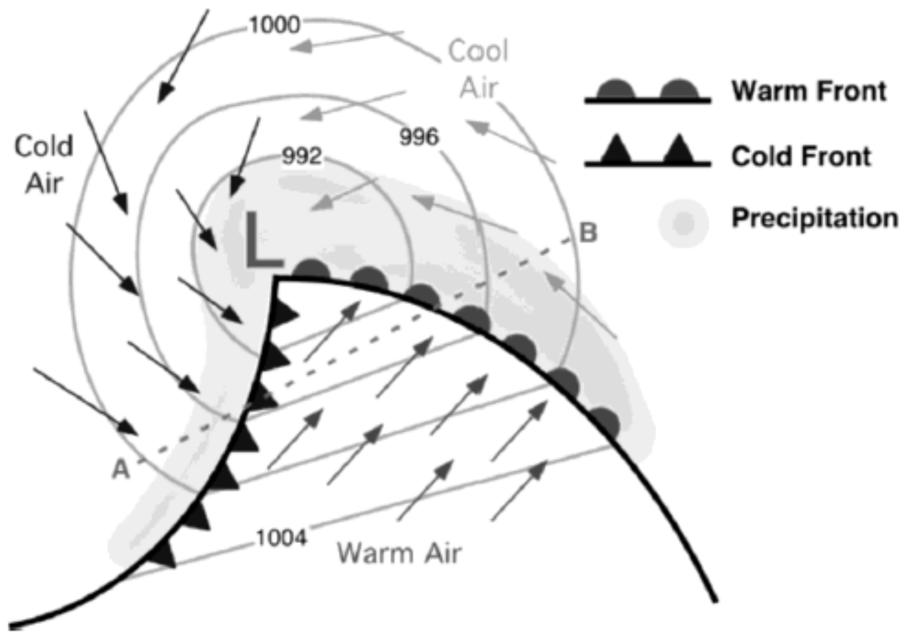

Figure 2.6. Model of Mid-latitude (extra-tropical) Cyclone with attendant fronts and surface low pressure center. Fronts are identified in the legend.

In the model MLC one can ascertain from the surface isobars that atmospheric pressure decreases towards the central low pressure center which is identified by a closed isobar and the letter 'L.' Cold air advects into this model system from the north and west displacing warm (and likely moist) air that originates from the south. Circulation around the central low is counter-clockwise and the model system will translate west-to-east following the 500hPa steering currents. The MLC will also be enhanced and depressed by the dynamics of the mid-tropospheric flow. Vertical motion will be enhanced (impeded) with mid-tropospheric divergence (convergence).

The MLC is an ideal system for producing WDR as rainfall can be generated along both frontal boundaries and in areas adjacent to the central low pressure area. This precipitation falls through a heterogeneous near-surface pressure environment that is set up by the MLC, thus providing for near surface winds at various speeds and directions during rainfall episodes.

Figure 2.7 is the surface analysis for 19 March 2012 when a mature MLC was the dominant weather feature across much of North America. In this case the central low pressure center is deepening and surface flow is converging towards the region of the closed isobar. An extensive cold front extends from the Canadian border into northern Mexico. Along this front 24-hour rainfall totals range from a trace in South Dakota to nearly 7mm in Texas. Rainfall is continuous from Nebraska to Texas. Precipitation totals are also substantial just west of the low pressure center where 24-hour rainfall totals are greater than 9mm. One may also note that the analysis on 19 March 2012 also shows semi-linear troughs (analyzed with dashed lines). These troughs are regions of relatively lower pressure and can generate rainfall when moisture is available. In this case the multiple troughs produce a near continuous rainfall region across the intermountain western US.

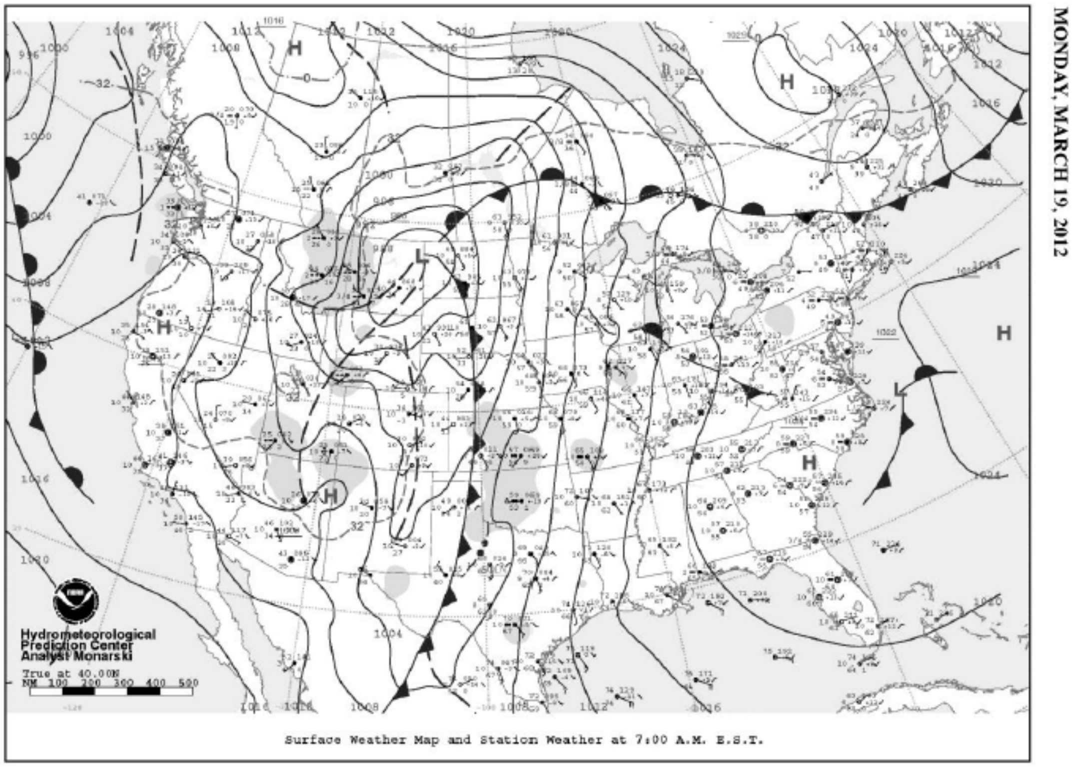

Figure 2.7. MLC as analyzed at the surface on 19 March 2012. Areas of rainfall are identified by gray shading.

In Figure 2.8 the MLC from the analysis of 19 March 2012 has both translated southeastward and occluded. In this stage of development the MLC produces intense rainfall and the rainfall is delivered in a very unique spatial pattern. Along the occlusion 24-hour rainfall totals of 48mm are observed near the closed low and 24-rainfall totals in excess of 18mm extend along the highly curved cold front that is tapping very moist (and warm) air from the Gulf of Mexico.

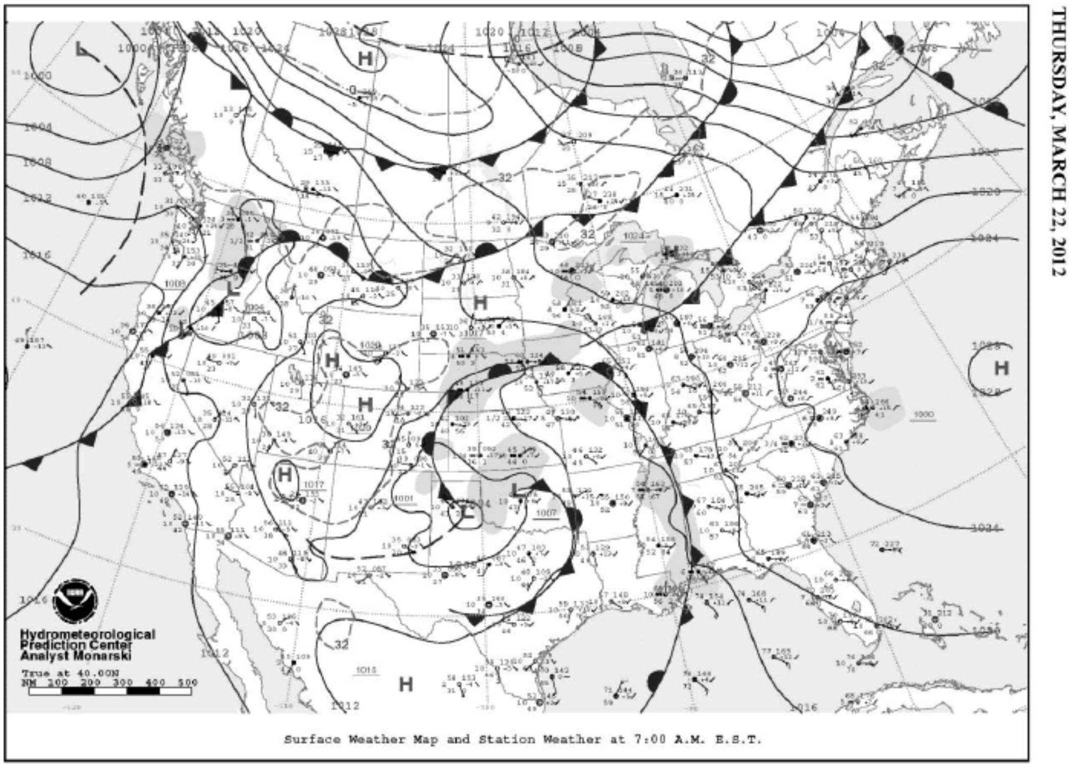

Figure 2.8. Occluded stage of MLC from surface analysis of 22 March 2012. Again rainfall regions are identified by gray shading.

The location and intensity of rainfall along a cold frontal boundary is a function of the larger scale atmospheric setting and the elements in place to produce either a katabatic cold front or an anabatic cold front. In basic definition, a cold front is characterized by relatively strong horizontal temperature gradient, static stability, horizontal wind shear, and vertical wind shear (Moore and Smith 1989). The weather, in particular rainfall patterns allow further refining of the cold front definition. An anafront is identified by a general upgliding motion of warm air along the sloping cold frontal surface which produces widespread post-frontal cloudiness. With an anafront, most rainfall occurs behind the advancing cold front and can be intense and of relatively long duration (Figure 2.9). Katafronts on the other hand are accompanied by postfrontal decent of dry air which restricts the ascent of the warm moist air, thus producing a narrow band of rainfall ahead of the surface cold front (Keyser and Shapiro 1986; Bergeron 1937). Rainfall is usually very light and of shorter duration with the passage of a katafront (Figure 2.9). By distinguishing between anafronts and katatfronts, one can forecast more accurately the location and intensity of both vertical rainfall and WDR associated with an advancing cold front.

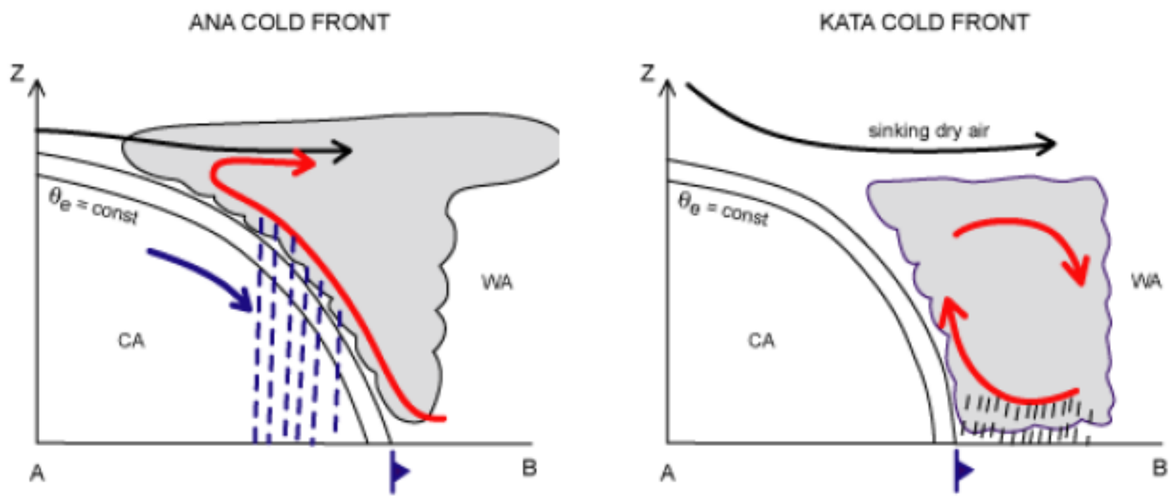

Figure 2.9. Diagram on left is a representation of rainfall associated with an anafront. The diagram on the right is a depiction of rainfall associated with a katafront (Source: http://www.zamg.ac.at/docu/Manual/)

2.4.2 MLC Climatology and WDR

The frequency of MLC development and the tracking behavior of mature MLC's are important elements for the development of a rainfall assessment. As WDR may result from mature MLC's, knowledge of the MLC climatology is fundamental to understanding the WDR climatology. From an analysis of Figure 2.10 one can see that MLC initiation (or cyclogenesis) is marked by inter-annual and intra-annual patterns. For example the first image illustrates the frequency of MLC development during December 1998. When compared to image two (the MLC climatology for July of 1998) it becomes clear the MLC's develop more frequently during the winter month and the regions of cyclogenesis differ substantially from cold season to warm season in North America. Comparing MLC development for two winter seasons (December 1998 and December 1977 (image three) one can also see that there is great variability between winter seasons in terms of MLC development. For example in December 1977 there were very few MLC's developing over the Gulf of Alaska compared to December 1998. Also during December 1977 there was an increased frequency of MLC formation in the central portion of the US compared relatively little cyclogenesis in this region during December 1998. These three illustrations suggest that MLC formation is variable in both space and time and thus WDR should follow a similar climatological pattern.

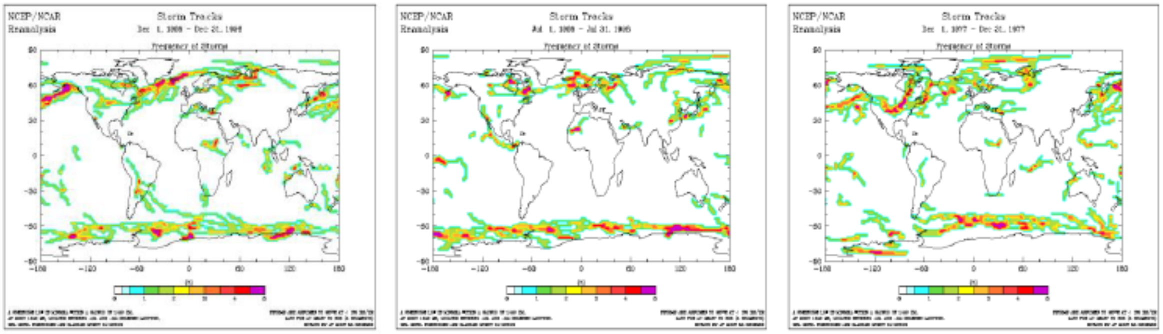

Figure 2.10. MLC formation frequency for December 1998, July 1998, and December 1977 (Source: http://data.giss.nasa.gov/stormtracks/)

2.4.3 Ideal Atmospheric Processes for WDR Generation (Convective Storms)

Another common source for WDR is convective weather or thunderstorms. Thunderstorms can occur as single cells, as clusters, as a line (squall line) or in extremely large agglomerations called mesoscale convective systems (MCS). Single cell thunderstorms may occur when surface temperatures reach the thermodynamically calculated convective temperature (T_c). This allows warm and moist surface air to ascend past the lifted condensation level (LCL) at which time a convective cloud will begin to form. Further instability will allow the air parcel to reach the level of free convection (LFC) where the rate of cooling of the rising parcel is less than that of the free atmosphere. Above the LFC a cumulus cloud may develop rapidly and produce a thunderstorm. A mature single cell thunderstorm will be characterized by a strong updraft of warm air adjacent to a downdraft of cold air and mixed phase hydrometeors. As the downdraft strengthens it will intersect with the surface delivering rainfall and strong localized surface winds—a recipe for WDR. Figure 2.11 is the idealized life cycle of a single cell thunderstorm. One should be mindful that the instability required for a thunderstorm may result from intense surface heating or from the advection of cold dry air aloft. Either of these scenarios is capable of producing a situation in which air parcels ascend rapidly and produce convective clouds.

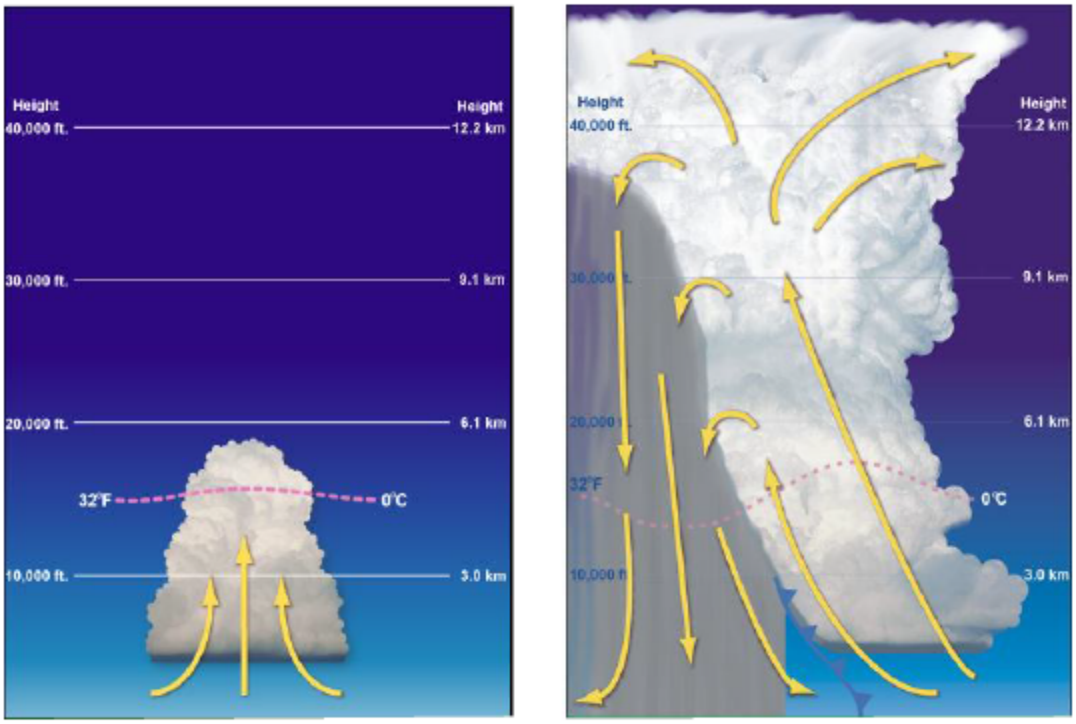

Figure 2.11. The left panel shows the developing stage of a single cell thunderstorm while the right panel illustrates the mature stage of a thunderstorm with intense rainfall and a gust front depicted as a bending front boundary to the right of the wind/rain shaft that is intersecting the ground surface (Source: http://www.srh.noaa.gov/jetstream/tstorms/life.htm).

Figure 2.12 provides an example of the thermodynamic conditions (via skew-t analysis from balloon sounding data) conducive to a thunderstorm. From the skew-t analysis one can detect a very warm, nearly saturated lower troposphere (surface to 850hPa) and a very cool and dry middle troposphere from 850hPa to 500hPa. Vertical wind shear is also discernible in the illustration.

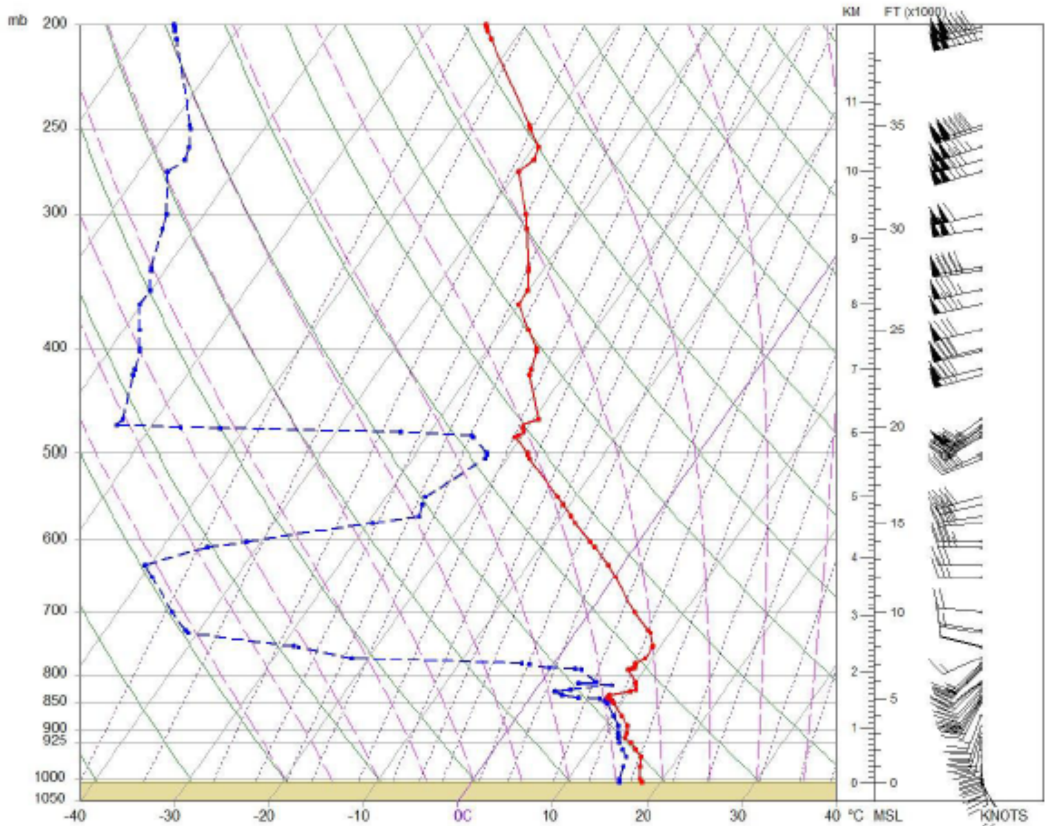

Figure 2.12. Skew-t analysis of radiosonde sounding prior to thunderstorm development at Corpus Christi, Texas on 20 March 2010.

Thunderstorms are efficient producers of WDR and may occur as a single cell as illustrated above or as a line of organized cells called a squall line. The climatological setting for a squall line includes both a rapidly advancing cold front with an intruding dry line between the cold frontal boundary and a warm moist air mass. A squall line can produce both intense rainfall and extremely vigorous straight-line winds. WDR from a squall line may last for prolonged periods and spread over an extensive area. Figure 2.13 shows the radar reflectivity image for a squall line that formed over the central US on 6 June 2008.

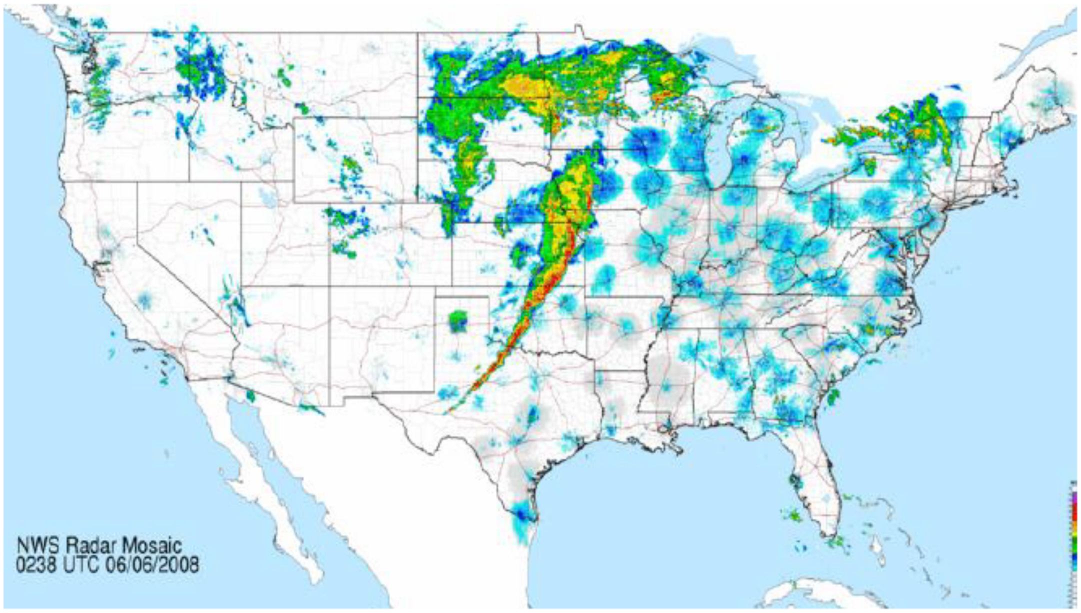

Figure 2.13. Squall line as analyzed by a mosaic of NEXRAD images. In this case a continuous line of thunderstorms extends from central Iowa to northwest Texas.

Another large scale weather system that produces copious WRD is the MCS. An MCS is a convective cloud and precipitation complex that occurs in connection with an ensemble of thunderstorms and produces a contiguous precipitation (and WDR) area on the order of 100km or more. An MCS will exhibit deep moist convection with embedded meso-cyclones that are driven partially by convective overturning (AMS Glossary 2012). A mature MCS is horizontally very large (from 20 to 500km) and can persist for three to twelve hours. In satellite imagery, an MCS will appear as a large circular or oblong cluster of very cold cloud tops. Figure 2.14 shows the satellite view of an MCS that developed over the central US on 11 May 2002 and produced both heavy rainfall and damaging winds as it slowly progressed eastward.

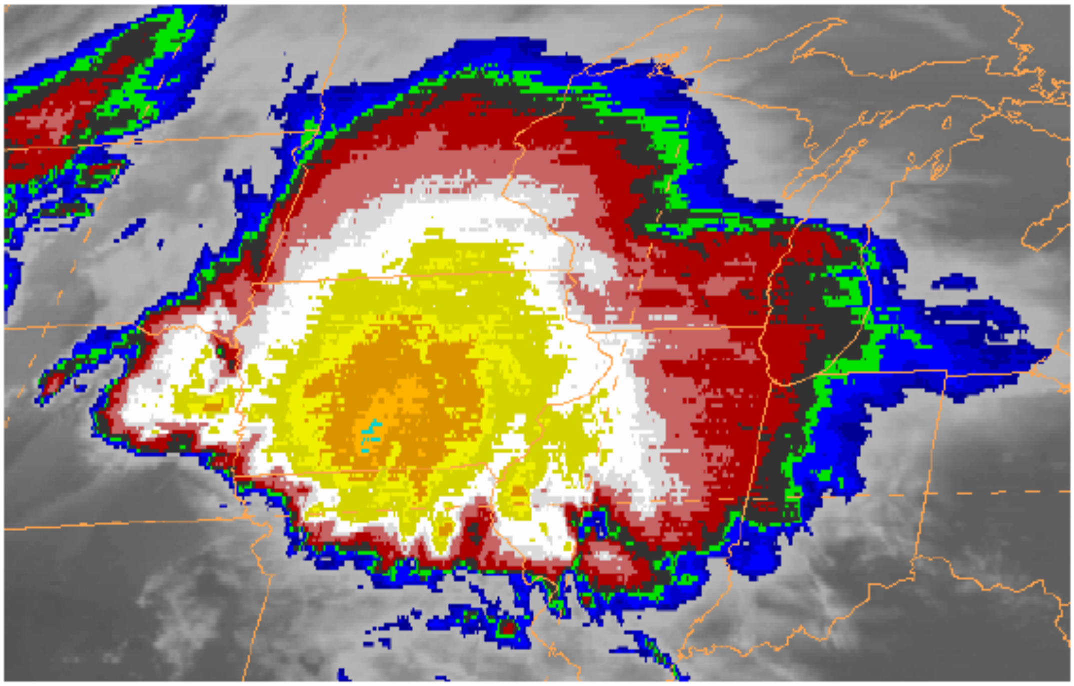

Figure 2.14. Color enhanced IR satellite image of an MCS. Note the amalgamation of convective cloud is centered over Iowa and extends westward into Nebraska and eastward into Indiana.

To illustrate the frequency and spatial extent of thunderstorm activity across North America one can use cloud-to-ground lightning flashes as a proxy for thunderstorm occurrence. Lightning accompanies single cell thunderstorms, squall lines and MCS's so it is a very good indicator of areas where convective weather and therefore WDR is more pronounced. Figure 2.14 is an image taken from Orville et al. (2011) that shows the spatial pattern of annual cloud-to-ground lightning flash density for the period 2001-2009 across North America.

2.4.5 Other Rainfall Producing Scenarios

Rainfall is not limited to convective processes in the mid-latitudes. In fact, rainfall may occur with mid-level stratiform clouds and rainfall can even form in low stratus clouds and fog. One of the primary mechanisms for atmospheric lift, absent convection, is orography. Air masses lifted by topography can be brought to their lifted condensation level producing clouds and in many instances precipitation in the form of rainfall. Orographic precipitation is of course limited to regions of complex terrain but this is an important mechanism for the production of rainfall across the North American landscape.

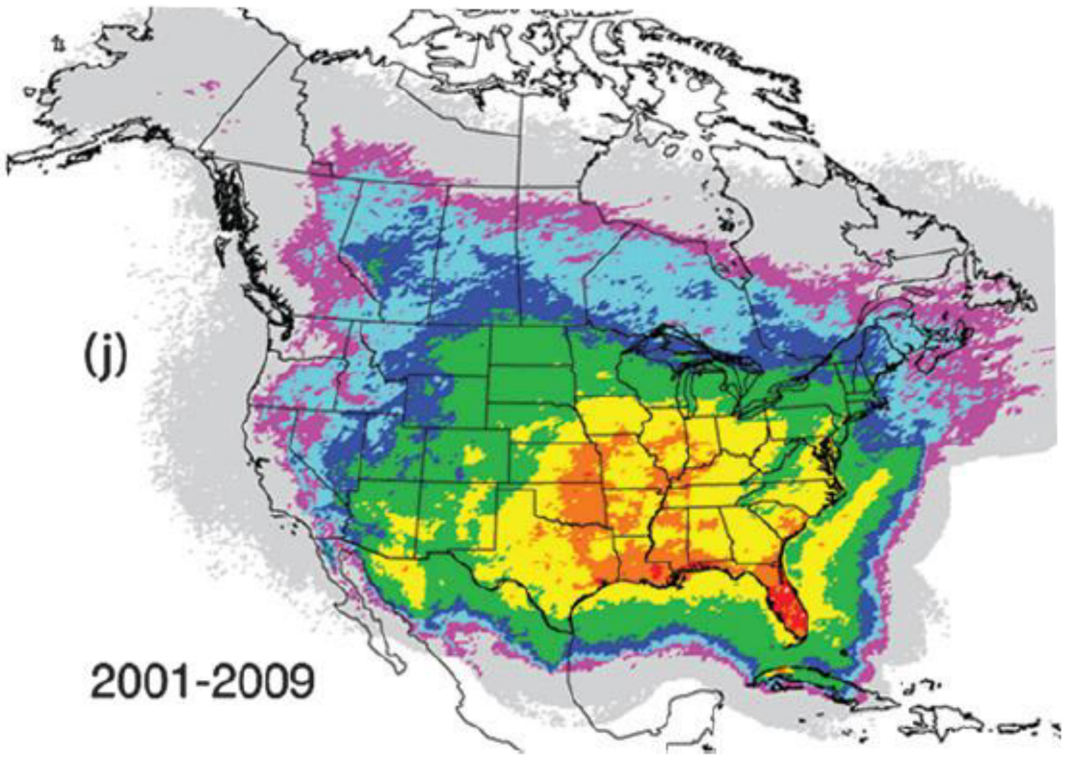

Figure 2.15. Annual cloud-to-ground lightning flash density for the period 2001-2009 derived from the North American Lightning Detection Network. Areas shaded gray have a mean flash density below 0.1 flashes/km^2/year; areas in green have a mean flash density between 1 and 3 flashes/km^2/year; yellow shade areas see between 3 and 6 flashes/km^2/year; and areas shaded in red have a mean annual flash density greater than 9 flashes/km^2/year. Note the areas with the highest flash density: Southeastern US, Central US, Monsoon region of the southwestern US.

2.4.6 Ideal Atmospheric Processes for WDR Generation (Tropical Cyclones)

Tropical weather and tropical rainfall systems in particular are very different from those in the mid-latitudes. Instead of the interactions of frontal boundaries, tropical weather systems are influenced chiefly by a large positive solar radiation flux and Bowen ratios of less than one. This establishes a climate that is very warm with high levels of atmospheric moisture entrained in the air near the earth's surface. Redistribution of this excess energy and moisture takes place via three primary mechanisms: 1) Ocean currents move warm water to higher latitudes; 2) Large scale atmospheric circulation patterns move warm moist air from tropics to mid-latitudes; and 3) Intense meso-scale cyclonic storm systems (tropical cyclones) move energy and moisture from the surface to the upper atmosphere and from lower latitudes to higher latitudes. It is the latter of these processes that has the most discernible impact on the WDR climatology across portions of North America. Tropical cyclones include tropical depressions, tropical storms, and hurricanes.

As a matter of introduction it can be said that all tropical cyclones have the potential for producing WDR, this includes tropical depressions and tropical storms. However, the hurricane is much more likely to produce excessive wind and rainfall and therefore the hurricane will be the focus of this section. The hierarchical framework for assessing hurricane intensity is provided by the Saffir-Simpson Hurricane Wind Scale. Table 2.1 1ists the Saffir-Simpson categories and associated wind speed thresholds for each category. Major hurricanes are those that reach a minimum intensity of category three.

Table 2.1. The Saffir-Simpson Hurricane Wind Scale. Note that a major hurricane must have sustained wind speeds of at least 111mph.

Category	**Wind Speed (mph)**	**Damage**
1	74 - 95	Very dangerous winds will produce some damage
2	96 - 110	Extremely dangerous winds will cause extensive damage
3	111 - 129	Devastating damage will occur
4	130 - 156	Catastrophic damage will occur
5	> 156	Catastrophic damage will occur

Tropical cyclones that develop into hurricanes exhibit both a regional preference for development and a preferred tracking behavior that can be referred to as the tracking climatology. Hurricane development or genesis regions are controlled to a great extent by latitude and sea surface temperature (SST). Tropical cyclones need very warm SST's and a favorable vorticity environment (near equator) to form and to prosper. These regions are found from approximately 3.0°N(S) to 15°N(S). In general, tropical cyclones require large areas of SST greater than 26.5°C (80°F). The image below (Figure 2.16) highlights the ocean regions adjacent to the North American continent where very high SST's can be found.

Figure 2.16. Regions of seasonally high SST's and thus the regions for preferred tropical cyclone development adjacent to the North American continent (Source: http://www.nhc.noaa.gov/climo/).

The climatology of hurricane formation follows the seasonally increased SST's in the regions illustrated in Figure 2.16. It should be noted that many tropical cyclones develop in the eastern Pacific but the tracking behavior of most of these storm steers them into the open ocean away from inhabited land areas. This is not the case with tropical cyclones developing in the Atlantic Basin, the Caribbean, and the Gulf of Mexico. Tropical cyclones in the Atlantic Forecast Region routinely make landfall and produce extreme WDR. A 100-year seasonal climatology of hurricanes and tropical storms for the Atlantic, Caribbean, and Gulf of Mexico is offered in Figure 2.17. This analysis suggests that the peak of hurricane season in the Atlantic Forecast Area is early September. The hurricane season however extends from May through November.

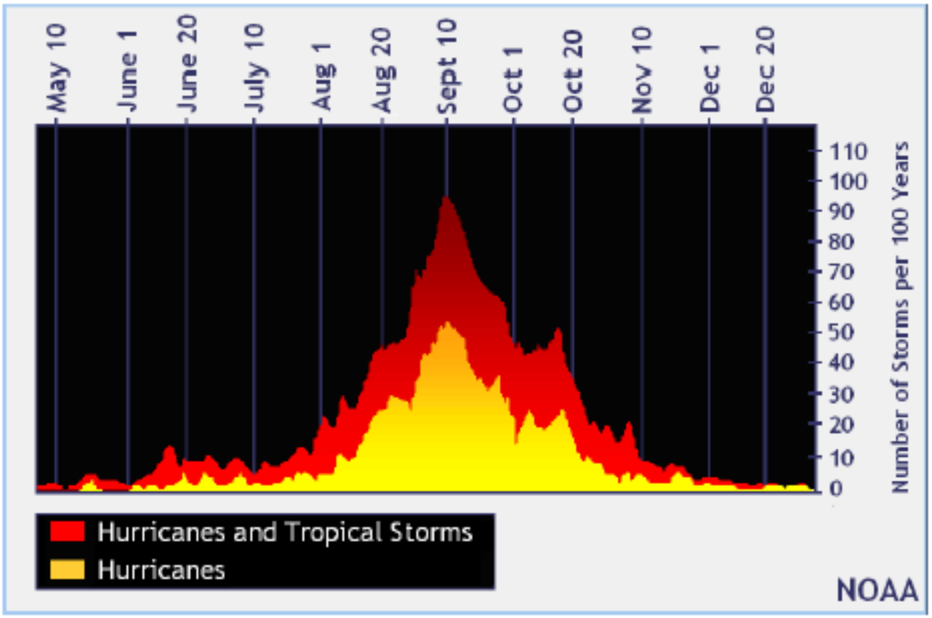

Figure 2.17. 100-year climatology for hurricanes and tropical storms forming in the Atlantic Forecast Area (Source: http://www.nhc.noaa.gov/climo/).

The preferred genesis regions for hurricanes during the August-to-October 'peak season' are shown in Figure 2.18. One can note that this area enlarges as SST's of 80°F expand spatially in September and contract slightly as this area of high SST's shrinks in October. Hurricanes developing in these areas have a high probability of impacting the weather in regions of North America from Mexico to Canada whether by direct landfall or by promoting disturbed weather inland while remaining over the ocean surface.

A historical climatology of hurricane tracks provides a very good indication of the regions of North America where extreme tropical weather is to be expected and where WDR rainfall will be maximized during the hurricane season (Figure 2.19). From this climatological perspective it is clear that hurricanes which develop in the Atlantic Basin, the Caribbean, and the Gulf of Mexico have a high potential for impact along the Gulf Coast, the south Atlantic coast as well as regions as far north as Nova Scotia. It should also be noted that many of these hurricane tracks penetrate deep into the continent and in doing so impact the hydrometeorology in areas quite distant from the coast.

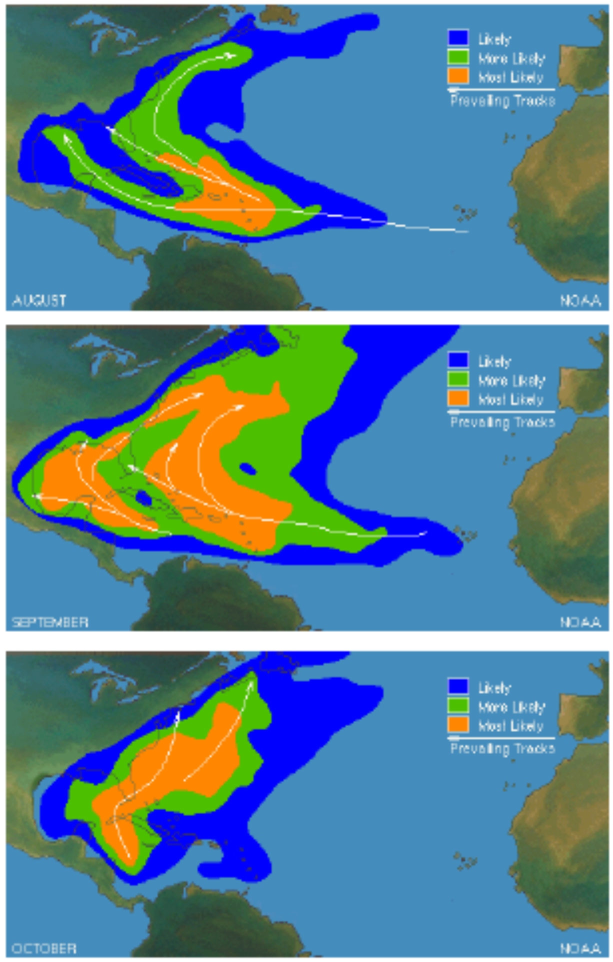

Figure 2.18. Areas of hurricane origin for the months of August, September, and October (Source: http://www.nhc.noaa.gov/climo/).

2.5 Hurricane Structure and WDR

A hurricane, whether making landfall or remaining over open water, has the potential to produce intense rainfall and generate high surface winds—a wonderful recipe for WDR. The intensity of WDR impacting building structures on land is dependent both on the overall intensity of the hurricane (Saffir-Simpson category) as well as the structure and trajectory of the hurricane as it approaches land. Figure 2.20 uses an image of hurricane Katrina to illustrate the variability in rainfall and wind speed intensity in differing quadrants of a hurricane. In most hurricanes developing in the Atlantic Forecast Area, the northeast (NE) quadrant of the cyclone contains the most vigorous inflows of latent heat and is therefore more likely to generate higher near-surface wind speeds and generate more intense rainfall. Points in the path of the NE quadrant therefore are at risk of more damage from WDR than points impacted by the SW quadrant, for example.

Figure 2.19. 100-year climatology of hurricane tracks.

Figure 2.20 also illustrates the variable cloud structure of a hurricane. In particular the figure shows cumulonimbus clouds extending above the broader cloud shield that makes up the hurricane signature in the satellite image. These vertically developed cloud-tops suggest embedded convection in areas adjacent to the hurricane eye and in these convective regions copious rainfall and much higher wind speeds (from downdrafts) can be expected. It is not clear from the current literature whether WDR is intensified by these embedded thunderstorms.

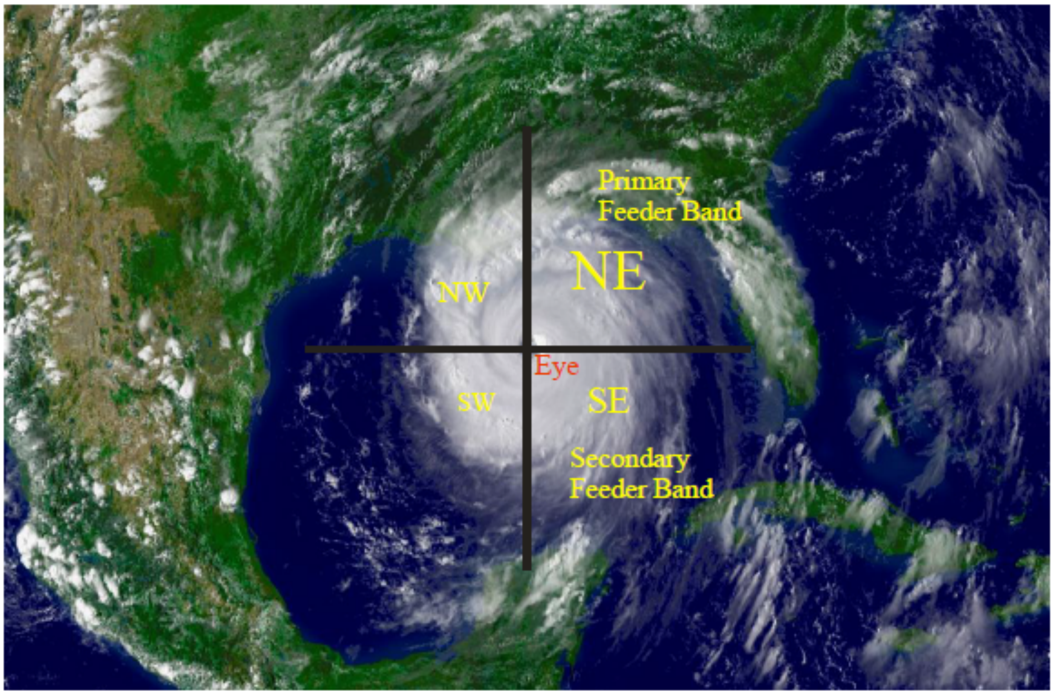

Figure 2.20. Visible satellite image of Hurricane Katrina. Identified on the image are the primary and secondary feeder bands which fuel the storm with latent heat, the eye of the storm which is the center of cyclonic circulation, and the four quadrants of the storm identified by directions and by relative intensity (size of text suggests intensity of winds and rainfall in the quadrant).

2.6 Statistical Analysis of Rainfall

Basic statistical treatments of rainfall include event specific parameters such as storm-total precipitation and maximum one hour rainfall rate. As the temporal domain expands climatological statistical measures provide a quantitative context for understanding rainfall, and thus WDR, patterns. Daily mean rainfall and daily maximum rainfall are common climatological elements that are useful to both forecasters and planners. Monthly statistics include total rainfall for the calendar month and the average rainfall for a particular month over a 30-year period. Annual rainfall data consist of total annual rainfall at point locations, number of rainfall days, and average intensity and duration of rainfall events at a point location. Climatologies of rainfall over a region are also available via interpolation methods. Most of the climatological data described above are easily accessible from the six regional climate centers in the US: Western Regional Climate Center (http://www.wrcc.dri.edu/), High Plains Regional Climate Center (http://www.hprcc.unl.edu/), Midwestern Regional Climate Center (http://mrcc.isws.illinois.edu/), Southern Regional Climate Center (http://www.srcc.lsu.edu/), Southeast Regional Climate Center (http://www.sercc.com/), and the Northeast Regional Climate Center (http://www.nrcc.cornell.edu/).

Fundamental to rainfall analysis is the intensity-duration curve which can be calculated for any observation point where hourly or sub-hourly data are collected over an extended period of time. The curve, an example of which is shown in Figure 2.21 provides information for derivation of the design rainfall event such as the 5-year, 24-hour storm at a particular location. A detailed description of the method can be found in Dunne and Leopold (1995).

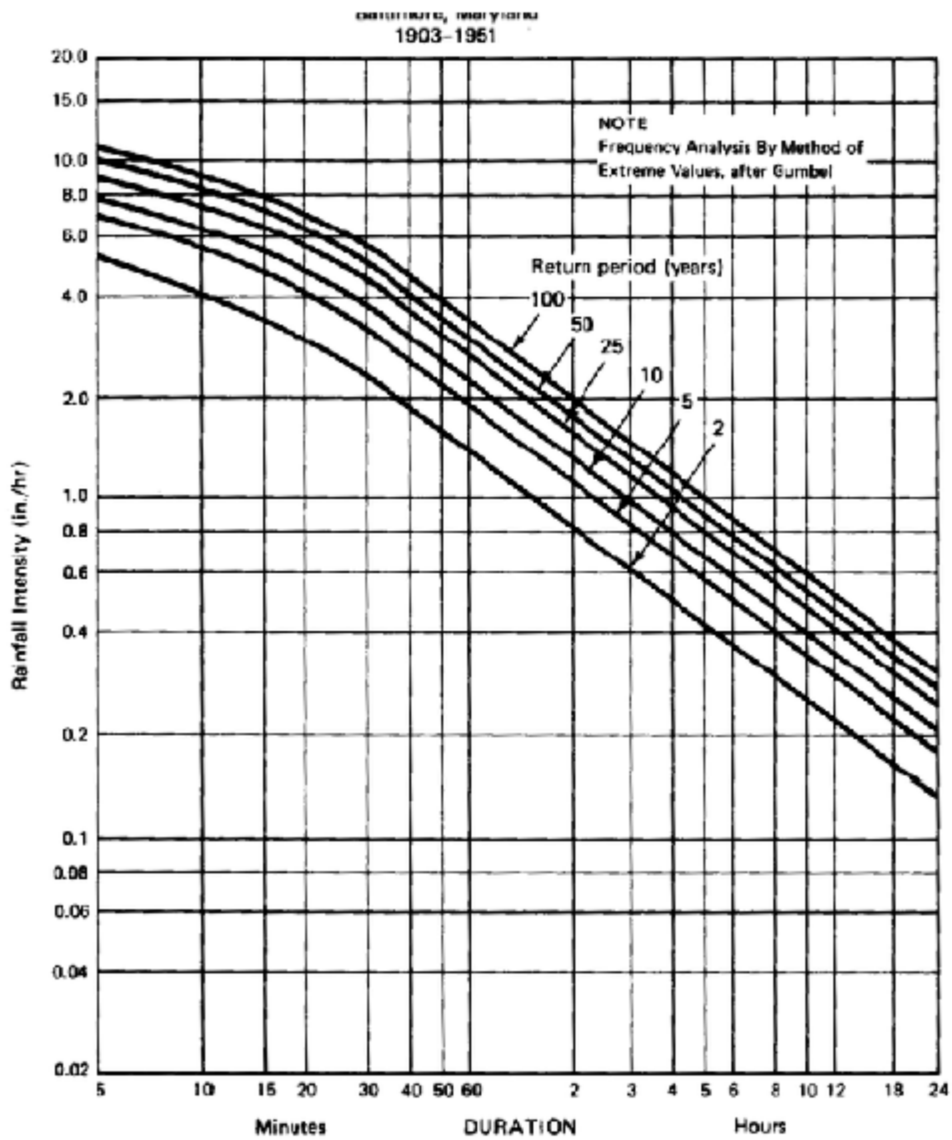

FIGURE 4–4 Rainfall intensity-duration-frequency. (National Weather Service, 1961.)

Figure 2.21. Long-term Intensity-Duration Curve for point location. The x-axis represents duration of rainfall events, the y-axis represents the intensity of rainfall events. The multiple curves represent the return intervals for design rainfall events.

As geospatial technology has advanced new approaches to developing rainfall climatologies have evolved. One of the most evolved products is the PRISM data set which is produced by the PRISM Climate Group at Oregon State University. PRISM data sets are state-of-the-art in terms of the interpolation methods used to estimate of rainfall parameters over space (including complex terrain). The PRISM data set and may be obtained at: http://www.prism.oregonstate.edu/. An example of monthly rainfall data in PRISM format is illustrated in Figure 22.

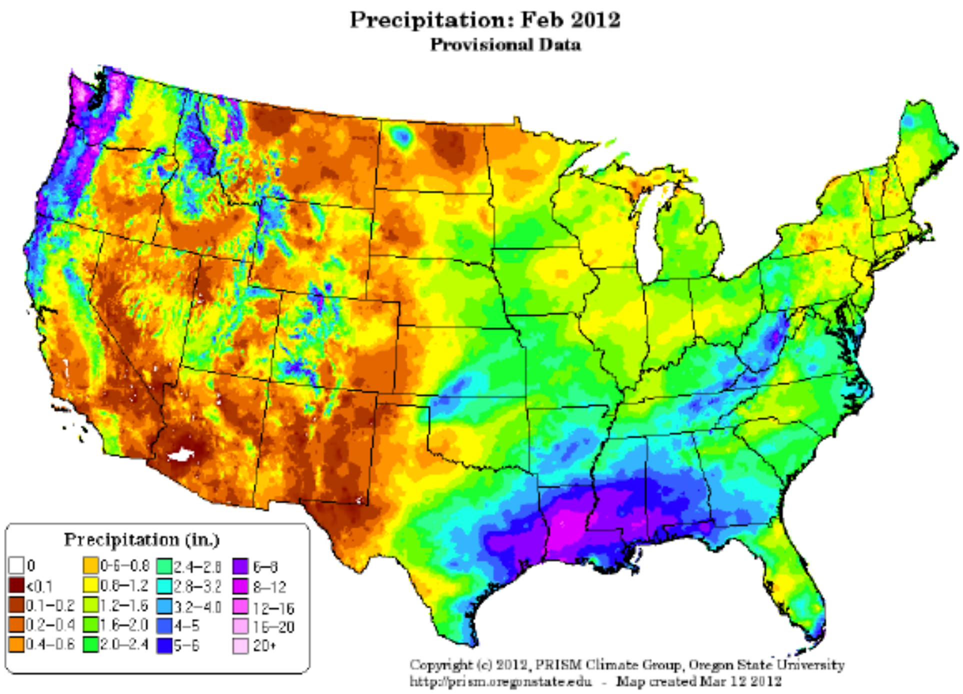

Figure 22. Rainfall data (February 2012) for the US using the PRISM interpolation algorithm.

To conclude it is important to note that spatial patterns of WDR will closely follow the rainfall climatology. However the intensity of WDR will depend on multi-scale processes and weather systems varying frequencies and return intervals, included among these are: thunderstorms, mid-latitude cyclones, and hurricanes.

3. Building / Wind-Driven Rain Interaction

Authors: Bert Blocken, Audra Kiesling

3.1. Wind flow pattern around building

Wind-driven rain (WDR), also referred to as "driving rain", is one of the most important moisture sources for building facades. It is an essential boundary condition for the analysis of the hygrothermal behavior and durability of historical and contemporary building facade components (Sanders 1996, Dalgliesh and Surry 2003, Blocken and Carmeliet 2004, Tang and Davidson 2004, Blocken et al. 2007, Janssen et al. 2007, Briggen et al. 2009, Masters et al. 2008, Salzano et al. 2010, Lopez et al. 2011). This chapter provides information on the interaction between wind-driven rain (WDR) and buildings. First, in section 3.2, the main definitions, parameters and the raindrop equation of motion are presented. Sections 3.3 through 3.6 provide a brief overview of raindrop size distribution, terminal velocity, mass flux spectra and hyperfine clustering, respectively. The last sections in the chapter identify the impacts and effects that wind-driven rain has on building façades.

3.2. Raindrop trajectories

3.2.1. Rain intensity vector, horizontal rainfall intensity and wind-driven rain

The "rain-intensity vector" is defined as the vector, the magnitude of which is the rainfall intensity (in mm/h or L/m²h) and the direction is that from which the rain is coming. We additionally define the specific rain intensity vector $\overrightarrow{R_d}$ that is related to one specific raindrop diameter d. Its magnitude is that part of the rainfall intensity composed of drops with diameter d, its direction is that of the velocity of raindrops with diameter d. The combination of wind and rain causes obliquity of the rain-intensity vector. This oblique rain is referred to as either "wind-driven rain" or "driving rain". The former term will be used in this book because the term driving rain sometimes yields confusion as it is not used in other research domains. The acronym WDR will be used. In general, "WDR intensity" refers to the oblique rain vector. From the viewpoint of the interaction between rain and vertical building facades, the term "WDR intensity" however takes on the narrower meaning of "component of the rain vector causing rain flux through a vertical plane". The latter definition was adopted by the CIB (International Council for Building Research) (Birkeland 1965) and is used in this book. The other component of the rain-intensity vector, that causes rain flux through a horizontal plane, is termed (horizontal) rainfall intensity.

The definition of the rain-intensity vector, of WDR and of horizontal rainfall intensity is clarified by Fig. 3.1. In Fig. 3.1a, a homogeneous wind-flow field is considered. This means that there is no disturbance of the flow field and that at every position, the vertical profile of mean horizontal wind speed is the same. Let us assume that the rain behaves as if all drops were of the median size d_{50}. As a result of the homogeneous wind field, the raindrop trajectories are parallel (assuming a steady-state wind field). Two raindrop trajectories form a stream tube, the entrance and the exit of which are shown in the details 1 and 2. At a certain height above ground, the rain-intensity vector is $\overrightarrow{R_1}$. At the ground, it is $\overrightarrow{R_2}$. Mass conservation is expressed as:

$$\overrightarrow{R_1} \cdot \overrightarrow{A_h} = \overrightarrow{R_2} \cdot \overrightarrow{A_g} \qquad (3.1)$$

where "**.**" denotes the scalar product of the rain-intensity vector and the surface vector, A_h is the area of a horizontal surface at a certain height above ground and A_g is the area of the rain-gauge orifice. As the areas A_h and A_g are equal (parallel trajectories), following Eq. 3.1, the vertical components of both rain-intensity vectors are also equal and the flux R_h. A_h is measured by the rain gauge. R_h is called the *horizontal* rainfall intensity (because it is measured by a gauge with a horizontal orifice; the definitions of measured rain intensity in hydrology are generally related to the gauge, not to the direction of the rain-intensity-vector component that is measured).
In Fig. 3.1b, a building disturbs the wind flow. The wind field is no longer homogeneous and the raindrop trajectories are no longer parallel to each other. Mass conservation in the stream tube yields:

$$\overrightarrow{R_1} \cdot \overrightarrow{A_h} = \overrightarrow{R_3} \cdot \overrightarrow{A_f} \qquad (3.2)$$

where A_f is an area on the building facade. According to the definition given above, the WDR intensity R_{wdr} is the horizontal component of the vector $\overrightarrow{R_3}$ (which causes flux through the vertical plane). It is calculated from Eq. (3.3):

$$R_h\, A_h = R_{wdr}\, A_f \qquad (3.3)$$

3.2.2. Specific catch ratio and catch ratio

As shown above, the rain intensity is indicated by the symbol R (rate of rainfall in L/(m²h) or mm/h). The rain amount is indicated by the symbol S (sum of rainfall in L/m² or mm). Several definitions have been used to describe the WDR intensity and the WDR sum on building facades. In this book, we will adopt the definitions by Blocken and Carmeliet (2002) and we define and use the specific catch ratio η_d, related to the raindrop diameter d, and the catch ratio η, related to the entire spectrum of raindrop diameters. They are defined as:

$$\eta_d(d,t) = \frac{R_{wdr}(d,t)}{R_h(d,t)} \quad ; \quad \eta(t) = \frac{R_{wdr}(t)}{R_h(t)} \qquad (3.4)$$

$R_{wdr}(d,t)$ and $R_h(d,t)$ are the specific WDR intensity and the specific horizontal rainfall intensity for raindrops with diameter d. $R_{wdr}(t)$ and $R_h(t)$ respectively refer to the same quantities but integrated over all raindrop diameters. It is important to note that $R_h(t)$ and $R_h(d,t)$ are "unobstructed" horizontal rainfall intensities. The term unobstructed refers to rainfall through a horizontal plane that is situated outside the wind-flow pattern that is disturbed by the building (i.e. the rainfall that would be measured by a rain gauge placed in open field, as shown in Fig. 3.1a). In practical applications the (specific) catch ratio will be measured and calculated for discrete time steps $[t_j, t_j+\Delta t]$. The (specific) catch ratio for a discrete time step is redefined as:

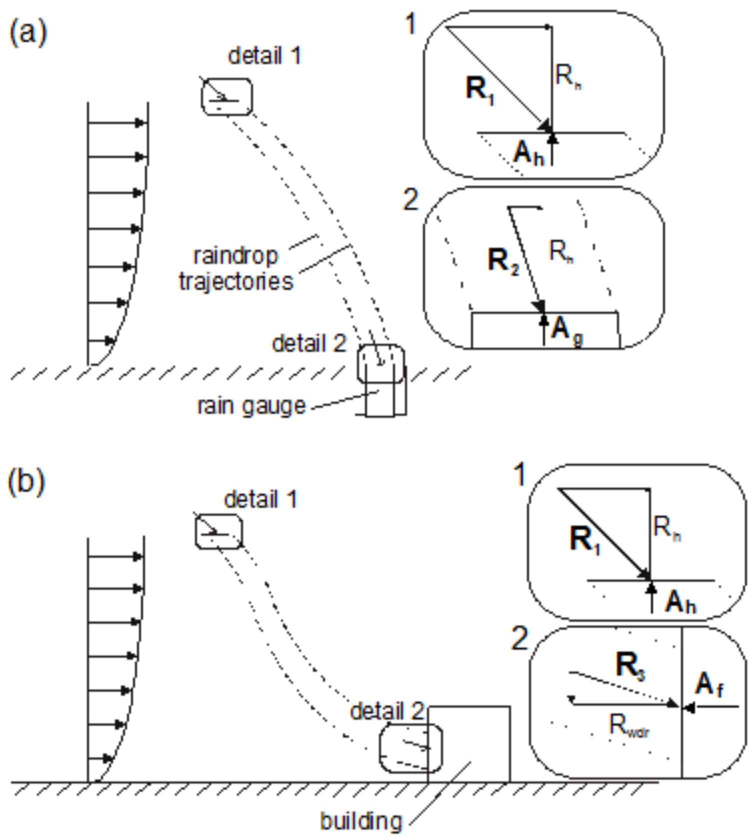

Figure 3.1. (a) Definition of horizontal rainfall intensity. In the figure, the rain falls to the ground in homogeneous wind conditions (raindrop trajectories are parallel to each other). Two raindrop trajectories form a stream tube. Expressing mass conservation indicates that the vertical component of the vectors $\overline{R_1}$ and $\overline{R_2}$ are the same (i.e. the horizontal rainfall intensity). (b) Definition of wind-driven rain on a building. The presence of the building disturbs the flow that is therefore no longer homogeneous (raindrop trajectories are not parallel). Mass conservation in the stream tube allows calculating the wind-driven-rain intensity R_{wdr} from the horizontal rainfall intensity R_h and the areas A_h and A_f.

$$\eta_d(d,t_j) = \frac{\int_{t_j}^{t_j+\Delta t} R_{wdr}(d,t)\,dt}{\int_{t_j}^{t_j+\Delta t} R_h(d,t)\,dt} = \frac{S_{wdr}(d,t_j)}{S_h(d,t_j)} \quad \eta(t_j) = \frac{\int_{t_j}^{t_j+\Delta t} R_{wdr}(t)\,dt}{\int_{t_j}^{t_j+\Delta t} R_h(t)\,dt} = \frac{S_{wdr}(t_j)}{S_h(t_j)} \qquad (3.5)$$

where $S_{wdr}(d,t_j)$ and $S_h(d,t_j)$ are the specific WDR sum and the specific unobstructed horizontal rainfall sum during time step $[t_j, t_j+\Delta t]$ for raindrops with diameter d. $S_{wdr}(t_j)$ and $S_h(t_j)$ respectively refer to the same quantities integrated over all raindrop diameters. It is noted that the catch ratio is a variable that has up to now mainly been used where the numerical quantification of WDR is concerned.

3.2.3. Parameters

The catch ratio (and hence the WDR) is a complicated function of space and time. The six basic influencing parameters for the catch ratio as defined in Eq. 3.4 are: (1) building geometry (including environment topology), (2) position on the building facade, (3) wind speed, (4) wind direction, (5) horizontal rainfall intensity and (6) (horizontal) raindrop-size distribution. In reality, the turbulent dispersion of raindrops is an additional parameter, although it is often neglected in numerical modeling efforts. The parameters wind speed (m/s) and wind direction (degrees from north) are usually given as their values at 10 m height in the undisturbed flow (U_{10}, φ_{10}) and are then called reference wind speed and reference wind direction. U_{10} is the mean streamwise horizontal wind speed and φ_{10} is the direction from which the wind is coming. The parameter horizontal raindrop-size distribution $f_h(d)$ (m^{-1}) refers to the raindrop-size distribution falling through a horizontal plane (in the undisturbed flow field). It is important to note that it differs from the raindrop-size distribution $f(d)$ (m^{-1}) given by the formula of Best (1950). The latter is a size distribution in a volume of air while the former is a flux through a horizontal plane. This difference is explained in Blocken and Carmeliet (2004). It is often overlooked in WDR studies. Stopping distance, another parameter involved in the catch ratio, is defined as the distance traveled by a drop as a result of its inertia once the wind flow ceases (Fuchs 1964).

3.2.4. Equation of motion of a raindrop

Fig. 3.2 illustrates the forces that act on a raindrop in a wind-flow pattern: the gravity force $\vec{G}$, the Archimedes force $\vec{F}_{ARCH}$ and the drag force $\vec{D}$. The wind-velocity vector $\vec{v}$ and the raindrop-velocity vector $\vec{v}_{DROP}$ are additionally indicated because they determine the direction and magnitude of the drag force, as the drag force is determined by the relative flow of air around the raindrop.

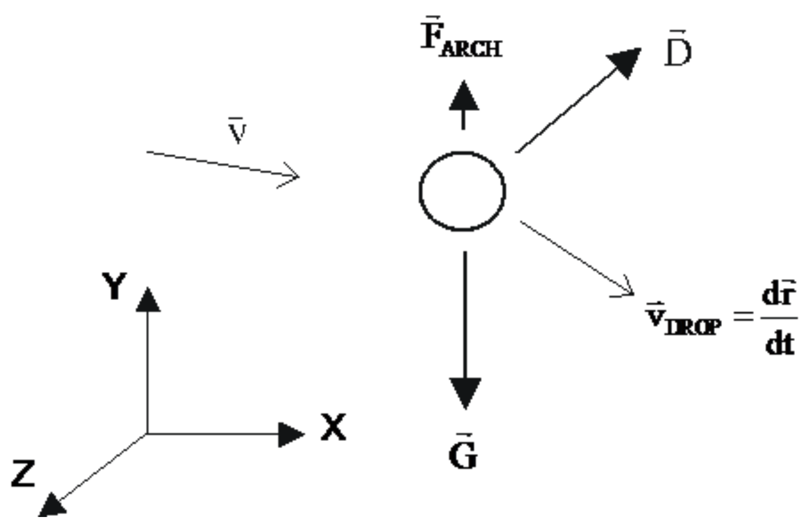

Figure 3.2. Forces acting on a raindrop in a wind-flow field. The wind velocity vector $\vec{v}$ *and the raindrop velocity vector* $\vec{v}_{DROP}$ *are additionally indicated.*

The equation of motion of a raindrop, moving in a wind-flow field characterized by a velocity vector $\vec{v}$ is:

$$\left(\frac{\rho_w - \rho}{\rho_w}\right)\vec{g} + \frac{3\mu}{\rho_w d^2} \cdot \frac{C_d \, Re_R}{4} \cdot \left(\vec{v} - \frac{d\vec{r}}{dt}\right) = \frac{d^2\vec{r}}{dt^2} \tag{3.6}$$

where Re_R is the relative Reynolds number (referring to the airflow around the raindrop):

$$Re_R = \frac{\rho d}{\mu}\left\| \vec{v} - \frac{d\vec{r}}{dt} \right\| \tag{3.7}$$

and ρ_w is the density of the raindrop, ρ the density of the air, g the gravitational acceleration, μ the dynamic air viscosity, d the raindrop diameter, C_d the raindrop drag coefficient, $\vec{r}$ the position vector of the raindrop in the xyz-space and t the time co-ordinate.

3.3. Raindrop Size Distribution

The raindrop size distribution (RSD) of a particular rain event refers to the measurements of raindrops in that event. Marshall and Palmer classify N_D as the number of raindrops per diameter as defined by the equation,

$$N_D = N_0 e^{-\Lambda D} \tag{3.8}$$

where N_D is the number of raindrops per diameter size (D), N_0 is the value of N_D for D=0 and Λ is given as,

$$\Lambda = 41R^{0.21}\ cm^{1} \tag{3.9}$$

where R is the rate of rainfall in mm/hr. In his 1950 publication, A.C. Best presents two experimental methods most used by researchers to determine drop size distribution. At the time, the most popular method was known as the “filter paper” method. This method required the use of absorbent filter paper that upon contact with liquid stained the paper, allowing for measurement and interpretation of the raindrop sizes. The other method presented, referred to as the flour method, required raindrops to fall into pans of sifted flour. Following baking and passing through graded sieves, the dough pellets formed by the raindrops were then measured (Best 1950). It should be noted that when using the two abovementioned methods, results are for raindrops as they impact the ground; however raindrop size distribution in air is the intended result (Best 1950). Further validation of raindrop size distribution has been completed by various other researchers; however, Blocken and Carmeliet’s ‘A Review of Wind-Driven Rain Research in Building Science’ repeatedly references the use of the empirical formula of A.C. Best, in most cases the formula adopted for raindrop size distribution (Blocken 2004). Raindrop size distribution is presented as volume of drops of a given size, rather than the number of drops of a particular size (Best 1950). The following equations are used in the determination of raindrop size distribution in accordance with the Best model,

$$1 - F = e^{-(x/a)^{2.25}} \tag{3.10}$$

$$a = AI^p \tag{3.11}$$

$$W = CI^r \tag{3.12}$$

where F is the fraction of water in the air comprised by drops with diameter less than x (mm), I is precipitation rate measured in mm/hr and W is the amount of water per unit volume of air measured in mm^3/m^3. Values A, C, p, r and n are constants with mean values of 1.30, 67, 0.232, 0.846 and 2.25, respectively. While there have been additional formulas used for raindrop size distribution (i.e. Marshall and Palmer, 1948; Ulbrich, 1983; Willis and Tattleman, 1989), Best’s model continues to be the most widely used RSD.

3.4. Terminal Velocity of Fall for Raindrops

Introduced in the 1949 publication of *The Terminal Velocity of Fall for Water Droplets in Stagnant Air*, Gunn and Kinzer presented an experiment involving two electrically insulated inducing rings, positioned in a grounded cylindrical shield that measured the time it took for an electrically charged droplet to fall from one ring to the other, set at a known distance apart. From these tests, fall velocity was determined as the product of the time and distance between the inducing rings. The terminal, or fall, velocity for a solid sphere requires the use of the gravitational force, G,

$$G = \frac{1}{6} g \pi d^3 (\rho_s - \rho) \tag{3.13}$$

where G is the downward gravitational force, g is the acceleration due to gravity measured in cm/sec^2, d is the diameter of the droplet (sphere) in cm, ρ_s is the density of the droplet (sphere) in gm/cm^3, and dynamic force, F,

$$F = \frac{1}{2}\rho V^2 Sc \tag{3.14}$$

where F is the force acting opposite of the direction of motion of the droplet (sphere), ρ is the density of the surrounding fluid in gm/cm^{3,} V is the velocity of the droplet (sphere) measured in cm/sec, and S is the projected area of the sphere measured in cm^2.

Equating the gravitation force and dynamic force produces an equation that yields the terminal velocity of a sphere, in this case a single water droplet.

$$V^2 = \frac{4}{3} gd(\rho_s - \rho)/\rho c \tag{3.15}$$

However, error associated with using the abovementioned formula may occur because rain droplets do not remain rigid spheres as they fall through the atmosphere to the ground. Deformation from aerodynamic forces, vibration and spin cause departure from the spherical geometry commonly assumed with rain droplets (Gunn and Kinzer 1949). From prior research, it has been noted that for rain droplets below a certain size, the aforementioned formula pertains (Best 1950). However, once raindrops begin to deform, that formula is no longer valid. C.N. Davies' research, reported by Sutton (1942) and published by Best (1950) introduced an equation with the ability to represent those droplets,

$$V = A_0\{1 - e^{-(d/a)^n}\} \tag{3.16}$$

where A_0, a and n are constants, V is the terminal velocity in cm/sec and d is the raindrop diameter in mm. Values for A_0, a and n were determined through trial and error to be 943, 1.77 and 1.147, respectively (Best 1950).

3.6. Hyperfine Clustering of Raindrops

Through research conducted by Jameson, Kostinski and Kruger, further knowledge into clustering of raindrops was achieved. Past studies limited drop counts to one minute, which according to these researchers spatially corresponds to ranges of a few hundred to several hundred meters (Jameson, Kostinski, and Kruger 1999). Delving deeper into the uncertainty of raindrop clustering, Jameson, Kostinski and Kruger took the one minute drop count and shortened it to a one second drop count using a video disdrometer. At both drop count time intervals, clustering was observed, thus suggesting that clustering occurs at even smaller spatial scales than originally assumed, ranging from a few meters to several hundreds of meters. Jameson et. al posed the question "is there some resolution at which clustering is no longer apparent"? This required looking at not only a 0.1-s drop count interval, but shortening that interval to 0.01-s, as well (Jameson and Kostinski 2000). The authors denote that there is a correlation between the clustering of raindrops of a single size and that of clustering among raindrops of different sizes. Jameson, Konstinski and Kruger have published a series of papers, *Fluctuation Properties of Precipitation. Parts I-VI*, in which the statistical methods used to determine these observations may be found.

3.7. Splashing, Runoff, Evaporation and Absorption

Factors such as droplet diameter, impact angle, impact speed, etc. are common variables affecting the behavior of a raindrop when it impacts a porous surface. Upon impact, raindrops may either spread, splash, bounce, absorb or evaporate, depending on the aforementioned variables (Abuku et al. 2009). It should be noted however, that raindrop behaviors do not relate to one another through comparison of time. Spreading, splashing and bouncing are all processes that happen within a few milliseconds of a raindrop impacting the surface; however, absorption and evaporation of a raindrop are processes that may last on the range of at least 100 times longer than their counterparts (Abuku et al. 2009). For experimental results regarding raindrop impact, the reader is directed to the works of (Abuku, Janssen, Poesen and Roels 2009). Only a brief mention of the impacts of raindrops on the building façade has been mentioned here.

Runoff of wind-driven rain on building façades is a phenomenon that in olden days occurred much less often than it does today. Take for instance buildings built in the 18th century. From examination of exterior façades of historical buildings (i.e. Regent House, Trinity College, Dublin) it can be seen that the detailing of the façade threw water off of the building, sheltering part of the building thus preventing absorption and penetration into the façade. This in turn reduced the amount of wind-driven rain able to infiltrate the exterior, thus lessening the structural damage that could have occurred. (Mulvin and Lewis 1994). Wind-driven rain, in general, may cause various other problems, such as, water penetration, frost damage and structural cracking, to name a few. Wind-driven rain runoff also may cause surface soiling patters on the building façade (Blocken and Carmeliet 2004).

The impact of wind-driven rain on a building façade presents the possibility of absorption; given the façade is porous (Abuku, Janseen, Poesen and Roels 2009), along with other variables such as droplet diameter, impact velocity and angle, etc. Not only can absorption occur in the outer façade of the building, it can also damage the interior. Investigation of impact, absorption and evaporation of raindrops acting on building façades has been performed both experimentally and numerically, explained through the comparison of a one-dimensional simulation at the façade considering a uniform, continual rain load to that of a three-dimensional simulation using random and discrete wind-driven rain (Abuku, Janssen, Poesen and Roels 2009).

3.8. Effect of Rain on Wind Loads

Choi (2008) divided the study of wind-driven rain into five steps: (1) the wind flow pattern around the building, further quantifying the wind velocities; (2) trajectories of various diameter size raindrops; (3) wind-driven rain intensities at different locations of the building façade; (4) estimation of the mass of rain water and (5) the average pressure due to wind-driven rain, calculated from the change of momentum of the raindrop. A more detailed explanation of each step may be found in (Choi 2008); however, the results of this study indicated that even with a high rainfall intensity (e.g. 200 mm/hr), the largest increase in average pressure was only approximately 2.2%. Thus from results like these, an observation may be made that even with a high intensity, wind-driven rain does not appreciably change the wind loading on buildings.

Chapter 4. WDR Effects on Building Performance

Authors: Goldsmith, Haefli, Fewless, Williams

Note: Additional information to be provided by Chuck Goldsmith on June 21

Multiple factors influence the deterioration of the building envelope. Driving rain, otherwise known as wind-driven rain is a climatological cause of dilapidation. Wind-driven rain has adverse effects on the building envelope causing deterioration of the façade and compromising the integrity of the structure and its contents. Cycles of intense moisture on components may lead to structural cracking which may not be cause for concern for failure, but may require remediation for aesthetic purposes. Water intrusion at the mortar-block interface and the subsequent freezing can lead to damaging stresses in masonry walls in cooler climates.

Wood framed structures represent a large portion of residential construction, for which protection from climatological effects is essential, precipitation in particular. As a result of water ingress into the building envelope, mold is likely to form if the conditions are favorable (Tariku et al. 2012). Of larger concern is the weakening of the structure if the intrusion is severe enough to cause rotting of wooden frame components. Water ingress through roof covers can lead to degradation of plywood sheathing to the point where collapse is imminent under the weight of a person walking over it.

Reduction of moisture content in building improves life expectancies of all building components including architectural, electrical and mechanical thus enhancing sustainability of building. The energy efficiency of a building may also be reduced by the increased moisture content of the building due to water intrusion. Electrical components specifically can be damaged beyond repair by the intrusion of water into critical areas such as outlets and circuit breakers.

Runoff impacts the weathering of the façade, and can be controlled by the proper selection of materials and patterns protruding from the surface. The extent of deterioration is largely dependent on the geometry of the façade, surface material properties, and the local climatology (El-Shimi 1980). Extended exposure to wind-driven rain may lead to discoloration due to mold or efflorescence. Decorative architectural features, protrusions and recesses in the façade also aid in its ability to shed water, thus reducing the likelihood of staining.

High levels of water ingress which may follow wind damage during extreme events such as hurricanes or super-cell thunderstorms can lead to extreme interior damages such as mold and mildew growth. Not only does this include the cost of remediation, but the costs incurred by the loss of functionality of the building and its occupants during the remediation period. The following is a discussion of individual components based on driving rain effects and resistance.

Soffit

Soffits are an essential component of residential construction designed to satisfy two purposes: (1) allow air to circulate through the attic space of a home and (2) keep undesirable articles from entering the attic space, particularly precipitation. This report focuses on the latter. Soffits perform well during thunderstorms, where long periods of strong winds are not typical. However, in high wind events such as hurricanes, both failure due to high wind and water intrusion due to differential pressures have been observed. Water ingress due to undesirable performance can result to mold and mildew growth in the attic space. Rotting of roof sheathing panels and dilapidation of interior may also occur.

Precast façade panels

Precast panels are typically intended for aesthetics only, with their stiffness typically not accounted for in the MWFRS design. While they provide satisfactory performance in deterring water ingress, discoloration and staining of the surface detracts from the appearance of the building. The staining of the precast panels is primarily due to the surface runoff patterns observed during driving rain. The surface runoff patterns are almost completely dependent upon the geometry of the precast panels. A qualitative analysis was performed, and recommendations made to minimize the staining of the building façade, the majority of which advocate proper detailing of windows and projections to control water runoff (El-Shimi, 1980).

Windows

Water travels through open orifices on windows that are not completely sealed due to the pressure gradient across the threshold. Windows are not designed to be completely water proof at design pressures, instead only to remain intact at these loads. In hurricanes, unprotected windows risk failure due to wind-borne debris. Coupled with the wind-driven rain, severe water intrusion can damage a building interior and contents, leading to the high costs of restoration. If the frame is not properly detailed during construction, water can also enter through voids in between the window frame and the opening. Cracks in caulking and sealant around the frame elevate the risk of water migrating into the building. Results from static pressure testing suggest that single hung windows perform slightly better than horizontal sliding windows in regards to driving rain (Masters, 2010).

Discontinuous Roof Covers

Discontinuous roof cover systems such as asphalt shingles and clay tiles are susceptible to wind driven rain as the approaching flow in high winds can drive the rain up the roof, against the natural water shedding tendency for these systems. Vapor barriers are installed beneath discontinuous roof covers to prevent any moisture that does intrude from collecting on the wood sheathing panels. Significant reductions in wind resistance and gravity loads can occur with water that begins to rot the sheathing panels. Attic and roof vents are also naturally susceptible to the effects of wind-driven rain, allowing moisture to enter the attic space which can foster mold in mildew growth in certain climates.

Wall joints and cracks

Open area on the exposed building such as cracks or improperly sealed joints can allow water intrusion. Residential homes constructed with stucco can be susceptible cracks due to differential settlement in the foundation. Water ingress may occur with cracks less than 0.39 mm wide (Mullens et al., 2006). Poor masonry construction practices facilitate the entrance of water into the building envelope as well; recommendations to correct this trend are provided in a report by Mullens et al., 2006. Unsealed orifices on the exterior of the façade such as outlets or faucets can also allow water ingress due to the pressure gradient across the exterior wall in long duration wind-driven rain events, particularly hurricanes.

Chapter 5. Research

Authors: Chowdhury, Dao, van de Lindt, Masters, Pinelli

5.1. Overview

Over the course of the 20th century into the 21st century, knowledge of wind-driven rain and its role in various professions has increasingly expanded. Advances in measurement systems, rain gauges and theory, to name a few, have enabled researchers to further their studies of a topic with unanswered questions. Blocken and Carmeliet (2004) present a thorough review of wind-driven rain and how it plays a key role in the area of building science. The following sections in this State of the Art Report on Research will discuss many of the same topics presented in the Blocken and Carmeliet (2004) review.

5.2. Rain Deposition

5.2.1. Wind-driven-rain gauges and measurements

The experimental methods consist of measuring WDR with WDR gauges. Similar to the well-known rainfall gauges that are equipped with a horizontal aperture to measure rainfall, WDR gauges are characterized by a vertical aperture to collect the amount of WDR (Fig. 5.1). Two types of measurements can be distinguished: (1) measurements of the free WDR (i.e. the WDR that is not influenced by the presence of buildings or other obstructions) and (2) measurements of the WDR on buildings. Free WDR gauges are placed in "free-field conditions" on a post to obtain a general idea of the WDR conditions, whereas wall-mounted WDR gauges are intended to obtain specific information of the WDR exposure at certain positions of the building facade.

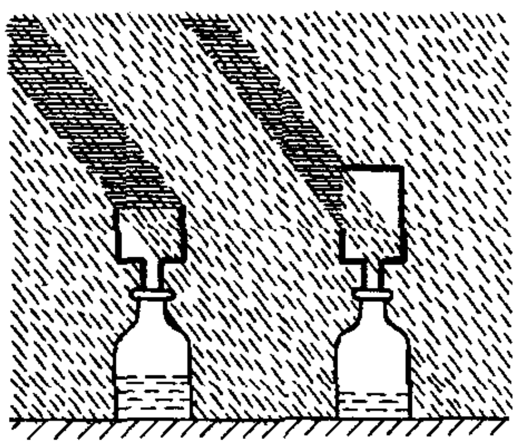

Figure 5.1. Horizontal-rainfall gauge with a horizontal aperture to measure horizontal rainfall (left) and wind-driven-rain gauge with a vertical aperture to measure wind-driven rain (right) (from Svendsen 1955).

The first WDR gauge for measurements on buildings was probably that employed by Holmgren in 1937 in Trondheim, Norway. Later, in 1943, Nell positioned two WDR gauges at the facade of his house in Voorschoten, the Netherlands (Basart 1946). Their example was followed by many researchers in other countries. The gauges used were all of a similar basic design (Fig. 5.2). It was plate-type gauges consisting of a collection area and a reservoir. The collection area is made up of a shallow tray (collection plate or catch area) of some material, shape and size and is fixed at the building surface. It has a raised rim around the perimeter to prevent the collection of water from outside the plate. The lowest point of the tray is drilled and tapped to accept a tube leading to the reservoir. The volume or weight of the collected rainwater in the reservoir is manually or automatically registered at regular intervals.

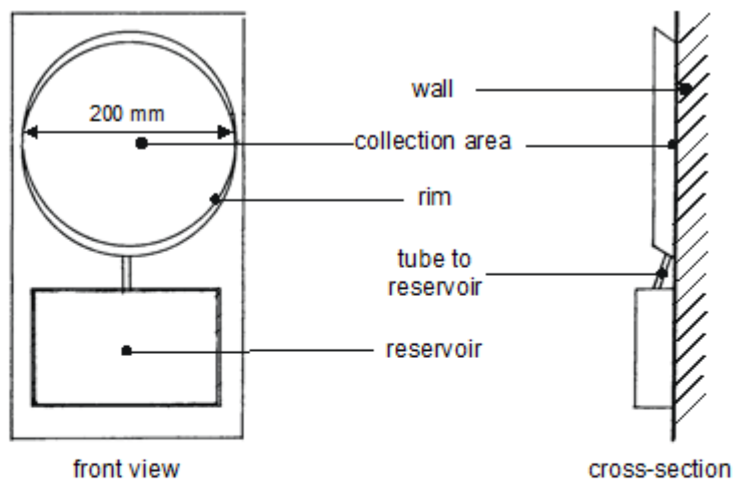

Figure 5.2. Wall-mounted plate-type wind-driven-rain gauge where the collection area fits flush with the vertical facade surface (from Blocken and Carmeliet 2004).

Measurements by wall-mounted gauges have revealed several features of what is nowadays called the "classic" wetting pattern of building facades (Blocken and Carmeliet 2004): (1) The windward facade is wetted whereas the other facades remain relatively dry, (2) At the windward facade, the wetting increases from bottom to top and from the middle to the sides. Typically, the top corners are the wettest, (3) The WDR intensity at a given position increases approximately proportionally with wind speed and horizontal rainfall intensity.

5.2.2. Accuracy of wind-driven-rain measurements

WDR gauges are not industrially manufactured and there exists no standard on their design. As a result, there are almost as many types of WDR gauges as there are researchers using them. The present discussion is focused on the plate-type WDR gauges that are used for measurements on buildings. The individual plate-type gauges differ by material, shape and size of the collection area. Detailed studies on WDR measurement accuracy were performed by Högberg et al. (1999)

and Blocken and Carmeliet (2005, 2006). These tests indicated that measurements by different WDR gauges can provide very different results, up to a factor 2 in captured WDR sum. The main reason is the so-called adhesion water error (Blocken and Carmeliet 2005). During and after a WDR event, there is always an amount of water (individual drops or water film) adhered to the collection plate. This amount is not collected in the reservoir and hence not measured. After and to a lesser extent also during rain, this adhesion water evaporates. Other error sources than those arising from the characteristics of the collection area are considered to be of lesser importance but cannot be excluded. They comprise (1) evaporative losses from the reservoirs, (2) splashing of raindrops from the collection area, (3) condensation on the collection area and (4) wind errors, meaning smaller catches due to the disturbance of the wind flow by the gauge body. Based on these findings and on adhesion water measurements, Blocken and Carmeliet (2005) designed a new WDR gauge, made from polymethylmethacrylate (PMMA), which is the material type that produced the lowest adhesion water errors from a wide range of materials tested. Nevertheless, it is always important to estimate the errors in WDR measurements. A methodology for WDR error assessment was presented and applied by Blocken and Carmeliet (2005).

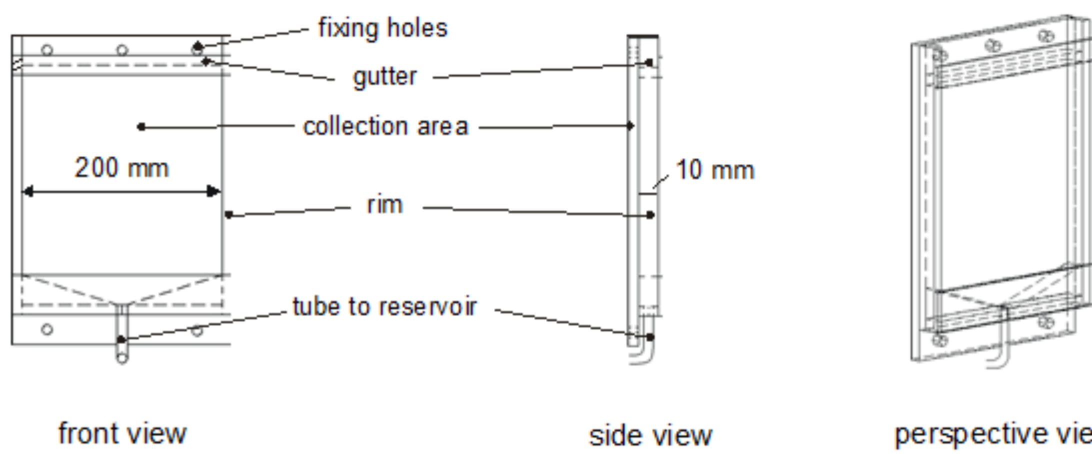

Figure 5.3. New design of wind-driven-rain gauge (Blocken and Carmeliet 2005). The gauge is made of PMMA with a collection area $A = 0.2x0.2\ m^2$.

5.2.3. On-site measurements of wind-driven rain on buildings

An overview of different WDR gauges and of WDR measurements on buildings can be found in Blocken and Carmeliet (2004). An example of WDR measurement results on the VLIET test building, in Leuven, Belgium, is shown in Fig. 5.4.

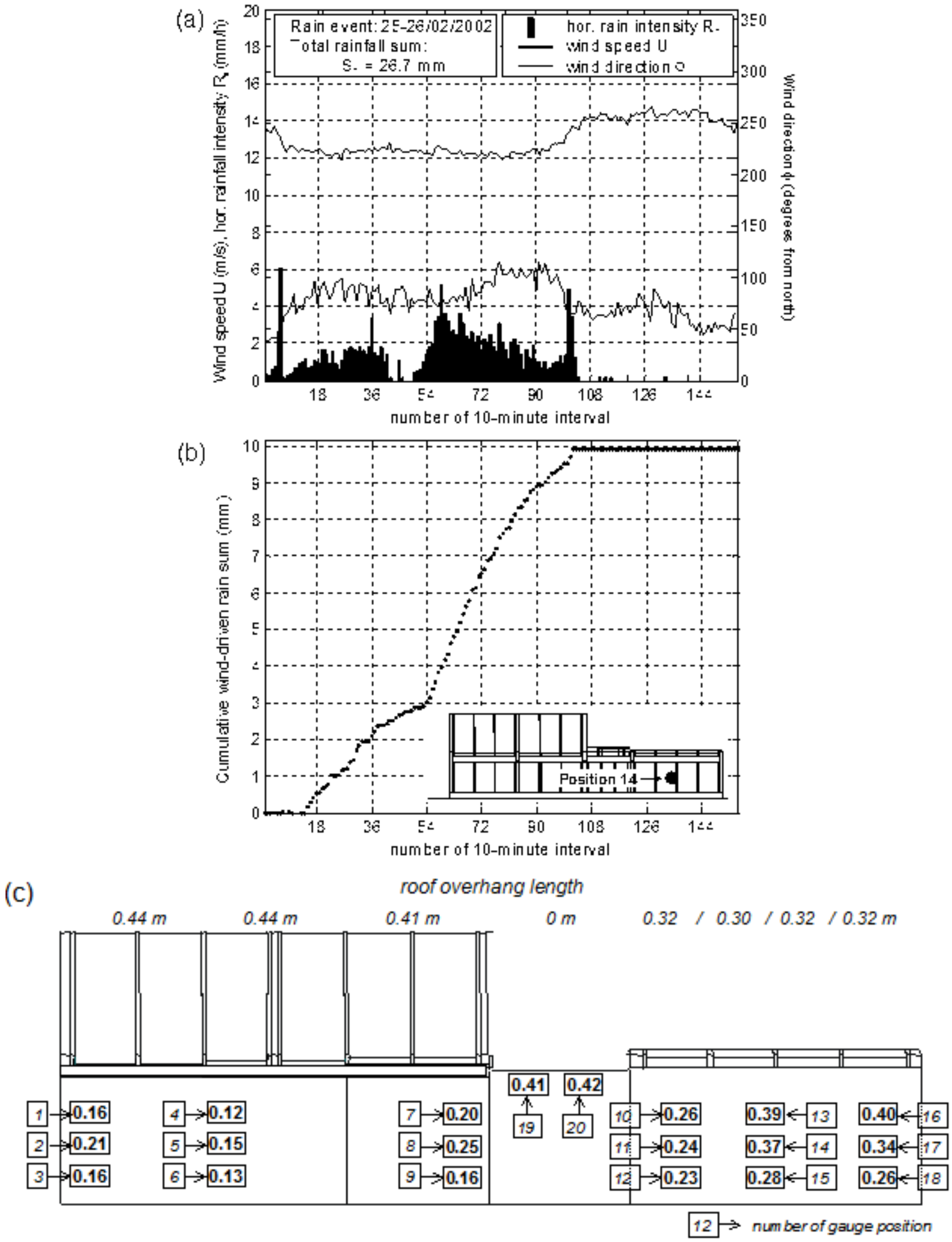

Figure 5.4. Measurement results of wind-driven rain on the south-west facade of the VLIET test buildings. (a) Horizontal rainfall intensity, wind speed and wind direction measured during the rain event (and averaged on a 10-minute basis). Total rainfall sum Sh = 26.7 mm. (b) Temporal distribution of the wind-driven-rain sum Swdr during the rain event at position 14. (c) Spatial distribution of the ratio Swdr/Sh (total wind-driven-rain sum to total horizontal rainfall sum) for the rain event (from Blocken and Carmeliet 2005).

The meteorological data recorded in the period from 25 to 26/02/2002 are shown in Fig. 5.4a. The rainfall intensity is light to moderate and the total horizontal rain sum S_h = 26.7 mm. Wind speed is situated between 2 and 6 m/s and the wind direction during rain is approximately south-west. Fig. 5.4b illustrates the temporal distribution of WDR at gauge position 14. During the first 130 minutes of the rain event, no WDR is registered. The roof overhang appears to effectively shelter position 14 during the low-wind-speed conditions in the beginning of the rain event. As the wind speed increases and after some delay (gauge collection area first collects adhesion water), WDR is starting to be registered and the WDR catch increases at a more or less constant rate. Fig. 5.4c shows the variation of the ratio of the total WDR sum S_{wdr} to the total horizontal rainfall sum S_h (= 26.7 mm) for the rain event across the facade. The following observations are made:

1. The highest values are found at the top edge of the terrace module (no roof overhang – gauges 19-20).
2. For the flat-roof module: The flat-roof module clearly catches more WDR than the sloped-roof module, because of the wind-blocking effect (Blocken and Carmeliet 2006b). According to the classical wetting pattern of building facades as discussed in section 5.2, the WDR sum is expected to increase from bottom to top and from the middle to the corner of the facade. Despite the presence of the roof overhang, the increase from bottom to top is clear, although it would have been more pronounced without the roof overhang present. Concerning the increase of the values from the middle to the corner of the facade, it is noted that the values at gauges 13-15 are rather high compared to those at gauges 10-12 and 16-17. This is due to the 0.02 m (!) difference in roof overhang for this small part of the facade. This difference has been found systematically for all rain events with wind-speed data of similar or lower magnitude (the wind speed largely determines the effect of the overhang).
3. For the sloped-roof module: The increase of the values from bottom to top of the facade is only present for the lower two gauges (2 and 3, 5 and 6, 8 and 9). The gauges near the top of the facade are significantly sheltered by roof overhang.

The error for the total WDR sum is estimated: E_{wdr} = 5 x 0.10 mm = 0.5 mm. The error for the ratio S_{wdr}/S_h is e_{wdr} = 0.5 / 26.7 mm = 0.02.

5.2.4. Physical simulation of wind-driven rain in wind tunnels

The possibility of wind-tunnel modeling of WDR on buildings was considered by Flower and Lawson (1972) and by Rayment and Hilton (1977). They mentioned the difficulties involved. Flower and Lawson concluded that it should be possible to predict impingement rates on buildings by suitable laboratory tests. Rayment and Hilton visualized the movement of raindrop trajectories around a building model using bubbles. Only one attempt of WDR quantification tests is known to the authors. An elaborate scaled wind-tunnel study has been performed at the Boundary Layer Wind Tunnel Laboratory (BLWTL) (Inculet and Surry 1994, Surry et al. 1994, Inculet 2001). Nozzle arrays were installed in a boundary-layer wind tunnel (Fig. 5.5). Building models at a scale of 1:64 were constructed and placed in the wind tunnel. The wind speed and the raindrop sizes were scaled and WDR on the buildings was physically simulated. An important problem was determining the amount of WDR falling onto different positions on the models. Measuring WDR on small models requires the use of special techniques such as the electrostatic-sensor technique or the water-sensitive-paper method (Inculet and Surry 1994). In these experiments, the water-sensitive-paper method was used. This method consists of positioning pieces of water-sensitive paper on the building model. Each drop that falls on the paper leaves a stain. This way, a visual picture of the wetting pattern is obtained. The observed staining clearly confirmed the "classical" wetting pattern of WDR on buildings: (1) The windward facade is wetted whereas the facade that is parallel to the wind remains dry. (2) The top and side edges of the wide, windward facade are most exposed to WDR. Based on the wetting patterns, by counting and sizing each individual stain, an estimate of the amount of WDR falling onto different parts of the model was determined (Inculet and Surry 1994). The difficulties in this type of demanding experiments were accurately described by Inculet and Surry (1994). They reported that the major drawbacks are the very limited time of the rain shower (individual drops must remain distinguishable on the paper) and the fact that the quantitative analysis (counting and sizing of individual stains) is very labor-intensive and therefore not possible for all locations and for a large number of tests. It was also mentioned that the short duration of the tests (5 to 10 seconds) might result in a considerable variability from test to test. Another difficulty was providing a homogeneous distribution of rain from the nozzles (meaning that in an empty wind tunnel, the nozzle arrays should provide a uniform horizontal-rainfall-intensity pattern on the wind-tunnel floor).

Figure 5.5. Upstream view in the boundary-layer wind tunnel equipped with nozzle arrays at the ceiling for wind-driven-rain simulation (© Inculet 2001, Boundary Layer Wind Tunnel Laboratory, University of Western Ontario, London, Ontario, Canada).

5.3. Modeling of hurricane interior losses due to water ingress in catastrophe models

Authors: Pinelli and Pita

This section focuses on modeling the effect of rain on buildings losses as performed in some catastrophe models. Catastrophe models are built to project insured hurricane losses over large portfolios composed of up to several hundreds of thousands of buildings, so the rain intrusion problem is treated from a statistical point of view. Because most catastrophe models are proprietary, the Florida Public Hurricane Loss Model (FPHLM) (Pinelli et al., 2011; Hamid et al. 2011) is used as a case study, and the methodology presented here belongs to that Model.

5.3.1. Importance of interior damage

In many buildings the value of what is inside them (i.e. their interior including partitions, fixed furniture, ceilings, doors, flooring, finishing, etc.) approaches or surpasses that of the envelope and structure. The main contributor to interior damage is wind-driven rain (Mileti, 1999) as many post storm surveys have shown (US-HUD, 1993; Sheffield, 1994; Smith, 1994; Crandell, 1998; Crandell et al., 1993, 1994; Sparks and Bhinderwala. 1994; Sparks et al., 1994; van de Lindt et al., 2007). Interior damage caused mainly by water intrusion, might also trigger contents damage and contribute to time related expenses. As such, interior damage represents a significant fraction of the total hurricane damage sustained buildings. Amirkhanian et al. (1994) studied insurance claims from hurricane Hugo and found that on average direct wind damage, and total damage represented 6.5% and 25.5% respectively of the insured value of the houses.

Consequently, it is crucial that any method to assess building vulnerability has a robust module to estimate the damage caused to the interior. The estimation of interior damage in vulnerability assessments of residential and non-residential buildings is challenging because of the complexity of the problem and the difficulty to validate any predictions. For that reason, the estimation of interior damage has been traditionally determined, predominantly, by expert opinion.

For example, Unanwa et al. (2000) proposed a method to assess interior damage with fault-trees. The authors gathered expert-supplied probabilities of interior damage conditioned on the failure of the exterior components. The expert probabilities indicate that interior damage is more likely to happen with breached openings and exterior wall—which are very similar—than with breached roof cover.

Nevertheless, more sophisticated methodologies based on engineering approaches, which include physical models, have been developed more recently. When physically modeling the effect of rain on the interior damage of a population of buildings subjected to a hurricane, three questions need to be addressed: how much rain is impinging on each building? How much of the impinging rain penetrates into each building? How much damage the rain intrusion produces inside each building?

HAZUS (FEMA-HAZUS, 2006, p.7-7:7-11) proposes a simulation approach where the interior building damage is estimated as the maximum economic damage resulting from water intrusion from either roof cover, roof sheathing or openings. The water intrusion through these components is estimated with heuristic equations that account for the particularities of each damage mode.

The interior damage model of the FPHLM, (Pita et al., 2012), combines a phenomenological model of the hurricane wind and rain fields, leading to an estimation of impinging rain, with a physical or mechanistic model of water intrusion and interior damage. The methodology is summarized in the next sections.

5.3.2. Model of hurricane wind and rain fields

The first part of the interior damage module of the FPHLM consists in the simulation of a large number of synthetic hurricanes with the associated rainrate. The key features of the synthetic hurricanes are generated from sampling probability distributions of storm characteristics. The probability distributions were fitted to historical hurricanes data in the Atlantic Basin, and represent key storm features such as: central pressure difference, translation velocity, Holland-B parameter, and decay filling constant. When a complete set of storm parameters has been reached, the methodology defines the corresponding radially averaged rain rate and wind speed distribution (assuming that tangential wind is the full wind speed) associated with the constitutive parameters. The rain distribution is modeled with the R-CLIPER approach (Lonfat et al., 2007; Marks et al., 1993) which outputs an azimuthally averaged rain rate by unit of time (in/hr) at the ground floor level. The rain rate varies as a function of radius and maximum intensity of the storm. The wind speed is modeled after the approach defined by Holland (1980) which delivers a sustained gradient winds speeds V_g at 3,000 meters:

The modeled wind fields are asymmetric as a function of the latitude and the Coriolis force. The storm decay after landfall is modeled with the pressure decay pressure model proposed by Vickery (2005). The gradient wind speeds are converted from 3000 to 10 meters in two steps: (1) from wind speed at 3,000 meters to 300 meters in the eyewall region (Franklin et al., 2003); then calculate the wind speed at 300 meters to continuous distances from the eyewall (Axe 2003), and (2) use the log-law procedure (Simiu and Miyata, 2006) to convert from 300 meters to 10 meters. Last, the averaging time period is converted from 1 minute-sustained to 3 second-gust with appropriate gust factors (Vickery and Skerlj, 2005).

5.3.3. Model of impinging rain on generic buildings

The second part of the interior damage module estimates the rain impinging on generic buildings. The buildings were conceptualized in the simulation scheme as a set of 91 measurement locations in a plane, which record the passage of the modeled wind and rain fields. These locations are arranged horizontally equally-spaced by 10 kilometers to span the whole extent of the synthetic hurricane, which has 900 km diameter, and are scattered vertically to feature varying distances from the coast (see figure below). The stations are arranged in that manner to account for any hurricane heading to any position in a plane. At each station, the simulation records the time history of rain rate and wind speed as the simulation displaces each synthetic hurricane by discrete time-steps. The simulation accumulates the amount of impinging rain *IR* over the entire storm duration, along with the maximum wind gust speed experienced at the same station. The process is repeated for each hurricane. The complete simulation repeats 100,000 times. Subsequently a relationship is derived between the total impinging rain and the maximum peak wind gust speed that a station may experience.

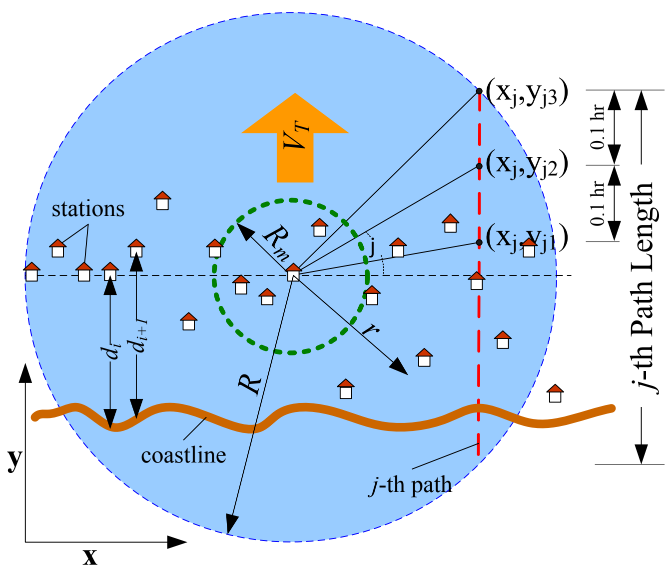

Figure 5.6. Variables of the simulation study performed to assess the correlation between rain and wind speed for the Florida Public Hurricane Loss Model. From Pita et al., (2012).

The total impinging rain rate IR_r is calculated as a function of the vertical rain rate (*rr*), the horizontal mean wind speed (V_h) at 10 m and the terminal velocity of the rain drops (V_t):

$$IR_r = rr \cdot V_h / V_t \tag{5.1}$$

The vertical rain rate (*rr*) is determined from the R-CLIPER model. The terminal raindrop velocity (based on Dingle and Lee, 1972) depends on the rain drop size (*D*), which in turn has a modified-gamma distribution N_D based on rain rate estimated from Willis and Tattelman (1989). The average raindrop velocity is computed considering the mass flux contribution of each drop size to the rain rate is computed as:

$$\overline{V_t} = \frac{\int V_t N_D \left(D^3 V_t\right) dD}{\int N_D \left(D^3 V_t\right) dD} \tag{5.2}$$

The Driving Rain Factor (*DRF*) is defined as:

$$DRF(rr) = \frac{1}{\overline{V_t}} \tag{5.3}$$

The R-CLIPER outputs an azimuthal average of rain rate as a function of radius to center of the storm. This output might include locations with very little or no rain. As such, the *DRF* could be highly biased if based solely on an average rain rate, since the terminal velocity increases with drop size, which in turn increases with rain rate. To overcome this shortcoming, the methodology calculates an effective *DRF*, which is an average of the *DRF* weighted by the distribution of rain rates that contribute to the average rain rate estimated by R-CLIPER:

$$\overline{DRF}\left(\overline{rr}\right) = \int DRF(rr)\, g\left(\overline{rr}, rr\right) drr \tag{5.4}$$

where g is the rain rate distribution, assumed lognormal from Tropical Rainfall Measuring Mission (TRMM) observations that yield a given mean rain rate, $\overline{rr}$ (Marks et al., 1993; Lonfat et al. 2004). The range of the mode and frequency of the mode are estimated using probability distribution functions from Lonfat et al. (2004) for the entire range of possible radii and storm intensity. These two parameters uniquely determine the distribution.
Eqn. (1) is then re-written as:

$$IR_r = rr \cdot V_h \cdot \overline{DRF} \tag{5.5}$$

The total amount of rain impinging on each station, *IR*, is found by integration of the impinging rain rate over the storm duration, between initial time of rain t_0 and final time of rain $t_.$

In addition to the total impinging rain *IR* during the event, the simulation algorithm registers the accumulated impinging rain IR_2 defined over the period ranging from the moment that a location experiences the peak wind to the end of the storm. The impinging rain accumulated prior to the maximum peak gust (IR_1) is computed as the difference: $IR_1 = IR - IR_2$. The resulting accumulations are then probability distribution functions of impinging rain as a function of the peak 3-sec wind gust at 10 meters height. Figure shows the mean IR_1 and IR_2 as a function of peak three-second gusts at 10 m. It should be noted, however, that although rainfall and wind speed are correlated, it does not imply that they are linked by a causal relationship.

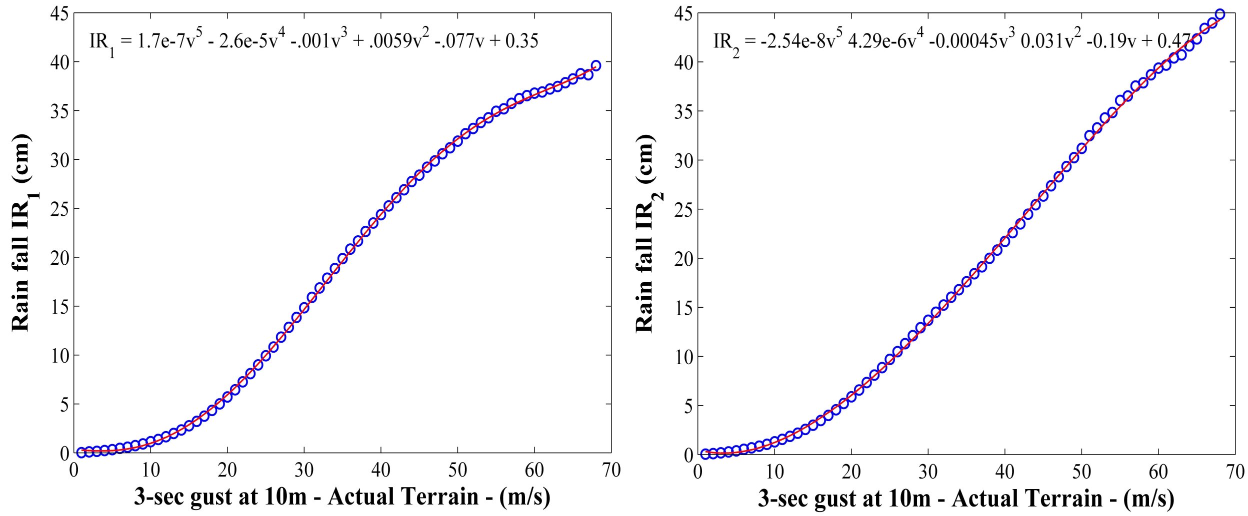

Figure 5.7. Mean accumulated impinging rains as a function of peak 3-second wind gust: (left) IR_1 from the beginning of the storm until the maximum wind, (right) IR_2 from the maximum wind until the end of the storm.

5.3.4. Model of water intrusion

The interior damage model must estimate the amount of water that ingresses into generic building types. The methodology is based on a Monte Carlo simulation procedure where for each simulation, a generic type of building is subjected to a 3 sec gust wind speed of varying maximum intensity, in any of 8 possible directions. For each simulation, an estimate of external damage is obtained resulting in breaches of the envelope, and the accumulated impinging rains IR1 and IR2 are sampled from the probability distributions of rainfall according to the 3 sec maximum wind speed the building is experiencing in that simulation.

The methodology assumes that water ingresses into the building through two sources: through defects in the envelope, and through the wind-caused breaches. In the case of building defects, water might ingress before and after the occurrence of the maximum wind speed (assumed to cause the breaches). The size of defects per component C_i is assumed to be a percentage d_{Ci} of the component area A_{Ci}.

The methodology has to modify the impinging rain estimated in the simulation described above to account for the actual rain that reaches the walls, by considering the influence that the geometry of the building plays. The rain admittance factor (*RAF*) described in section 6 of this report, measures the fraction of the approaching rain that strikes the building. Straube and Burnett (2000) and Blocken and Carmeliet (2010) suggest RAF = 0.2-0.5 for low-rise buildings and RAF = 0.5-1.0 for mid-/high-rise buildings. In addition, adjustment factors were proposed to account for the particularities of a building subjected to a rotating hurricane. These will be succinctly discussed below. So, the convolution of the breaches areas and construction defects by the impinging rain conveys the amount of water that enters the building. The accumulated height ($h_{C_i}^{d}$) of water penetration through defects d in component C_i is computed as:

$$h_{C_i}^d = \frac{k \cdot RAF \cdot \left[IR_1 \underbrace{\left(d_{C_i} A_{C_i}\right)}_{\text{Total Defects Area}} + IR_2 \underbrace{\left(d_{C_i} A_{C_i} S_{C_i}\right)}_{\text{Post-breach Defects Area}} \right]}{A_b} \tag{5.6}$$

while the accumulated height ($h_{C_i}^b$) of water penetration through breaches b, is computed with:

$$h_{C_i}^b = \frac{k \cdot RAF \cdot \left\lfloor IR_2 \cdot A_{C_i}^B \right\rfloor}{A_b} \tag{5.7}$$

defined by adjustment factor (k), rain admittance factor (RAF), accumulated impinging rain before and after maximum wind (IR_1 and IR_2), percentage of defects (d_{Ci}), area of component i (A_{Ci}), the building base area, (A_b), breach area of component i ($A_{C_i}^B$), and survival factor (S_{Ci}) for component $i = 1 - A^B{}_{Ci} / A_{Ci}$.

The adjustment factor k encompasses many effects attached to the key components that influence the water intrusion into buildings. The following list reviews the proposed coefficients.

- Adjustment for distribution of breaches and defects in walls as a function of the wind direction, f_{sim}: Impinging rain ingresses only through breaches and defects located in the windward wall. Each instance of damage occurs at a particular wind direction. But once the damage occurred, the wind will keep rotating and changing direction over the remaining duration of the storm. As a result, defects and breaches will progressively change from windward to leeward or vice-versa. The f_{sim} factor takes into account the variable exposure of any breach throughout the time history of the storm. It does not apply to the roof.

- Adjustment for projection of roof breach with respect to wind direction, $f_{RedRoof}$: This adjustment factor accounts for the orientation of the exposed roof breaches relative to the wind (Figure). If the wind is normal to the ridge, $f_{RedRoof}$= 1.0 (the vertically projected surface area of the breach exposed to impinging rain is maximum). If the wind is parallel to the ridge, $f_{RedRoof}$ is minimum. If the wind is at an angle with the ridge, $f_{RedRoof}$ is assumed to be the average value between the two previous cases.

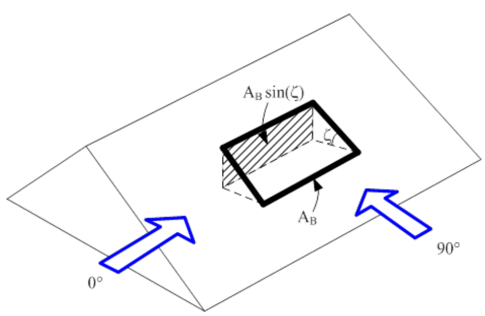

Figure 5.8. $f_{RedRoof}$ represents the breached roof area that is exposed to impinging rain as a function of wind angle of attack.

- Adjustment factor for runoff water, f_{RunWat}: this factor accounts for the water that drains on the external surfaces of the building and ingresses through the defects and breaches.

The factors listed above are derived mainly by engineering judgment, and as such should be revised every time new information becomes available, either through field or laboratory tests or computational fluid dynamic analyses. For example, recent efforts on modeling and measuring runoff water have been done by Blocken and Carmeliet, (2012). Other efforts underway at the Wall of Wind and elsewhere are reported in Section 6 of this report.

This approach estimates the amount of water that enters through each component of the envelope. The total amount of water at any given story is calculated by adding the contribution of all components for a given wind speed, and by estimating the water which percolates from story to story.

In multi-story low-rise buildings, a portion ρ of the water intrusion percolates downward from story to story. The values of percolation are based on engineering judgment, supported by calibrations of the model with insurance claim data, and thus can be updated when new research becomes available.

5.3.5. Interior Damage Model

The final step maps water inside the building to interior damage with a bilinear relationship, adopted from HAZUS (FEMA, 2006), where total interior damage is achieved for a certain threshold of height of accumulated water.

At every wind speed interval, this estimation of interior damage is then combined with the estimation of exterior damage to build vulnerability matrices and curves. These curves are useful not only in the insurance industry, but also in studies of risk management, and disaster mitigation.

Two building models consisting of 2-stories, gable roof, timber frame, multi-family buildings in Florida, one whose openings are protected with shutters and another whose openings are not, are used as an example illustrates the output of the model. **Error! Reference source not found.** (left) shows the relative contribution of each envelope component to total water intrusion (normalized to 100%) as a function of wind speed. The ordinate axis at a given abscissa value represents the relative proportion of the various components to whatever interior damage was accumulated, and does not imply 100% interior damage for all wind speeds. In the graph, at low speeds the water ingress is governed by the pre-existing defects. Roof, gable and wall sheathing damage modes become the main sources of damage as wind speeds increase. The only sources of damage that play a constant role in the interior damage generation throughout all the wind speeds range are the openings, especially windows. Furthermore, the openings contribute to damage in three stages: at low wind speeds, pre-existing defects are the predominant source of water intrusion; at medium wind speeds, the contribution of opening breaches increases; and, at higher wind speeds, the overall contribution of openings decreases as the water intrusion through wall sheathing failure predominates. In the figure below (right panel) the amount of water intrusion through breaches of the protected openings decreases with respect to those of the unprotected building.

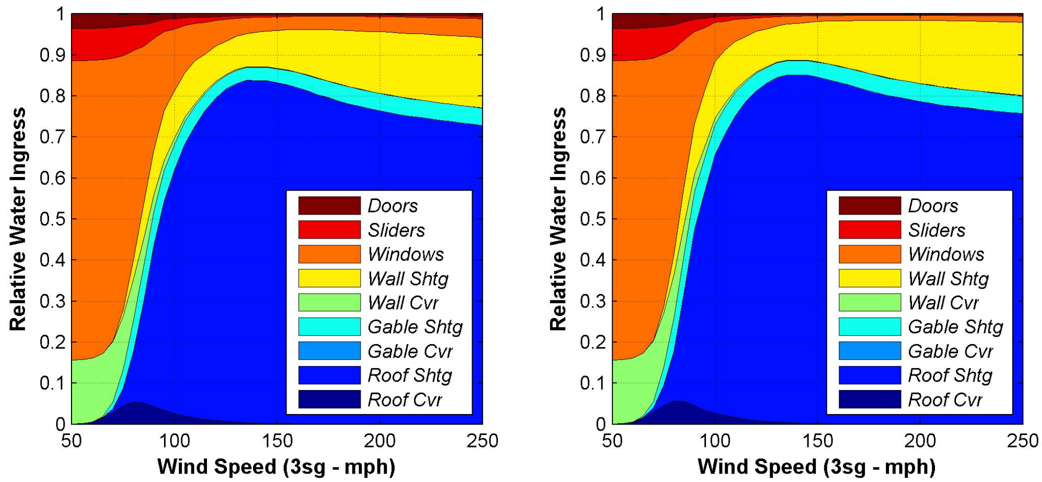

Figure 5.9: Normalized stacked areas graphs showing relative water ingress per component as a function of wind speed for 2-stories, gable roof, timber frame buildings. Left: building without shutters. Right: building with shutters. From Pita (2012).

Contents Damage and Time Related Expenses

Contents include anything in the building that is not attached to the structure itself. Time Related Expenses refer to increase in living expenses or to loss of rent revenue for owners of apartment buildings, which results directly from the interior damage and having to live away from the insured location.

As in the case of interior and utilities damage, both the contents damage and the time related expenses can be assumed to be a function of the amount of water that penetrates into the building and they are therefore a function of interior damage caused by water intrusion.

5.3.6. Future studies needed

Experimental studies are currently under way to evaluate more realistic values and distributions of the rain admittance factor, the runoff factor, and the mechanisms of water intrusion though breaches and defects. Additional studies are needed to better understand the extent of damage inside a building due to water intrusion and the mechanisms of water percolation.

5.4. Experimental Simulation

Polovkas and Thompson (1952) document one of the earliest known full-scale experiments directed at quantifying the rate of water ingress through the building components. The Storm Protection Laboratory (Figure 5.10a) was constructed at the University of Florida in 1946 to improve the performance of building components in severe weather conditions. The wind generator was generated by a hydraulically activated three-bladed airplane propeller spun by a 1300 hp nine-cylinder radial air-cooled aircraft engine (Figure 5.10b). The maximum achievable velocity was in excess of 67 m/s (150 mph). Simulated rain was introduced through a 1.8 m steel pipe grid with holes spaced at 5 cm on center (Figure 5.10c).

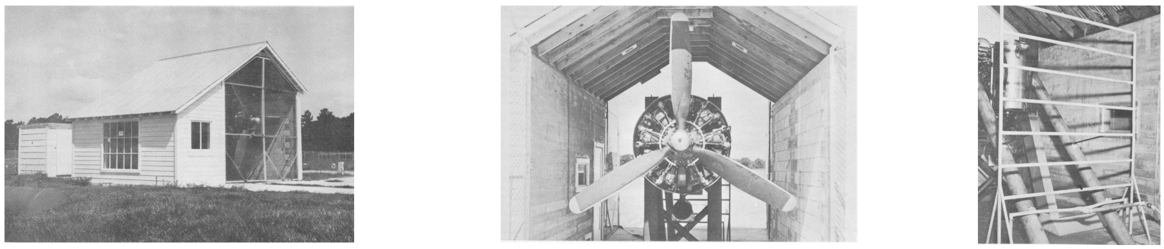

(a) Test facility (b) Wind generator (c) Spray rack

Figure 5.10. Storm Protection Laboratory at the University of Florida (Circa 1952)

The initial concept for the Wall of Wind, now a fixture at Florida International University, began at Clemson University in Clemson, South Carolina in the late 1990s. Lack of laboratory testing for full-scale structures, components and connections subjected to extreme wind patterns that produced repeatability led to the concept of the Wall of Wind (Kennedy). At the time, field data was available for wind loads on a low-rise building in open exposure from the Wind Engineering Research Laboratory at Texas Tech University; however, this data pertained to everyday weather conditions, not those of extreme weather events, such as hurricanes. Various models/prototypes were built and constructed, with the goal being able to produce a category five hurricane wind environment (Kennedy).

Over fifty years later, various experimental simulations have been constructed with the same intention as that of the Storm Protection Laboratory: to quantify water ingress through various building components. Florida International University's Wall of Wind (FIU WoW), also known as Phase I, began as a two-fan apparatus, capable of generating up to 120 mph winds with a water injection system able to simulate wind-driven rain. Phase II, known as the RenaissanceRe WoW, incorporates a six-fan system, generating 130-140 mph winds. This phase also includes a water injection system. Photographs of the phases may be seen in Figure 5.11.

(a) Wall of Wind, Phase I (b) RenaissanceRe Wall of Wind (Phase II)

Figure 5.11. Wall of Wind, Florida International University

In 2007, the University of Florida (UF) introduced the UF Hurricane Simulator, an apparatus equipped with eight hydraulically actuated vaneaxial fans, capable of simulating the turbulent wind and rain loads seen on structures during natural hazards such as hurricanes (Masters, Prevatt and Gurley 2010). Since its creation, the UF Hurricane Simulator, pictured in Figure 5.12, has been used to perform wind and wind-driven rain research on mock ups of residential homes as well as for a human perception study.

Figure 5.12. UF Hurricane Simulator.

Water ingress testing at the University of Western Ontario (UWO) Insurance Research Lab for Better Homes (IRLBH) utilizes relatively small pressure loading actuators. The actuators, regenerative blowers with high and low pressure sides, are controlled using a high speed servo motor, with the ability to produce up to 10 kPa of wind-induced pressure within a 1.2 m x 1.2 m air box (Van Straaten and Straube 2010). For water ingress testing, a spray rack system (according to ASTM E331-00) was utilized (Van Straaten and Straube 2010). For a more detailed description of the pressure loading actuators used for this study, the reader is directed to Kopp et. al (2010).

Based on the concept of the pressure loading actuator developed by UWO, UF constructed the High Airflow Pressure Loading Actuator (Second Generation) (Masters, Prevatt and Gurley 2010). This system is comprised of two 75HP Centrifugal Backward Inclined Class IV SWSI fans that may be operated in series or parallel. Capable of producing pressures associated with hurricanes, the HAPLA has been used to test various types of building components. A spray rack, positioned in the test chamber, allows for the use of the HAPLA in water ingress experiments as well.

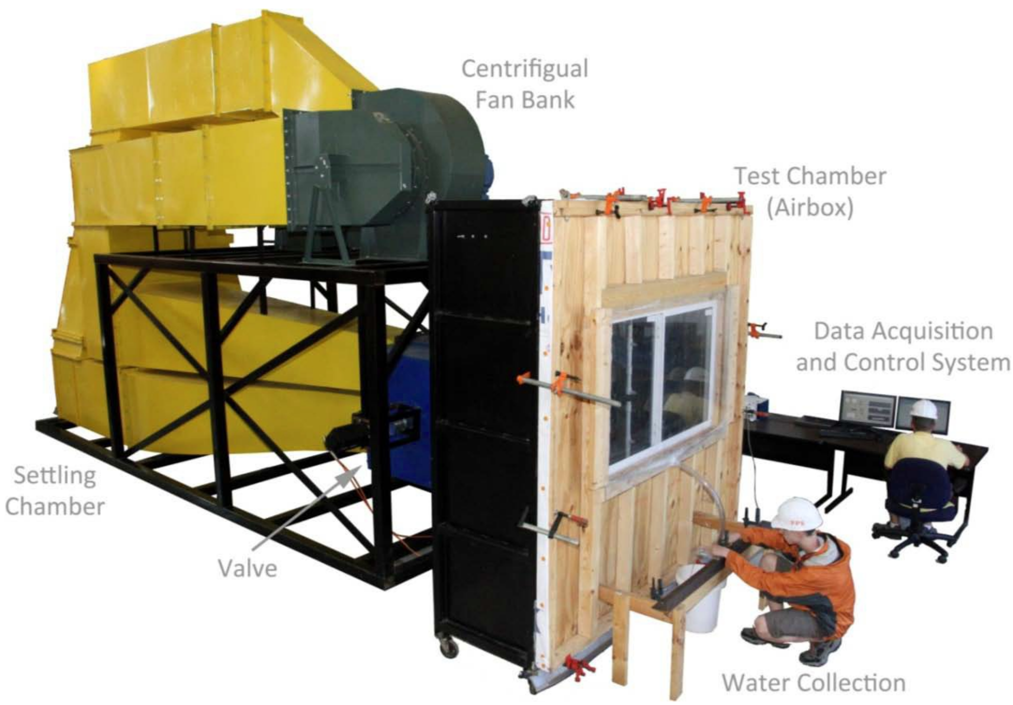

Figure 5.13. University of Florida High Airflow Pressure Loading Actuator

The Insurance Institute for Business & Home Safety (IBHS) performed a full-house wind-driven rain laboratory test in August 2011, the first of its kind, examining how WDR infiltrates the building envelope at various wind speeds and component and cladding options (Quarles et al. 2012). For this examination, a full-scale, 1,300 square foot duplex was constructed, with certain variables present or lacking on half of the full-scale house. In this test, for instance, sheathing joins on the roof deck were sealed on one side, but not on the other side. Use of open and covered soffit products simulated soffit being lost or remaining in place, respectively, during a hurricane event such as the test performed (Quarles et al. 2012). Results of these tests allowed for IBHS researchers to quantify the rate of water entering the full-scale house and to assess the amount of damage incurred on the structure and its contents (i.e. furniture).

5.5. Modeling of Water Ingress

Authors: Dao and van de Lindt

Full scale testing of water ingress has been conducted using many different building components. A varying factor in the studies is the pressure differential applied to the systems as well as the wind-driven intensity. Tariku et al. (2012) studied the effects of wind-driven rain on stucco wall systems, with emphasis on the moisture content of the interior of the structure as the determining factor in failure. Water penetration resistance of varying styles of residential windows was investigated by Salzano et al. (2010). This study was primarily focused on the performance of windows in tropical cyclone conditions. High differential pressures from the exterior to interior of the windows provide the necessary pressure gradient to allow water to travel up voids in the window assemblies and enter the structure. Fragility models are developed using test results, such as those mentioned above, case studies and theory. Probabilistic models are also developed to predict the amount of water ingress to take place for a given wind-driven rain event.

5.5.1. Overview of modeling of water ingress using a stochastic model

Fragility models of wind-driven rain intrusion into the building envelope are a relatively new concept, requiring the use of computation fluid dynamics, particle dynamics to determine rainwater trajectory, and nonlinear structural analysis (Dao and van de Lindt, 2010). Complexity is added to predicting water ingress through a building in general, by the amount of different components and assemblies that comprise the exterior of the building. To date probabilistic models have primarily focused on component based performance, due to the number of varying combinations possible in a given structure.

5.5.2. Wind-driven rain water intrusion fragilities

Fragility definition

Ellingwood et al (2004) provided a general definition for a fragility which can be expanded to include the water intrusion rate. Assuming the probability of exceeding a certain water intrusion rate is the desired quantity, the fragility can be expressed as:

$$P[(s-S)<0]=\sum_{\mathbf{h}} P[(s-S)<0|\mathbf{H}=\mathbf{h}]P[\mathbf{H}=\mathbf{h}] \tag{5.8}$$

where s is a predetermined limit for the rate of water intrusion, S is the rate of water intrusion into the building, and $\mathbf{H}$ is the hazard vector; which in the present case is $\mathbf{H} = [I\ V]^T$ where I is the rainfall intensity and V is the basic wind speed defined by ASCE7-10. The term $P[\mathbf{H}=\mathbf{h}]$ is the joint probability of two random variables: rainfall intensity I and basic wind speed V. The conditional probability $P[(s-S)<0|\mathbf{H}=\mathbf{h}]=Fr$ is defined as the water intrusion fragility.

Wind-driven rain water intrusion fragility modeling

The amount of rainwater that intrudes into a building through a panel depends on the amount of rainwater falling on the area above that panel and, of course, the area of the panel itself. Rainwater intrusion is also affected significantly by wind pressure on the roof, particularly near the opening. In general, the rate of rainwater intrusion through a roof-sheathing panel can be estimated as:

$$R = A_o \times v_{wt} \tag{5.9}$$

where A_o is the opening area of that roof-sheathing panel; and v_{wt} is the rate of rainwater intrusion through area A_o. It should be noted that another term could be added to account for the area of the openings in gaps around the panel and between adjacent panels due to construction tolerances, but since this was not specifically examined in this report, those terms have not been included in equation (5.9). In this report, the development focuses on the statistical formulation for calculation of the rainwater intrusion volume. For this reason, it is assumed that the rainwater intrusion velocity will be a linear combination of the rate of water falling onto the area above that panel and area of the panel itself, expressed simply as:

$$v_{wt} = (c_a s_a + c_u s_u) \tag{5.10}$$

where c_a and c_u are coefficients that must be determined experimentally, s_a is the rate of rainwater falling on the panel, and s_u is the rate of rainwater falling on the roof area above that panel (Figure 5.14). The effect of rainwater intrusion above the panel will be discussed in next section. The rate of rainwater falling on an area of the building is calculated based on local rain fall intensity as:

$$s_i = I \times \gamma_i \times A_i \tag{5.11}$$

where I is the rain fall intensity; A_i is the area under consideration and γ_i is local intensity factor for that area. The local intensity value is estimated based on the wind-driven rain model proposed by Choi (1993) or can be determined by experiment (Blocken and Carmeliet, 2002). For detailed information regarding the local intensity factor, the interested reader is referred to Choi (1993). Substituting equation (5.10) into equation (5.9), gives:

$$R = A_o(c_a s_a + c_u s_u) \tag{5.12}$$

From equation (5.13), an opening area limit, a_l, can be expressed as:

$$a_l = \frac{r}{c_a s_a + c_u s_u} \tag{5.13}$$

If the cross sectional area of the roof-sheathing opening, A, is greater than the limiting value or area limit, a_l, then the water intrusion into the structure exceeds the predetermined value r. Finally it can be seen that this can be expressed as the conditional probability, $Fr = P[(s - S) < 0|\mathbf{H} = \mathbf{h}] = P[(a_l - A) < 0|\mathbf{H} = \mathbf{h}]$.

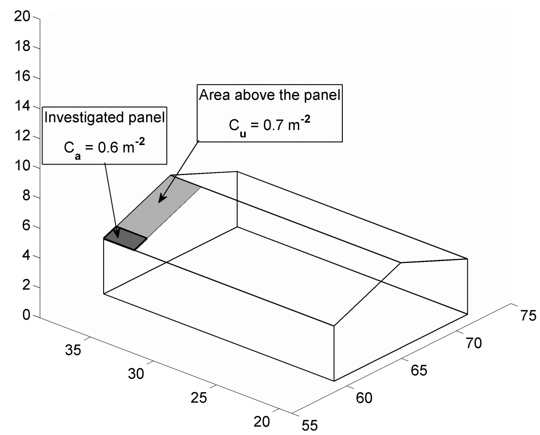

Figure 5.14: Rainfall Areas for illustrative example

Now the formulation turns to the structural modeling, in which one must determine the probability of exceedance for various size edge openings in the roof sheathing. This is possible with the new non-linear nail model developed by Dao and van de Lindt (2008). To do this, finite element analysis (not discussed in detail here for brevity) allows the identification of the uplift pressure that results in the area of the panel opening being equal to a_l. Using substantial nail test data, the statistics for the resistance of the roof-sheathing panel uplift behavior are determined. Then, together with the dead load statistics and wind pressure calculated from ASCE7-10 (2010), the probability of exceeding a particular volume of wind-driven rainwater can be computed (Dao and Van de Lindt, 2010).

The fragility curve is determined for each rainfall intensity value by rank ordering the data and fitting it to a lognormal distribution. Figure 5.15 shows a fragility surface for different rainfall intensities and basic wind speeds. From the fragility surface in Figure 5.15, one can take a slice parallel to any of the horizontal axes to hold either rainfall intensity or basic wind speed constant. A horizontal plane taken through the surface is a rainfall-basic wind speed contour in which the probability of exceeding the water intrusion limit is constant.

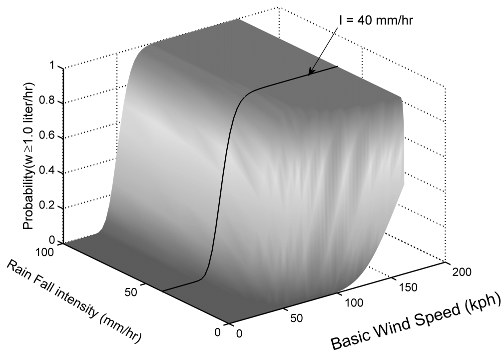

Figure 5.15: Fragility surface

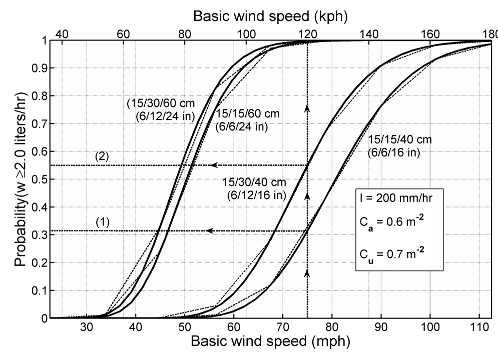

Figure 5.16: Fragility curves for different nail patterns

Figure 5.16 shows the fragility at a rainfall intensity of 200 mm/hr (8 in/hr) for four different nail patterns. The values of C_a and C_u were taken arbitrarily as 0.6 and 0.7, respectively. The numbers separated by slashes show the nail patterns and truss spacing, specifically the first number shows the roof sheathing panel edge nail spacing, the second number specifies the field nail spacing, and the last number specifies the truss spacing. In Figure 5.16, one can see that the probability of exceeding a water intrusion rate of 2.0 liters/hr at a basic wind speed of 120 kph (75 mph) is around 99% for nail patterns 15/15/60 cm (6/6/24 in) and 15/30/60 cm (6/12/24 in), 55% (dash line 2) for nail pattern 15/30/40 cm (6/12/16 in), and 32% (dash line 1) for nail pattern 15/15/40 cm (6/6/16 in). Now, consider a performance-based design requirement that is implicitly tied to damage from water intrusion, e.g. a performance requirement stating that the probability of exceeding 2.0 liters/hr during the hurricane is not greater than 50% (median) at a basic wind speed of 120 kph (75 mph) when rainfall intensity is (assumed to be) 200 mm/hr (8 in/hr). In this case, inspection of Figure 5.16 shows that only one nail pattern and truss spacing combination satisfies this performance requirement, namely the 15/15/40 cm (6/6/16 in) design.

5.5.3. Rain water intrusion during a hurricane

The rain water intrusion into a room of a residential structure during a hurricane can be estimated as:

$$R = \sum_{i=1}^{h} \sum_{j=1}^{n} R_{ij} \tag{5.14}$$

where h is number of hurricane hours n is number of roof sheathing panels above the room, R_{ij} is a random variable representing the amount of rain water intrusion through panel j during hurricane hour i.

Equation 5.14 can be used to calculate the amount of rainwater intrusion through a single panel, where s_a is the rate of rainwater falling on that roof panel and s_u is the rate of rainwater falling on the roof area above that roof-sheathing panel that runs down through this panel. In general, the amount of rainwater that runs through this panel is also affected by the rate of rainwater intrusion on all the panels above this panel. In order to account for this affect, one can write:

$$R_{ij} = A_o \left[c_a s_a + c_u \left(s_u - \sum_{k=1}^{m} R_{ik} \right) \right] \tag{5.15}$$

where R_{ik} is a random variable representing the amount of rainwater intrusion for the roof-sheathing panel above the panel of interest, panel j , during hurricane hour i, and m is the number of roof-sheathing panels above the panel being investigated.

MISSING AN EQUATION??

In equation 5.15 the statistical distribution of the random variable A_o is calculated based on results from non-linear finite element analysis (e.g. Dao and van de Lindt, 2008; Dao and van de Lindt, 2012) for which it is assumed that the roof sheathing panel has not yet failed, and therefore equation 5.15 is used to calculate the rate of rainwater intrusion for panel j for the case in which it has not yet failed. For the case where roof-sheathing panel j has failed prior to or during the hurricane hour i, the rate of water intrusion can be expressed as:

$$R_{ij} = s_a + s_u - \sum_{k=1}^{m} R_{ik} \tag{5.16}$$

Now, assuming that the roof covering always fails before the roof-sheathing panel since, in general, it has a lower wind resistance and this has been routinely observed (see e.g. van de Lindt et al, 2007). With this assumption, one can see that if the roof cover on a panel survives, then that roof-sheathing panel also survives; and there will be no rainwater intrusion through that panel. Therefore the probability of no rainwater intrusion is equal to the probability of roof cover survival. If the roof cover on a panel fails, there will be two possible cases that may result; the roof-sheathing panel survives and the roof-sheathing panel fails. If the roof sheathing panel survives, then rainwater will intrude through that panel edge opening. The probability of the amount of rainwater intrusion through that panel is equal to the probability of that amount of rainwater intrusion calculated by equation 5.15 multiplied by the probability the roof cover fails (recall that equation 5.15 already includes the probability of the panel survival). If the roof sheathing panel fails, then rainwater will go through the area left by that roof-sheathing panel. The probability of a specific amount of rainwater intrusion is calculated as the probability of that amount of rainwater intrusion estimated by equation 5.16 multiplied by the probability that the roof-cover fails multiplied by the probability that the roof-sheathing panel fails. Figure 5.17 summarizes the probabilistic procedure for the rate of rainwater intrusion through a panel with roof cover loss and roof-sheathing panel loss both taken into consideration.

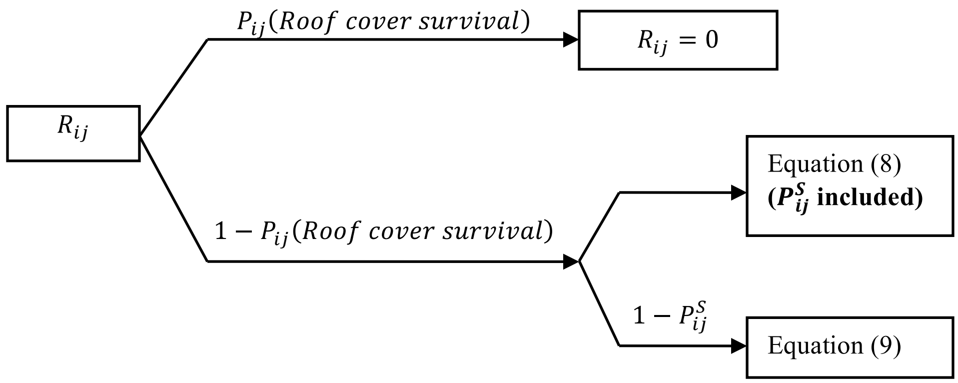

Figure 5.17: Probability of rainwater intrusion considering both roof cover loss and roof panel loss (exerpted from Dao and van de Lindt, 2012)

In Figure 5.17, P_{ij}^S is the probability of survival for panel *j* during the first *i* hurricane hours; and $P_{ij}(Roof\ cover\ survival)$ is the probability of roof cover survival for panel *j* during the first *i* hurricane hours (see Dao and van de Lindt, 2012 for more details). From Figure 5.17, one can compute the probability of rainwater intrusion through each roof-sheathing panel for each hurricane hour.

$P(R_{ij} = r_{ij}) = P_{ij}(Roof\ cover\ survival)$ For $r_{ij} = 0$ $P(R_{ij} = r_{ij})$ $= [1 - P_{ij}(Roof\ cover\ survival)][P(R_{ij} = r_{ij} \vert Panel\ survival)P_{ij}^S + P(R_{ij} = r_{ij} \vert Panel\ failure)(1 - P_{ij}^S)]$ For r_{ij}	(5.17)

where $P(R_{ij} = r_{ij} | Panel\ survival)$ is the probability of water intrusion given panel survival, (it should be noticed that the term $P(R_{ij} = r_{ij} | Panel\ survival)P_{ij}^S$ is calculated by equation 5.15); $P(R_{ij} = r_{ij} | Panel\ failure)$ is the probability of water intrusion given panel loss and estimated by equation 5.16 (see Dao and van de Lindt, 2012 for more details).

5.5.4. Future studies needed

In the method introduced above, the rainwater intrusion was calculated by combining a wind-driven rain model and nonlinear structural model. To have a better calibrated wind-driven rain model, experiments need to be conducted to measure the local intensity factors for the rain water falling on the building surface for different areas over different types of buildings (these would be similar to pressure coefficients in the ASCE 7 wind loading provisions). Further experimental and numerical studies on wind-driven rain will enable the estimation of amount of rainwater falling on building surface under different wind velocities and rain fall intensities.

A measure of the water intrusion through the building surface also needs to be tested to determine several coefficients that were assumed in the method. A thorough study should focus more on the effect of wind pressure on the rate of water intrusion given different sheathing edge. enings.

Chapter 6. Guidance for Designers and Practitioners

Authors: Cope, Jain, Williams, Kiesling

6.1. Overview

The purpose of this chapter is to provide designers and practitioners with a source for research and measurements for the application of wind-driven rain loads to building design. In order to understand the wind-driven rain behavior as it applies to building performance, a basic understanding of the climatology behind it must first be developed. This begins with an assessment of conditions, the sources of data, and a standardization of data sets used to analyze driving rain conditions. The two most commonly used semi-empirical models based on experimental results and theories are presented for use in determining wind-driven rain loads. Standard testing methods for water ingress of wind-driven rain for various building components are given. Full scale experiments have been conducted on entire buildings, and on individual components to evaluate their water penetration resistance. These full-scale experiments vary widely in their methods of simulating pressure, velocity, and precipitation in obtaining results.

6.2. Modeling of Spatial Rain Deposition on Buildings

6.2.1. Climatological Assessment of Wind-Driven Rain Conditions

6.2.1.1. Parameters

In order to perform climatological assessments at specific locations of interest, certain parameters must be known or readily available. The determination of wind-driven rain intensity is easily calculated, given the mean wind speed, horizontal rainfall intensity, and raindrop terminal velocity are known. Common data sources used for rainfall intensity assessments are further described in the following section, with the addition of event specific reconstruction of wind driven rain conditions.

6.2.1.2. Data Sources

Meteorological data is available via data sources such as the National Climatic Data Center (US), NWS HYDRO-35 (1977), research conducted by Underwood and Meentemeyer (1998) and research conducted by Applied Research Associates for the State of Florida's Residential Construction Mitigation Program (RCMP). These data sources provide various outlets of reference in regards to climatological data, available for use in determination of wind-driven rain intensities throughout the United States.

The National Climatic Data Center (NCDC), a division of the National Oceanic and Atmospheric Administration (NOAA), headquarters the world's largest archive of climatological data, providing data to users at locations across the entire United States and in select locations worldwide. Climatological data services provided range from land-based station data, satellite data, radar data, model data, weather balloon data, and marine/ocean data, to paleoclimate data. In terms of climatological assessments of wind-driven rain, Doppler radar data is typically utilized. A download of the NCDC Weather and Climate Toolkit provides access to WSR-88D (NEXRAD) datasets for a user-specified time frame. These datasets provide the three meteorological base data values: reflectivity, mean radial velocity, and spectrum width and are known as Level II data. From Level II data values, Level III values (i.e. base reflectivity, base velocity, storm relative velocity, base spectrum width, and composite reflectivity, to name a few) are generated.

The NOAA's Weather Climate Toolkit is easily accessible via internet installation (www.ncdc.noaa.gov/oa/wct/install.php). Through the NCDC NEXRAD Data Inventory, data for specific time frames is "ordered." With each order, a NCDC HAS Job Number is assigned and used within the Weather and Climate toolkit application, as seen in Figure 6.1. Ordering data inventory is accessible through: http://www.ncdc.noaa.gov/nexradinv/, where users select the National Doppler Radar nearest the location of interest. The NOAA NCDC Weather and Climate Toolkit has the capability of exporting climatological data in various output formats (i.e. shapefile, well-known text, ESRI, GeoTIFF).

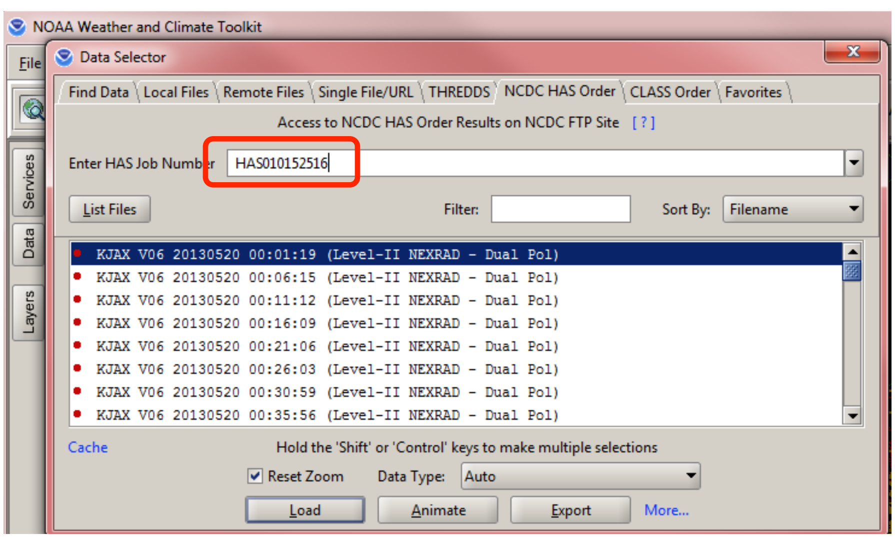

Figure 6.1. Screenshot of NOAA Weather and Climate Toolkit

The National Weather Service (NWS), also a division within the National Oceanic and Atmospheric Administration (NOAA), provides weather, water and climate data, forecasts and warnings. The NWS HYDRO-35, published in 1977, presents precipitation-frequency values for 37 states, from Texas to North Dakota and eastward. These values were measured for durations of 5, 15 and 60 minutes for return periods of 2 and 100 years. Within HYDRO-35, equations are presented as computations to derive 10- and 30- minute values. These values were measured with recording rain gages at approximately 200 stations, and annual 1-hr events were recorded at approximately 1900 stations. These precipitation frequencies were plotted on a map of the 37 states observed as contour lines. Linear interpolation between contour lines provides precipitation frequencies for locations that do not have direct measurements. Figure 6.2 displays the precipitation frequencies for a 2-yr 60 minute precipitation event.

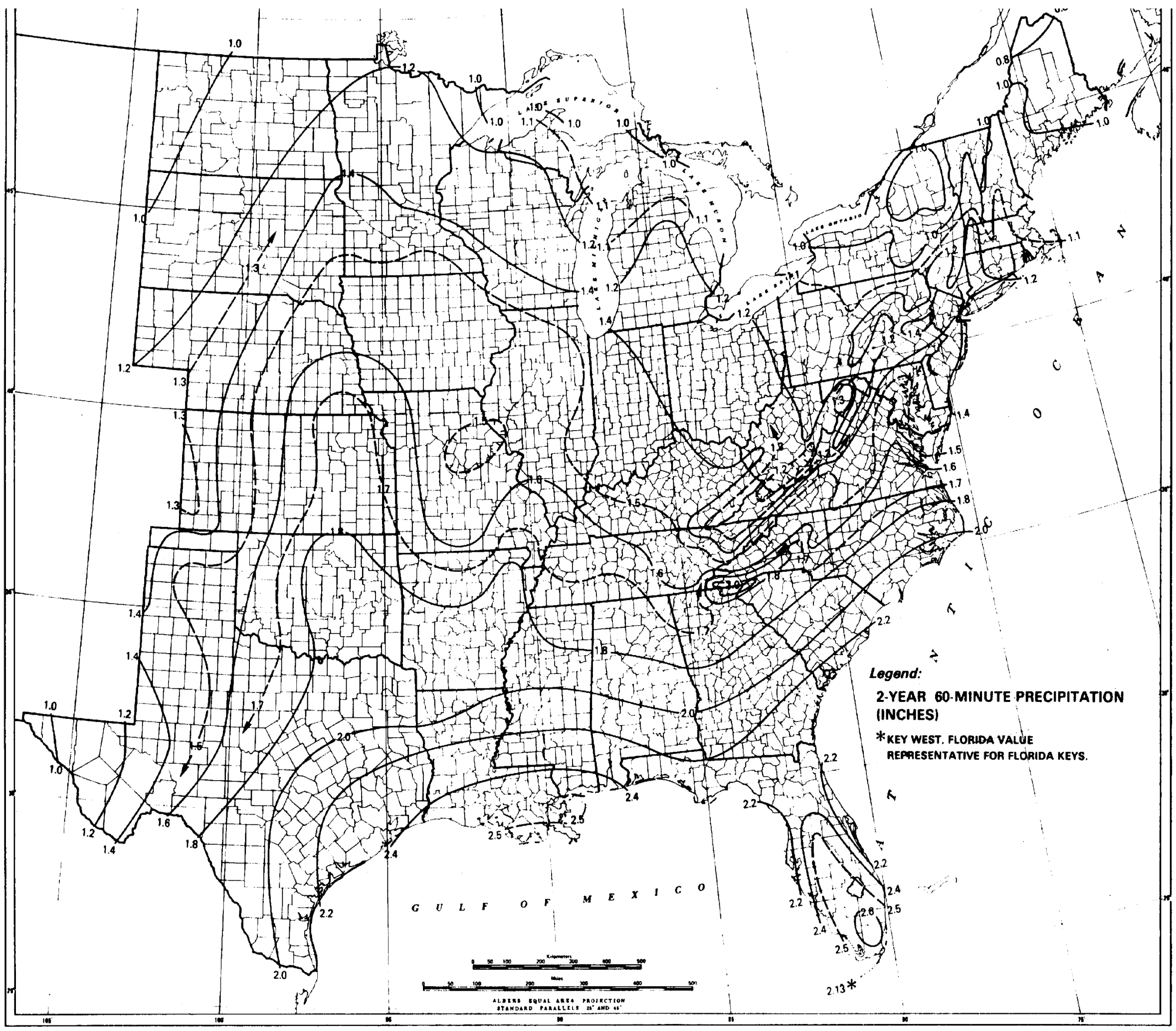

Figure 4.--2-year 60-min precipitation (inches)--adjusted to partial duration series.

Figure 6.2. NWS HYDRO-35 (1997) 2-year 60-minute precipitation.

In 1998, Underwood and Meentemeyer introduced climatology of wind-driven rain for the contiguous US for the period 1971 to 1995. Prior to this introduction, wind-driven rain assessments of this sort had not been performed. By this time, raindrop size distribution had been introduced by A.C. Best (1950) and the effects of wind-driven rain on buildings, soil and crops had been documented. Before the work by Underwood and Meentemeyer was completed in 1998, only one study had presented a map of WDR across the United States (Grimm 1982), based solely on average annual rainfall rate estimates and wind speed at 120 locations across the country. Studies by Underwood and Meentemeyer introduced climatologies for WDR event duration, WDR frequency of occurrence and total WDR for a year, across the contiguous United States.

Climatological maps produced from the Underwood and Meentemeyer study provide a base framework for wind-driven rain assessment in the United States. These estimates, frequencies, and total wind-driven rain values vary from year to year, as meteorology is unpredictable; however, even with variability, a base knowledge of the climatology is able to be formed.

As a result of research conducted by Applied Research Associates, as proposed by the Residential Construction Mitigation Program, wind-driven rain maps for the state of Florida were created. These contour maps, for specific return periods, outline the following WDR parameters: rain score, effective storm duration and effective wind speed, all necessary to determine the wind-driven rain hazard. Utilizing a hurricane hazard model, the combination of a wind model and updated rainfall model generated rain scores for the state of Florida. Rain scores, for this particular type of analyses, are defined as the "measure of the wind driven rain load," which is further defined as the "integral of the wind driven rain intensity multiplied by an indicator of the pressure difference across a window or wall."

Contour lines for the rain score map were computed as given by Equation #:

$$RS = \int_0^T \left(U^2(t) * R_{wdr}(t)\right) dt \qquad (6.1)$$

where $U(t)$ is the mean wind speed and $R_{wdr}(t)$ is the wind-driven rain intensity. Figure # illustrates the rain score contours for the state of Florida, as determined using hurricane hazard modeling, wind models and an updated rainfall model.

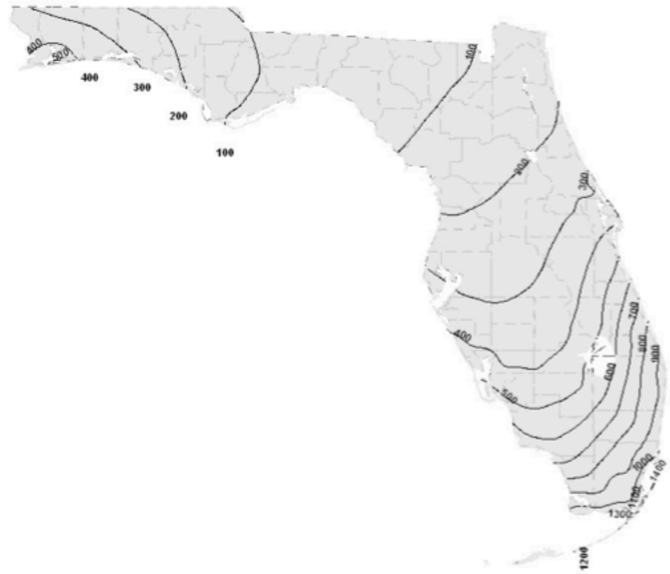

Figure 6.3. 50-Year Rain Score Map (provided by ARA)

While these wind-driven rain maps provide useful information of wind-driven rain hazard, the lack of maps for other coastal regions (i.e. East coast, Texas) hinders use for locations other than the state of Florida. A similar approach used to generate these maps for the state of Florida could be applied for other areas of interest.

6.2.2. Standardization of Data Sets

Prior research regarding the standardization of data sets, performed by Blocken and Carmeliet (2008), outlines the variation of wind-driven rain calculations on buildings with regard to time resolution. Because wind-driven rain is dependent upon the rainfall intensity and wind velocity, it is imperative to use a resolution that is as accurate as possible, with little estimation error. Raw data measurements, once collected are averaged over typical averaging intervals, producing the dataset used for analysis (Blocken and Carmeliet 2008). However, by averaging over particular intervals both rainfall intensity and wind velocity, loss of peak estimates occurs, producing underestimates and overestimates that significantly alter the data. An additional source of error is the violation of wind velocity and rainfall intensity co-occurrence (Blocken and Carmeliet 2008).

Blocken and Carmeliet (2008) provides guidelines for determining minimum time resolution of meteorological data, upon study of the four most important parameters influencing data averaging error: (1) averaging technique, (2) averaging interval, (3) building geometry/position and (4) type of rain event. Upon analysis, guidelines were presented for use when determining the time resolution needed for accurate WDR calculations. Dependent on each parameter's influence, a recommendation of 10 minutes is presented as the minimum required time resolution. This recommendation can vary from 10 minutes to 1 day, relative to the parameters.

Two averaging techniques presented provided a clear indication that the most accurate WDR measurements were calculated using a weighted average of raw 10 minute data rather than the traditional arithmetic average.

6.2.3. Event-Specific Reconstruction of Wind-Driven Rain Conditions

Recreation of specific weather events in a laboratory setting provides the capability to test the resistance of various building components to realistic rainfall characteristics during intense weather conditions, such as tropical cyclones.

Data sources, mentioned in the previous sections, provide base rainfall characteristics needed for reconstruction of specific weather events; however, reconstruction of raindrop size distribution from these sources is not possible. The NCDC Weather and Climate Toolkit provides reflectivity estimates, as well as the generation of rainfall intensities, but it does not have the capability of directly measuring an event-specific raindrop size distribution. Thus, in order to reconstruct weather events, raindrop size distribution must be determined using derivations incorporating the rainfall parameters accessed from rainfall data sources.

Additionally, event-specific reconstruction may be accomplished from direct observations recorded during storm deployments. The University of Florida, along with other research universities in the United States, deploy during tropical cyclones in order to further characterize these natural hazards. Measurement devices, known as disdrometers, record the raindrop count at various frequencies, the key parameter in determining raindrop size distribution from these measurement devices. However, storm deployments are neither feasible nor safe for all to participate in. The data collected during storm deployments most often is used directly in the laboratory by those collecting it.

6.2.4. Semi-empirical models

Measurements are time-consuming, expensive and often impractical. Recent research has revealed that WDR measurements are also very prone to error (Högberg et al. 1999, Blocken and Carmeliet 2005, 2006a). In addition, measurements made on the facades of a particular building at a particular site, have limited applicability to other facades of other buildings at other sites. This awareness has driven researchers to develop calculation models, which have been progressively improved throughout the years. Today, the models that are most advanced and most frequently used are the semi-empirical model in the ISO Standard for WDR assessment (ISO 2009) (ISO model), the semi-empirical model by Straube (1998) and Straube and Burnett (2000) (SB model) and the CFD model by Choi (1991, 1993, 1994a) extended into the time domain by Blocken and Carmeliet (2002, 2007). A concise overview of the two semi-empirical models is provided in this chapter. A more detailed overview and a comparison of these models can be found in Blocken and Carmeliet (2010) and Blocken et al. (2010, 2011).

6.2.4.1.1 Semi-empirical model in the ISO Standard

The main method in the ISO Standard (ISO) provides a procedure to calculate two quantities: (1) the annual average index (as a measure for average WDR exposure) and (2) the spell index (as a measure for maximum or peak WDR exposure). The procedure consists of two steps. First, the airfield index is calculated, which refers to WDR in free-field conditions, i.e. without buildings present, and related to a smooth grass-covered terrain (airfield). Next, this airfield index is converted to a wall index by correction factors to take into account the differences between free-field WDR (as in Eq. 2) and WDR impinging on the building. The correction factors are the roughness coefficient, the topography coefficient, the obstruction factor and the wall factor. Note that the word "index" has been inherited from earlier WDR research; it is used in the ISO Standard to refer to WDR amounts, expressed in L/m² or mm. The airfield hourly index is defined as *"the quantity of driving rain that would occur on a vertical wall of given orientation per square meter of wall during 1 h at a height at 10 m above ground level in the middle of an airfield, at the geographical location of the wall"* (ISO 2009). The airfield annual index is the airfield index for a given wall orientation totaled over one year. The calculation is performed with at least 10 (and preferably 20 or 30) years of hourly values of wind speed, wind direction and horizontal rainfall intensity from the nearest meteorological station:

$$I_A = \frac{2}{9} \frac{\sum U_{10} \cdot R_h^{8/9} \cdot \cos\theta}{N} \tag{6.2}$$

where the airfield annual index I_A is expressed in L/m²a (a = annum), U_{10} is the reference wind speed (unobstructed streamwise wind speed at 10 m height) and N is the number of years of available data. The summation is taken over all hours when cosq is positive, i.e. the hours when the wall is windward.

The airfield spell index is defined as the "*airfield index for a given wall orientation totaled over the worst spell likely to occur in any three-year period*". A spell is defined as a period during which WDR occurs, and that is preceded and followed by at least 96 hours with airfield hourly index $((2/9)U_{10}R_h^{8/9}\cos\Theta)$ smaller than or equal to zero. Using at least 10 (and preferably 20 or 30) years of hourly values of wind speed, wind direction and horizontal rainfall intensity, separate airfield indices are calculated for the given wall orientation and for each spell of WDR:

$$I_S' = \frac{2}{9} \sum U_{10} \cdot R_h^{8/9} \cdot \cos\theta \tag{6.3}$$

where I_S' is expressed in L/m². The summation is again taken over all hours in the spell when $\cos\theta$ is positive. The airfield spell index I_S is then obtained as the maximum value of I_S' likely to occur once every three years.

The wall annual index (I_{WA}) and the wall spell index (I_{WS}) are calculated by multiplying the airfield indices with four correction factors: the roughness coefficient C_R, the topography coefficient C_T, the obstruction factor O and the wall factor W:

$$I_{WA} = I_A \cdot C_R \cdot C_T \cdot O \cdot W \; ; \qquad I_{WS} = I_S \cdot C_R \cdot C_T \cdot O \cdot W \tag{6.4}$$

The roughness coefficient CR takes into account the change of mean wind speed at the site due to the height above the ground and the upstream roughness of the terrain. It is given by:

$$C_R(z) = K_R \ln\left(\frac{z}{z_0}\right) \qquad \text{for } z \geq z_{min} \tag{6.5}$$

$$C_R(z) = C_R(z_{min}) \qquad \text{for } z < z_{min} \tag{6.6}$$

where z is the height above ground, K_R the terrain factor, z_0 the aerodynamic roughness length and z_{min} a minimum height. Values of K_R, z_0 and z_{min} as a function of the terrain category are given in Table 6.1. The Draft notes that if a change of upstream roughness occurs within 1 km, the smoothest upstream terrain category must be used. Note that the smoothest terrain category provides the largest C_R value.

The topography coefficient C_T takes into account the increase of mean wind speed over isolated hills and escarpments. It is applied when the wind approaches the slope of the hill or the escarpment and when the building is located at "*more than half way up the slope of a hill" or "within 1.5 times the height of the cliff from the base of a cliff*". It ranges between 1.0 for upstream slopes with less than 5% inclination to a peak value of 1.6 for buildings situated at the crest of steep cliffs or escarpments.

The obstruction factor, O, takes into account the shelter of the wall by the nearest obstacle, which is at least as high as the wall, along the line of sight from the wall. The line of sight is defined as the "*horizontal view away from the wall, over a sector spanning about 25° either side of the normal to the wall*". The obstruction factor is given in Table 6.2. The Standard notes that the obstruction factor may vary significantly at different points along a long wall, and that, if the layout of the built environment is likely to funnel wind towards the wall, the obstruction factor should be taken equal to one, irrespective of the presence of obstructions.

Finally, the wall factor W is defined as the "*ratio of the quantity of water hitting a wall to the quantity passing through an equivalent unobstructed space*", i.e. the ratio of WDR on the building to free-field WDR. Note that this is not the "airfield" free WDR, but the free-field WDR at the building location, after taking into account the correction factors C_R, C_T and O. The wall factor tries to take into account the type of the wall (height, roof overhang) and the variation of

WDR across the surface of the wall. The wall factors made available in the ISO Standard are shown in Fig. 6.1.

Table 6.1. Parameters in the ISO Standard roughness coefficient (ISO 2009)

Terrain category	Description	KR	z0	zmin
I	Rough open sea; lake shore with at least 5 km open water upwind and smooth flat country without obstacles	0.17	0.01	2
II	Farm land with boundary hedges, occasional small farm structures, houses or trees	0.19	0.05	4
III	Suburban or industrial areas and permanent forests	0.22	0.3	8
IV	Urban areas in which at least 15% of the surface is covered with buildings of average height exceeding 15 m	0.24	1	16

Table 6.2. ISO Standard obstruction factor as a function of the distance of the obstruction from the facade (ISO 2009)

Distance of obstruction from facade (m)	Obstruction factor O
4 - 8	0.2
8 - 15	0.3
15 - 25	0.4
25 - 40	0.5
40 - 60	0.6
60 - 80	0.7
80 - 100	0.8
100 - 120	0.9
over 120	1.0

Description of wall	Average value	Distribution
Two storey gable	0,4	0,5 0,4 0,3 0,3 0,3 0,2
Three storey gable	0,3	0,5 0,4 0,3 0,3 0,3 0,3 0,3 0,3 0,2
Multi storey building with flat roof (pitch < 20°)	0,2 for e.g. ten storey, but higher intensity at top	0,5 for top 2,5 m 0,2 for remainder
Two storey eaves wall	0,3	Pitched roof (≥ 20°) typical overhang 350 mm 0,3 0,3 0,3
Three storey eaves wall	0,4	Pitched roof typical overhang 350 mm 0,4 0,4 0,4
Two storey building with flat roof (pitch < 20°)	0,4	0,5 0,4 0,2

Fig. 6.4. Wall factors (W) in the 2009 ISO Standard that are the same as those in the European Standard Draft (© CEN 2006, reproduced with permission).

6.2.4.1.2. Semi-empirical model by Straube and Burnett

The model by Straube (1998) and Straube and Burnett (2000) is based on Eq. 6.7 where the "Driving Rain Function" DRF is introduced as the inverse of the raindrop terminal velocity of fall:

$$R_{wdr} = \frac{1}{V_t} \cdot U \cdot R_h = DRF \cdot U \cdot R_h \qquad (6.7)$$

Straube and Burnett recommend calculating the DRF from the equation by Dingle and Lee (1972) for the terminal velocity:

$$V_t(d) = -0.166033 + 4.91844\, d - 0.888016\, d^2 + 0.054888\, d^3 \leq 9.20 \text{ m/s} \tag{6.8}$$

where d is the raindrop diameter. Concerning the choice of d, they suggest the median diameter from the raindrop spectrum by Best (1950):

$$F(d) = 1 - \exp\left(-\left(\frac{d}{a}\right)^n\right) , \quad a = A R_h^{\,p} \tag{6.9}$$

where F(d) is the fraction of liquid water in the air with raindrops of diameter less than d, and A, n, p are parameters, the experimentally determined averages of which are 1.30, 2.25 and 0.232, respectively. From Eq. 6.9, the following equation for the median raindrop diameter can be obtained:

$$\bar{d} = 1.105\, R_h^{\,0.232} \tag{6.10}$$

Eqs. 6.7-6.9 indicate that the DRF or free-field WDR coefficient suggested by Straube and Burnett is a function of raindrop terminal velocity of fall, raindrop-size distribution and horizontal rainfall intensity R_h. This is based on the work by Choi (1994b), who demonstrated analytically that the DRF is a function of both the raindrop-size distribution and the raindrop terminal velocity of fall, both of which are linked to Rh. Straube and Burnett found that the DRF ranges from 0.20 to 0.25 s/m for average conditions but that it varies considerably for different rainfall intensities and rain storm types, from more than 0.5 s/m for drizzle to 0.1 s/m for intense cloudbursts.

The model by Straube and Burnett for WDR on building facades is given by:

$$R_{wdr} = DRF \cdot RAF \,.\, U(z) \cdot R_h \cdot \cos\theta \tag{6.11}$$

where RAF, the “Rain Admittance Factor”, is introduced to convert the free-field WDR intensity to the WDR intensity on the building facade. Based on their own WDR measurements (both free-field WDR and WDR on the walls of a test building) and on a literature review, Straube and Burnett provided values of the RAF in graphical form for three types of building geometries. They claimed that these contours and values are relatively building-scale independent. The increase of WDR intensity with height is partly taken into account by the presence of the power law function $U(z) = U_{10}(z/10)^a$ in Eq. 6.11, and partly by the RAF values themselves.

6.2.4.2. Computational Fluid Dynamics

Using computational fluid dynamics (CFD), solving the Navier-Stokes equation using the k-e model, the wind flow pattern around a building can be obtained Choi (1993). The results of the CFD calculations are then used to solve the equations of motion for raindrop trajectories over time (Lagrangian particle tracking), enabling the determination of the WDR impinging on the building façade. From the results the specific catch ratio, dependent upon the raindrop diameter, and the catch ratio which incorporates the entire range of drop diameter, can be determined. This model by Choi (1993) was verified by field measurements for accuracy, and used as a basis of comparison for the ISO and SB models, the two most frequently used semi-empirical models Blocken (2010). The CFD model provides an accurate representation of the wind-blocking effect, which varies with building geometry, and is not fully accounted for by the semi-empirical models.

6.2.4.3. Boundary Layer Wind Tunnel Modeling

Wind tunnel simulation of wind-driven rain involves major challenges. It requires simultaneous scaling of wind and rain. Inherent in the simulation of the flow field, it is difficult to maintain all the similarity requirements of non-dimensional parameters between model (wind tunnel) and prototype (full-scale). In order to generate these similarity requirements, the scaling based on dimensionless parameters such as Reynolds number (Re) and Froude number (Fe), must be applied to reproduce the natural characteristics of the full-scale free-field wind-driven rain flow.

6.2.4.4. Full-Scale Measurements

Presented in more detail in the State of the Art Report on Research, full-scale measurements of wind-driven rain are obtained through measurements in the field, utilizing wind-driven rain gauges as well as through other technological devices (i.e. disdrometers). Measurement of wind-driven rain is tabulated through the use of wind-driven rain gauges; however, no standard exists on the type of wind-driven rain gauge utilized (Blocken and Carmeliet 2004). Additionally, disdrometers offer the ability to measure drop size distribution of wind-driven rain. However, measurement error may present itself through evaporation of adhesion water, evaporation of water present in the reservoir, splashing of drops, condensation on the collection area and potential wind errors (Blocken and Carmeliet 2004). Many field experiments regarding measurement of wind-driven rain have been performed by various researchers. The reader is directed to a review of wind-driven rain assembled by Blocken and Carmeliet (2004) for additional information.
Add

6.3. Standardized Testing Procedures

Authors: Eric Haefli and Carlos Lopez

In strong storms, building products are subjected to extreme wind loads and wind-driven rain. Standardized testing procedures are used to evaluate the performance of these products particularly because the methods are simple and repeatable. In the case of water penetration resistance, procedures are available for the evaluation of fenestration, masonry, and other building products. Many municipalities mandate that these products be evaluated by accredited laboratories using these methods; however, product manufacturers use them in research and development and engineers use these them in the field to determine if products meet their design requirements, identify vulnerabilities, and as diagnostic tool to identify and isolate problems.

In general, standardized testing procedures can be characterized by their respective pressure loading sequence. In this document they will be categorized into uniform static, cyclic static and cyclic, and pseudo-dynamic air pressure difference. Table 6.3 lists standardized testing procedures and their product applicability. Further information regarding a particular procedure may be directed to its respective standard.

Table 6.3 Summary of Common Existing Testing Protocols

Test Name	Type of Load	Specified Load	Specified Number of Cycles	Objective	Product Applicability
ASTM E331	Static	137 Pa (2.86 psf)	N/A	Water penetration	Exterior windows, skylights, doors, and curtain walls
ASTM E1105 Procedure A	Static	Unspecified	N/A	Field determination of water penetration	Exterior windows, skylights, doors, and curtain walls
TAS 202	Static	75%, 150%, and 15% of DP	N/A	Structural, water penetration, air infiltration, forced entry	Any external component which helps maintain the integrity of the building envelope
ASTM E1646	Static	137 Pa (2.86 psf) for roof slopes less than or equal to 30° 300 Pa (6.24 psf) for roof slopes greater than 30° Test pressures	N/A	Water penetration	Exterior metal roof panel systems

		are not to exceed 575 Pa (12.0 psf)			
ASTM E1089	Static	480 Pa (10.0 psf)	N/A	Water penetration	Flat plate solar collectors
ASTM E514	Static	500 Pa (10.2 psf)	N/A	Water penetration	Unit masonry
ASTM C1601	Static	Pressure determined using Bernoulli equation and desired test wind speed up to 33.5 m/s (75.0 mph)	N/A	Water penetration	Masonry wall surfaces
ASTM D6904	Static	1245.4 Pa (26.0 psf)	N/A	Water penetration	Coatings on masonry block
ASTM E1105 Procedure B	Cyclic Static	Unspecified	Minimum of 3	Field determination of water penetration	Exterior windows, skylights, doors, and curtain walls
ASTM E547	Cyclic Static	137 Pa (2.86 psf)	Unspecified	Water penetration	Exterior windows, skylights, doors, and curtain walls
ASTM E2268	Cyclic	206.0 Pa (2.5 psf), 137.0 Pa (2.86 psf), 69.0 Pa 1.4 psf	300	Water penetration	Exterior windows, skylights, and doors
AAMA 520	Cyclic	See table 6.4	300 per level see table 6.4	Water penetration	Windows, doors and unit skylights
AAMA 501.1	Pseudo-Dynamic	300.0 Pa (6.2 psf), 380.0 Pa (8.0 psf), 480.0	One 15 min cycle at a time	Water penetration	Windows, curtain walls and doors

		Pa (10.0 psf), 580.0 Pa (12.0 psf), and 720.0 Pa (15.0 psf)			
TAS 100	Pseudo-Dynamic	15.6 m/s (35.0 mph), 0.0 m/s (0.0 mph), 31.3 m/s (70.0 mph), 40.2 m/s (90.0 mph), 0.0 m/s (0.0 mph), 49.2 m/s (110.0 mph), 0.0 m/s (0.0 mph)	1	Water penetration	All discontinuous roof systems, consisting of a prepared roof covering and underlayment
TAS 100(A)	Pseudo-Dynamic	15.6 m/s (35.0 mph), 0.0 m/s (0.0 mph), 31.3 m/s (70.0 mph), 40.2 m/s (90.0 mph), 0.0 m/s (0.0 mph), 49.2 m/s (110.0 mph), 0.0 m/s (0.0 mph)	1	Water penetration	Soffit ventilation and a continuous or intermittent ridge area ventilation system (i.e., ridge vents, static vents, turbines or powered vents)

6.3.1 Uniform Static Air Pressure Difference

Uniform static air pressure tests are widely used in the product approval process (e.g., ASTM E331) and in diagnostic assessment of leakage paths in existing structures (e.g., Procedure A of ASTM E1105). The specimen is surrounded by a pressure chamber which provides a constant pressure differential between each side of the specimen for a prescribed amount of time. A constant water spray is applied to the exterior surface of the specimen through the duration of the test and the location of leaks is recorded along with other pertinent test data.

ASTM E331 is the most commonly used test method in the evaluation of fenestration products and also serves as the basis for uniform static air pressure tests of other building products (e.g., ASTM E1646 for exterior metal roof panel systems, ASTM E1089 for flat plate solar collectors). ASTM E331 is performed in the laboratory and prescribes that the "test-pressure difference or differences at which water penetration is to be determined, unless otherwise specified, shall be 137.0 Pa (2.86 psf)" for a period of 15 minutes (see figure 6.2). This test was later modified in ASTM E1105 Procedure A to evaluate performance of fenestration in the field. ASTM E1105 Procedure A maintains the load duration of 15 minutes; however, the load is unspecified and left to the discretion of the party instructing the test. Further, all ASTM procedures used to evaluate fenestration define water penetration as "penetration of water beyond a plane parallel to the glazing (the vertical plane) intersecting the innermost projection of the test specimen, not including interior trim and hardware, under the specified conditions of air pressure difference across the specimen."

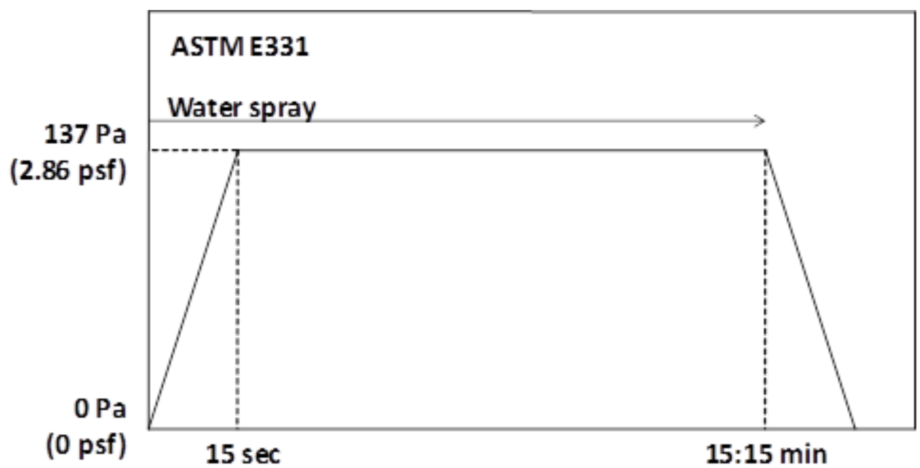

Figure 6.5. ASTM E331 Pressure Loading History

Testing Application Standard (TAS) 202 is used to evaluate the structural and water penetration performance of fenestration products. It closely resembles ASTM E331; however, it imposes different passing criteria. TAS 202 structurally tests a window to 150% of the rated design pressure, while recording the maximum and permanent deflections during testing (see figure 6.3). To meet water infiltration requirements, fenestration must not exhibit any water intrusion when 15% of the design pressure is applied with a constant water spray (see Section 5.2.6 of TAS 202).

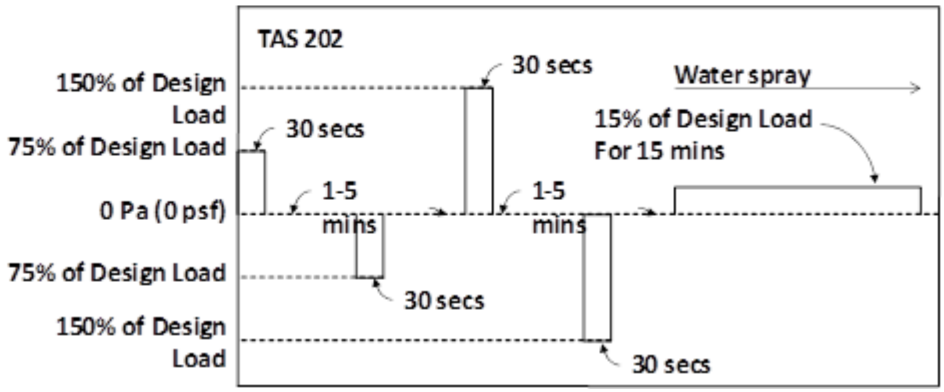

Figure 6.6. TAS 202 Pressure Loading History

Other uniform static air pressure tests include those used in the evaluation of the performance of masonry and masonry coatings (ASTM E514, ASTM C1601, and ASTM D6904). These tests are performed in a similar manner as those presented above; however, the specified loads are greater and in the case of ASTM C1601 the test pressure is directly correlated to wind speed using the Bernoulli equation and desired test speed up to 33.5 m/s (75 mph).

6.3.2 Cyclic Static and Cyclic Air Pressure Difference

Cyclic static and cyclic air pressure tests are also used to evaluate water penetration resistance of building components. Cyclic static test are similar to uniform static air pressure tests but differ in that the specimen is subjected to static pressures multiple times. Cyclic air pressure tests prescribe different test pressures which must be achieved in rapid pulses for a specified number of cycles. The concept is that cyclic loading will more closely resemble in field conditions and may display leaks that are otherwise not observed. Varieties of these tests include those performed in the laboratory and in the field (e.g. Procedure B of ASTM E1105, ASTM E547, ASTM E2268, JIS A 1517, and AS/NZS 4284:1995).

The two most common static cyclic pressure tests used in the evaluation of fenestration products are ASTM E1105 Procedure B, and ASTM E547. Both examine the performance of installed fenestration, however; ASTM E1105 is strictly a field test. Pressure loading in ASTM E1105 Procedure B is similar to its counterpart, ASTM E1105 Procedure A, in that the load is unspecified and left to the discretion of the party instructing the test. ASTM E547 is a variant of ASTM E331; however, the pressure is cycled from zero for a specified amount of time and cycles (see figure 6.5).

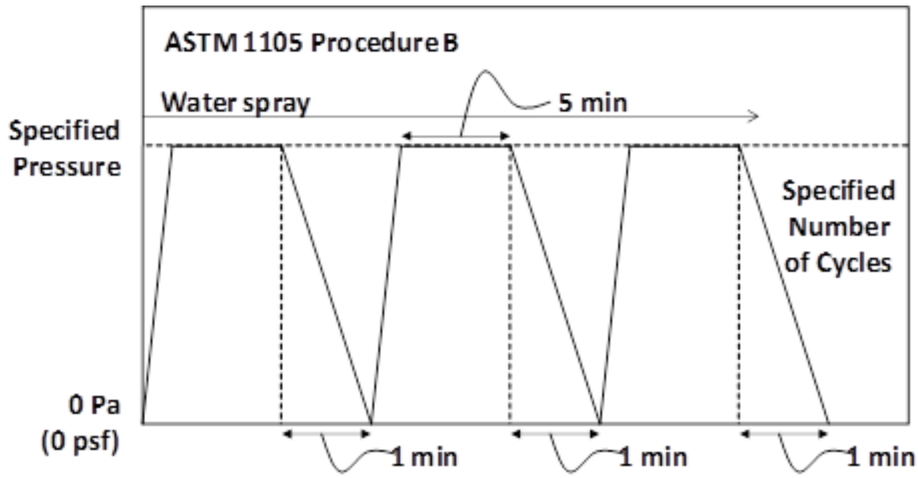

Figure 6.7. ASTM 1105 Procedure B Pressure Loading History

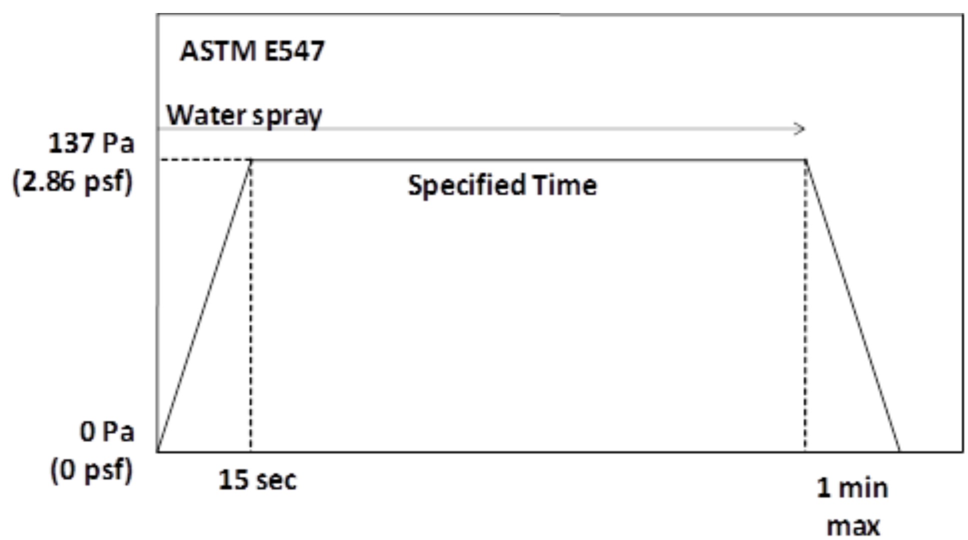

Figure 6.8. ASTM E547 Pressure Loading History

ASTM E2268 is a cyclic pressure test defined by rapid pulsed air pressure difference. ASTM E2268 has the same loading function as Japanese Industrial Standard JIS A 1517 (a modulation limited to ± 50% of the median pressure with pulse lengths of 2 seconds), but it states that the "median test-pressure difference or differences at which water penetration is to be determined, unless otherwise specified, shall be 137.0 Pa (2.86 psf)" as is prescribed in ASTM E331 (see figure 6.5).

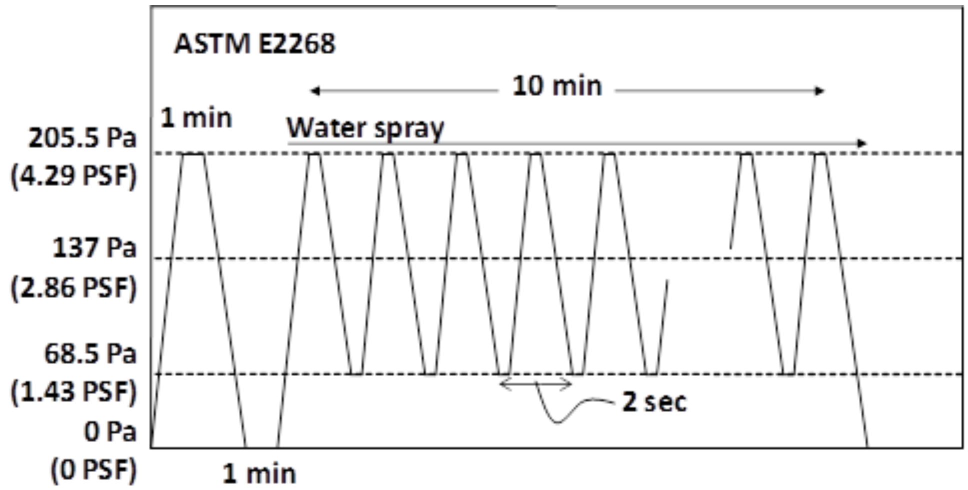

Figure 6.9. ASTM E2268 Pressure Loading History

6.3.3 Limitations of Uniform Static Air Pressure, Cyclic Static, and Cyclic Air Pressure Tests in Evaluating Fenestration Performance

In examining uniform static, cyclic static, and cyclic air pressure tests, concerns have been voiced by some in the industry. The following discusses these salient points.

- Building products and installation methods vary due to structural design pressure requirements and all have the potential to perform differently. Default minimums (e.g., 137.0 Pa, 2.86 psf, for fenestration and 500 Pa, 10.2 psf for masonry), rather than a percentage of the design pressures may not suit the requirements necessary for different areas of the building or all geographic areas. This issue becomes apparent in a high velocity wind zones where design pressures can be relatively high. An example is residential windows sold in coastal areas, whose lowest common pressure rating is approximately 1440.0 Pa (30.0 psf). Testing these products to 137.0 Pa (2.86 psf) would test water penetration resistance to approximately 10% of the design pressure and less for higher rated windows. Similarly, some masonry and exterior metal roof panel systems standards test to 500 Pa (10.2 psf) and 575 Pa (12.0 psf), respectively. These pressures could be such a small percentage of the design pressures that they could routinely be exposed to the test conditions.

- Test results are based on pass/fail criteria, there is no stipulation on how to test for, quantify, or record any water infiltration rates. In some cases water infiltration can occur but is not recorded until certain criteria is met. Reporting infiltration rates and/or minimum pressures at which the products exhibit any water infiltration may be more appropriate for designers. Similarly, the lack of distinction in performance from product to product may play a role in the extent of insurable damage. Results reported for minimum performance standards do not provide such information.

- There are no strategies or stipulations provided for different wind-driven rain exposure conditions (i.e., climate zones). This raises the question if water penetration resistance should be related directly to wind exposure zones.

- Age effects are not considered. UV, ozone, and environmental exposures, over time, adversely affect the water penetration resistance of fenestration components such as weather-stripping and sealants (Katsaros et al. 2007). Aging of the finished wall system may also yield new infiltration paths. The benefits of testing artificially aged assemblies merits further study (Katsaros et al. 2007, Lindgren 1984, Gjelsvik 1983, Fazio et al. 1997).

- These procedures typically test specimens in isolation. Testing of products as well as the interface is necessary to assess the performance of the assembly.

- These standards do not account for the loads fenestration products are exposed to when installed in structure. Fenestration products are inherently susceptible to the movement structures experience (Blackall 1984) (due to different physical loads, expansion due to heat, etc.). This redistribution of loading may open new migration paths for water and merits further research.

The American Architectural Manufacturers Association made similar notes of existing standards and produced a Voluntary Specification for Rating the Severe Wind Driven Rain Resistance of Windows, Doors and Unit Skylights (AAMA 520). The concept is to apply a spectrum of pulsating pressure and rain loads to determine how well a product performs in wind driven rain over a range of severities. The product receives a "score" on a scale of 1 to 10 based on its ability to prevent a volume of water greater than 15mL from entering the structure (see table 6.4 and figure 6.6). This is a significant departure from the usual practice of test standards, which are based on pass/fail criteria.

Table 6.4 AAMA 520 Performance Levels

Performance Level	Lower Limit	Median	Upper Limit
1	239.4 Pa (5.0 psf)	478.8 Pa (10.0 psf)	718.2 Pa (15.0 psf)
2	284.3 Pa (6.0 psf)	574.6 Pa (12.0 psf)	852.8 Pa (18.0 psf)
3	335.2 Pa (7.0 psf)	670.3 Pa (14.0 psf)	1005.5 Pa (21.0 psf)
4	383.0 Pa (8.0 psf)	766.1 Pa (16.0 psf)	1149.1 Pa (24.0 psf)
5	340.9 Pa (9.0 psf)	861.9 Pa (18.0 psf)	1022.8 Pa (27.0 psf)
6	378.8 Pa (10.0 psf)	957.6 Pa (20.0 psf)	1136.4 Pa (30.0 psf)
7	526.7 Pa (11.0 psf)	1053.4 Pa (22.0 psf)	1580.0 Pa (33.0 psf)

8	574.6 Pa (12.0 psf)	1149.1 Pa (24.0 psf)	1723.7 Pa (36.0 psf)
9	622.4 Pa (13.0 psf)	1244.9 Pa (26.0 psf)	1867.3 Pa (39.0psf)
10	670.3 Pa (14.0 psf)	1340.7 Pa (28.0 psf)	2011.0 Pa (42.0 psf)

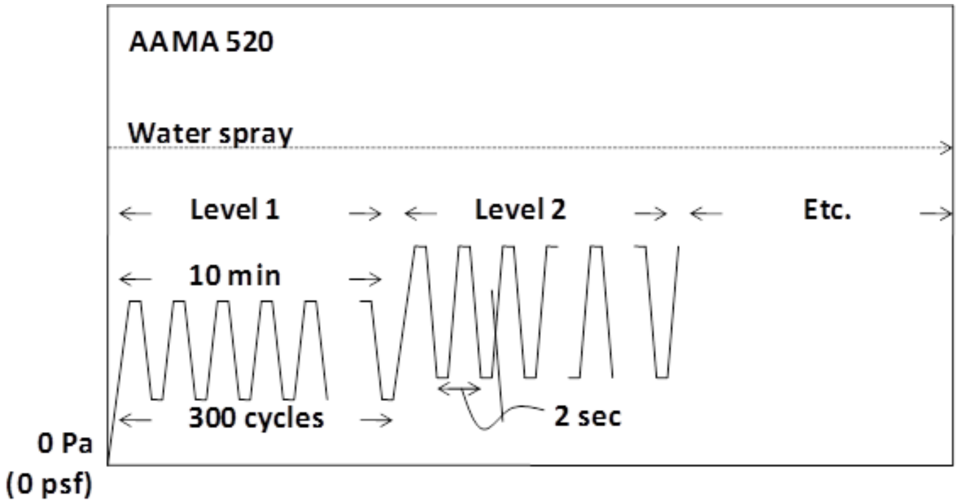

Figure 6.10. AAMA 520 Pressure Loading History

6.3.4 Pseudo-Dynamic Pressure

In 2005, AAMA drafted a voluntary specification that tests products for water penetration using dynamic pressure (AAMA 501.1). It utilizes a spray system in compliance with ASTM E331 and "a wind generating device, such as an aircraft propeller, (that) shall be capable of producing a wind stream equivalent to the required wind velocity pressure." The wind generating device is calibrated to produce minimum of 3 test pressures (from 300 Pa, 380Pa, 480 Pa, 580 Pa, and 720 Pa) at four radially equidistant locations. The wind speed tolerance shall be within ±1.1 m/s (±2.5 mph) of the desired calculated wind speed. The test consists of applying the specified wind speed and spray for a period of 15 minutes. Water infiltration is then documented, quantified, and defined as "as any uncontrolled water that appears on any normally exposed interior surfaces, that is not contained or drained back to the exterior, or that can cause damage to adjacent materials or finishes."

While this test attempts to more accurately reproduce field conditions, it raises a concern by allowing wind generators such as a propeller. Intrinsically by using a propeller without a method for flow straightening, the flow field is radially non-uniform and possesses significant vorticity. The velocity field produced by the propeller increases radially outward from the center of the propeller, resulting in pressures at the perimeter being much greater than those near the center. In extreme cases there may even be a flow reversal near the center of propeller. Given this phenomenon the calibration procedure is not effective since pressure measurements are taken at locations are that are radially equidistant from the center and by definition should yield similar pressures. In addition there is an induced spiral component of motion to rain droplets which would wet the face of the specimen unnaturally and may cause or inhibit water intrusions that are representative of service conditions.

TAS 100 and TAS 100(A) overcome this limitation by requiring the wind generating device to produce a constant wind profile (within ± 10% of the required axial wind velocity) across the width of the test specimen, up to a wind speed of 49.2 m/s (110 mph). These tests provide the constant wind profile desired for testing; however, they are limited to the evaluation of the performance of discontinuous roof systems, soffit ventilation, and a continuous or intermittent ridge area ventilation system (i.e., ridge vents, static vents, turbines or powered vents).

6.4. Full-Scale Experiments

Authors: Arindam Chowdhury, Anne Cope, Forrest Masters

The wide range of adverse effects of wind-driven rain on building structures created the need for repeatable experimental study in controlled testing setups. This requires characterization of the physical processes (wind and rain) to replicate their natural contents relevant to the engineering application. The following sections provide information on the simulation of wind driven rain and full-scale testing methods currently in use.

6.4.1 Rain Simulation

Wind-driven rain is a two-phase dispersed fluid flow consisting of high turbulent wind and raindrops falling with terminal velocities. The free-field wind-driven rain is characterized by mean wind speed profile, turbulence intensity, integral length scale, spectral energy content, raindrop size distribution, and terminal velocity of drops. Separate characterization of the two fluid flow systems can be accomplished through data collected during actual storms. The range of values for the above governing parameters is mainly determined by the nature of storm and topographical conditions. Nowadays, there is enormous effort of research to characterize the nature of wind-driven rain due to its wide application to engineering structures such as hygrothermal study of building envelope, damage studies during extreme weather condition (Lopez et al. 2011a).

Many challenges are present in simulation of combined flow field of wind and rain including, requisite accuracy of measurement of drop size distribution and scarcity of available data to validate target models especially on wind-driven rain associated with extreme weather condition. Measurement of wind-driven rain is highly prone to error due to deflection and interference of the equipment body in the flow being measured. Some of the source of errors include, splashing, evaporation, and adhesion. Studies indicated that there could be up to 6% difference of measurement between repeated tests with similar setup (Schick 2007a).

The conventional method of generating wind-driven rain is to use water jet sprayed using nozzles of selected size and capacity. The water flow rate and pressure need to be controlled in order to generate certain range of raindrop size distributions that comply with the real storm data.

6.4.1.1. Nozzle Selection

Generation of realistic wind-driven rain requires the selection appropriate type of nozzles (opening shape and angle) and their arrangement in the testing setup. The wind-driven rain flow characteristic is a function of flow discharge behavior from individual nozzles. The raindrops from each nozzle are formed when volume of water is forced to pass through nozzle opening under specified discharge rate and pressure – referred as *atomization process*. The atomization process starts with shaping of the 3D volume of water to tiny *sheet*, which is then forced to emerge as *ligaments* (or separated volume-segments) of water as it passes through the geometrical shape of the spray nozzle. The water ligaments further break up into small pieces of water volume called *drops*, *droplets*, or *liquid particles*. The process is controlled by the potential energy of the flow, which is a function of the flow rate and pressure (Schick 2007b). The shape of the final drops is determined by flow energy and the nozzle opening geometry.

The flow inside a nozzle is governed by equation 6.12, where Q1 and P1 are rated flow and rated pressure which can be found form the manufacturers' manuals, and Q2 and P2 are the required flow and pressure. The value for n ranges from 0.44 to 0.50 (Knasiak et al. 2005).

$$\frac{Q_1}{Q_2} = \left(\frac{P_1}{P_2}\right)^n \tag{6.12}$$

The required pressure P2 is calculated from equation 6.12 based on the flow rate needed to generate the required rain intensity.

6.4.1.2. Drop Size Distribution

The drop size distribution of nozzle generated rain flow is controlled by many factors including nozzle type (opening shape), flow rate, pressure, liquid properties, and spray angle. The nozzle type or opening shape usually defines the shape of the emerging fluid flow pattern; *flat spray*, *full cone*, or *hollow cone*. For a specified level of flow rate and pressure, the hollow cone pattern produces the smallest size of raindrops while the full cone drop size gives the largest drops (Knasiak et al. 2005). As it is indicated in equation 6.12, the flow rate and the pressure have opposite effect on size of the raindrops being generated. Increasing of the flow rate at a constant pressure will result in increasing of the drop size. Increasing of the pressure at a constant flow rate will decrease the drop size. Higher spray angles also result in decreasing of the drops size (Knasiak et al. 2005).

The drop size distribution from individual nozzle can be defined either in spatial or temporal scale. The spatial distribution is an instantaneous characterization of number and size of drops within a unit volume of air. The temporal distribution is based on examining individual drops passing through given cross-sectional area within certain interval of time. Generally, the scale to be implemented depends on the application type and capability of measuring instrument. Temporal scale is recommended for widely spaced particles while spatial is good in case of closely spaced particles. The spatial scale based simulation which defines the drop size distribution per cubic meter of air per diameter of drop class (m-3 mm-1) is usually preferred for simulation of the free-field wind-driven rain. The average terminal velocities of raindrops with diameters within a specific range (categorized under a specific *bin*) can be used to transform drop size distribution function from spatial to temporal scale or vice versa, provided sampling error such as recirculation of rain drops is minimal (ASTM 2007).

As noted in the previous sections, the accuracy of drop size distribution also depends on the measurement technique being implemented. This is because of the limitations (in optical configuration and sampling techniques) and the different types of distribution function built in the drop analyzers. Most type of drop analyzers use a single default built-in distribution function to convert the optical information to a meaningful drop size distribution. Some of the most common cumulative density functions used in analyzers setting are Rosin-Rammler distribution function, lognormal distribution, and distribution function developed according to the *ASTM E799-03* standard for determining data criteria and processing for liquid drop size analysis (Schick 2007b).

The Rosin-Rammler distribution function is usually applied for study of size distribution of particles formed with various diameters. The cumulative function, which is useful in determination of the amount of water carried by raindrops having diameter less than D, is given by;

$$F(D) = 1 - exp\left[-\left(\frac{D}{\overline{\overline{D}}}\right)^{N}\right] \tag{6.13}$$

where F(D) is the mean drop diameter; N is the measure of the spread of drop sizes. The lognormal distribution is normal distribution of the natural logarithm of the variable. It is given by;

$$F(D) = \frac{1}{D\sigma\sqrt{2\pi}} e^{-\frac{lnD}{2\sigma^2}} \tag{6.14}$$

The ASTM E799-03 provides criteria and procedures for determining appropriate sample size, size class widths, characteristic drop sizes, and dispersion measure of drop size distribution. The method is best suited for drop count data collected based on sizes. It uses the lognormal distribution function to fit the cumulative liquid volume with particle diameter class.

Definitions and terminologies of drop size analysis

Some common statistical parameters are used in the characterization of the wind-driven rain flow field as the integral of the drop size distribution. The notations are adapted from ASTM E779-03 (ASTM 2007):

$$\overline{D}_{pq}^{(p-q)} = \frac{\sum_i D_i^p}{\sum_i D_i^q} \tag{6.15}$$

where:

$\overline{D}$ = the over bar in $\overline{D}$ designates an average process,

$(p-q)\ p > q$ = the algebraic power of $\overline{D}_{pq}$,

$p \text{ and } q$ = the integers 1, 2, 3, or 4,

D_i = the diameter of the *i*th drop, and

$\sum_i$ = the summation of D_i^p or D_i^q, representing all drops in the sample

Some of the interpretations of common derivatives of eq. 6.15 follow;

$\sum_i D_i^0$ = the total number of drops in the sample,

$\overline{D}_{10}$ = linear (arithmetic) mean diameter,

$\overline{D}_{20}$ = surface area mean diameter,

$\overline{D}_{30}$ = volume mean diameter,

$\overline{D}_{32}$ = volume/surface mean diameter (Sauter), and

$\overline{D}_{43}$ = mean diameter over volume

Volume Median Diameter (VMD/ DV50): A drop diameter in the drop size distribution at which 50% of the total volume of water sprayed is made up of drops with diameter smaller or equal to the volume median diameter.

DV10: A drop diameter in the drop size distribution at which 10% of the total volume of water sprayed is made up of drops with diameter smaller or equal to DV10 value. It is related to the drift potential of the drop size distribution.

DV90: A drop diameter in the drop size distribution at which 90% of the total volume of water sprayed is made up of drops with diameter smaller or equal to DV90 value.

Relative Span Factor (RSF): A dimensionless parameter which indicates the uniformity of drop size distribution. RSF is defined as:

$$RSF = \frac{D_{V90} - D_{V10}}{D_{V50}} \tag{6.16}$$

The ASTM 779-03 Standard also provides a detailed procedure and criteria on how to control the error inherent in measuring and analysis of drop size distribution. The use of a distribution function in characterization of the nozzle generated wind-driven rain flow should be justified with all the procedures, assumption and correction applied in the process. This can be accomplished through any statistical method of examining the best-fit application of a distribution function to a set of drop size data. Clearly identified methodology: sampling technique, use of measurement technology (or accuracy of measurement), and method of analysis play important role in the resulting characteristics of drop size information of wind-driven rain flow (ASTM 2007).

6.4.2. Pressure Loading Actuator

Pressure Loading Actuator (PLA) is a controllable dynamic loading system used to regenerate realistic pressure loads using blower fan and flexible airbag system. The concept is first developed to replicate the spatial and temporal details of wind pressure on building facade without the need to reproduce the entire wind flow field, thereby reduce the testing cost significantly (Cook et al. 1988; Kopp et al. 2010). The PLA enables to investigate the response of buildings and their components under hurricane wind load through tracing of predetermined area-based pressure applied to finite regions of the building envelope. The spatial representation is ensured by using as many PLA systems running simultaneously with individually dictated pressure tracing. Higher number of PLA systems is required in the region of high spatial pressure variation. The time variation in the tracing of time history pressure data is usually controlled by computer programs. This enables to improve the traditional testing procedure (testing under uniform static or cyclic loading as commonly suggested by building codes and standards) as it uses either real storm or wind tunnel load data.

The system is versatile to accommodate the temporal change of hurricane wind speed and direction as in real storms. It can also incorporate other type of hurricane induced loads, such as wind-driven rain and wind-borne debris together with the pressure loading to make a complete assessment of damage resistance. It is apparent that the method is easily applicable to building facade with simple geometrical shapes and more convenient to study the component-wise wind-driven rain effects on building structures. For studies involving damage, correction should be considered for area based pressure loading (and rain intrusion testing result) due to lack of consequent fluid flow modification as a result of damaged building components. Some previous building component studies for wind and wind-driven rain effects using PLA include, wind-borne damage to windows and fatigue failure of roof cover under fasteners (Kopp et al. 2010), study of static wind loading for roofing panel (Surry et al. 2007), study of water penetration resistance of residential windows using high airflow PLA (Lopez et al. 2011b).

The apparent similarity requirement for testing using PLA system is derived from the ability to regenerate the target pressure load time history, which is derived from either wind tunnel or real storm data. The governing parameter is usually taken to be the frequency content of the predetermined pressure load. In the application of wind-driven rain, the PLA system follows spraying of water impinging velocity and drop size distribution irrespective of realistic wind-driven rain characteristics as prescribed by codes and standards. Though spatial and temporal distribution of water drops in the testing chamber with respect to the exposure area of the testing specimen controls the amount of water ingress through the specimen, the subject is still not covered in up-to-date study of the wind-driven rain effects using such loading mechanism.

6.4.3. Wind Tunnel Simulation

Wind tunnel simulation of wind-driven rain involves major challenges. It requires simultaneous scaling of wind and rain. Inherent in the simulation of the flow field, it is difficult to maintain all the similarity requirements of non-dimensional parameters between model (wind tunnel) and prototype (full-scale). In order to generate these similarity requirements, the scaling based on dimensionless parameters such as Reynolds number (Re) and Froude number (Fe), must be applied to reproduce the natural characteristics of the full-scale free-field wind-driven rain flow.

6.5.3.1. Similarity Requirement

The similarity requirements of the governing non-dimensional parameters between model and prototype in the experimental simulation of wind-driven rain can be derived from the governing equations of the flow as presented by Inculet, 2001 or using the classical dimensional analysis of PI theorem as shown below. For the steady-state wind-driven rain flow, the driving force, *F*, on a single droplet of rain can be expressed as a function of the following six parameters; relative velocity $(V_r = V_t - U)$, drop size d, density of air ρ_a, density of water ρ_w, viscosity of air μ, and acceleration due to gravity g. Hence,

$$F = V_r^{\alpha}\, d^{\beta}\, {\rho_a}^{\gamma}\, {\rho_w}^{\delta}\, \mu^{\varepsilon}\, g^{\zeta} \tag{6.17}$$

where α,β,γ,δ,ε and ζ are exponents to be determined. The basic independent quantities involved are mass (M), length (L), and time (T). Note that the dimensions of all the above parameters can be expressed in terms of the independent parameters. Thus, expressing eq. 6.16 in dimensional form:

$$\frac{ML}{T^2} = \left(\frac{L}{T}\right)^{\alpha} (L)^{\beta} \left(\frac{M}{L^3}\right)^{\gamma} \left(\frac{M}{L^3}\right)^{\delta} \left(\frac{M}{LT}\right)^{\varepsilon} \left(\frac{L}{T^2}\right)^{\zeta} \tag{6.18}$$

Comparing the exponents of the independent dimensions from both sides of eq. 6.18, one can derive the following three equations:

$$\begin{aligned} 1 &= \gamma + \delta + \varepsilon \\ 1 &= \alpha + \beta - 3\gamma - 3\delta - \varepsilon + \zeta \\ -2 &= -\alpha - \varepsilon - 2\zeta \end{aligned} \tag{6.19-6.21}$$

Solving for $\alpha, \beta, and\ \gamma$;

$$\begin{aligned} \alpha &= 2 - \varepsilon - 2\zeta \\ \beta &= 2 - \varepsilon + \zeta \\ \gamma &= 1 - \delta - \varepsilon \end{aligned} \tag{6.22-6.24}$$

Hence, equation 6.14 becomes

$$F = V_r^{2-\varepsilon-2\zeta}\, d^{2-\varepsilon+\zeta}\, {\rho_a}^{1-\delta-\varepsilon}\, {\rho_w}^{\delta}\, \mu^{\varepsilon}\, g^{\zeta} \tag{6.25}$$

This can be rearranged to:

$$F = \rho_a V_r^2 d^2 \left(\frac{\rho_w}{\rho_a}\right)^\delta \left(\frac{\mu}{\rho_a V_r d}\right)^\varepsilon \left(\frac{gd}{V_r^2}\right)^\zeta \tag{6.26}$$

Equation 6.26 shows that the driving force coefficient on a raindrop is a function of three non-dimension parameters; density ratio, Reynolds number, and Froude number. The density ratio is satisfied in wind tunnel simulations. The challenge remains in simulating the two non-dimensional flow parameters, Reynolds number (*Re*) and Froude number (*Fe*), as expressed below.

$$\left(\frac{\rho_a V_r d}{\mu}\right)_{fs} = \left(\frac{\rho_a V_r d}{\mu}\right)_{ms} ; \qquad \left(\frac{V_r^2}{gd}\right)_{fs} = \left(\frac{V_r^2}{gd}\right)_{ms} \tag{6.27}$$

where *fs* and *ms* refer to full-scale and model-scale, respectively. Further analysis of scaling based on the Reynolds number requirement indicates that the velocity scale is inversely related to the length scale; while Froude numbers similarity requirement suggests the length scale should be the square of the velocity scale. This indicates that simultaneous satisfaction of the similarity requirements would be impossible unless the scaling is kept to be unity (Simiu 2011). The errors due to violation of similarity requirements can be addressed through sensitivity analysis and correction factors can be applied to improve upon the test results. The length scale of wind tunnel testing which involves wind-driven rain simulation needs to be kept as large as possible in order to avoid evaporation of droplet before reaching the building facade.

6.4.4. Full-Scale Simulation

Large and full-scale testing approach for investigating hurricane induced load effects on building structures is important to advance our understanding of the nature of wind load and the consequent progressive physical damage phenomena. Such testing is capable of capturing all the detailed spatial and temporal effects including coupling of wind loads with structural responses. It is advantageous for studying the wind pressure distribution on building façade with complex and detailed architectural features since it can allow such structures to be prototyped without any distortion that may be caused due to scaling. Large and full-scale testing approach for wind is an important toolbox in identifying realistic failure modes through destructive testing and in developing innovative mitigation technologies. It can also accommodate simultaneous testing of wind and wind-driven rain. Large –scale simulation entails reproduction of requisite volume of air flow to completely engulf the building model. This requires the use of high performance fans arranged in array format with active and passive flow controlling systems. The maximum size of models can be determined through systematic blockage effect experiments (Aly et al., 2011).

Many testing facilities for large- and full-scale simulation of wind and wind-driven rain are being developed and used in recent years to study hurricane induced damage to low-rise buildings. Some of the current testing facilities include: "Three Little Pigs" (Kopp et al. 2010) and the Wind Engineering, Energy and Environment (WindEEE) Dome (Natarajan and Hangan 2010) at the University of Western Ontario, Hurricane Simulator at the University of Florida (UF) (Mensah et al. 2011), the Wall of Wind at the Florida International University (FIU) (Aly et al. 2011), the new multi-peril facility of the Institute of Business and Home Safety (IBHS) (Liu et al. 2011), and Cyclone Testing Station at James Cook University, Australia.

In general, full-scale simulation of wind-driven rain presents less challenges and result in more realistic fluid flow compared to rain representation in scaled boundary layer wind tunnel. The rain is usually generated using a nozzle rack placed in front of the exit of the fan system. The selection of the nozzle type should be chosen to generate the target characteristic parameters of wind-driven rain. The rain rate is controlled by the water flow rate in the main supply pipe.

The accuracy and repeatability of test results depend on realistic representation of the target parameters derived from hurricane wind and rainfall data. The governing parameters include mean wind speed profile corresponding to the exposure condition, turbulence intensity, integral length scale, spectral energy content of the flow, raindrop size distribution, and terminal velocity of drops. Similarity requirements are applicable with scale of unity to assure reasonable representation of the flow.

Chapter 7. References

Abuku, M., Blocken, B., and Roels, S. (2009). "Moisture response of building facades to wind-driven rain: Field measurements compared with numerical simulations." *J. Wind Eng. Ind. Aerodyn.*, 97, 197-207.

Abuku, M., Janssen, H., Poesen, J., and Roels, S. (2009). "Impact, absorption and evaporation of raindrops on building facades." Building and Environment, 44, 113-114.

Aly, A.M., Chowdhury, A.G., and Bitsuamlak, G. (2011). "Wind profile management and blockage assessment for a new 12-fan Wall of Wind facility at FIU." *Wind and Structures*, 14(4), 1-16.

American Society for Testing and Materials. (2007). "Standard practice for determining data criteria and processing for liquid drop size analysis." *E799 - 03*, (14.02), 271-275.

American Society for Testing and Materials. (2007). "Standard Test Method for Water Penetration of Exterior Windows, Skylights, Doors, and Curtain Walls by Uniform Static Air Pressure Difference." 51-54.

American Society for Testing and Materials. (2010). "Standard Test Method for Water Penetration of Exterior Windows, Skylights, and Doors by Rapid Plused Air Pressure Difference." 493-498.

Amirkhanian, S., Sparks, P., and Watford, S. (1994). "A Statistical Analysis of Wind Damage to Single-Family Dwellings Due to Hurricane Hugo." In: Baker, N. and Goodno, B. (eds.) *Proc., Structures Congress XII*, ASCE, 1042-1047.

AMS Glossary, Allen Press, http://amsglossary.allenpress.com/glossary, 2012.

American Society of Civil Engineers. (2012); "ASCE 7-10: Minimum design Loads for Buildings and Other Structures." *Am. Soc. Civil Engineers*, Reston, VA.

Axe, L. (2003). "Hurricane surface modeling for risk management." Master's thesis, The Florida State University College of Arts and Sciences.

Basart A. (1946). "Verhandeling inzake de regenval op het verticale vlak met betrekking tot de bouwconstructie." Technical Report (In Dutch), Instituut voor warmte-economie TNO. Keramisch Instituut TNO.

Bergeron, T. (1937). "On the Physics of Fronts." *Bulletin of the American Meteorological Society*, V. 18, 265-275.

Best, A.C., (1950a). "Empirical formulae for the terminal velocity of water drops falling through the atmosphere." *Q. J. R. Meteorol. Soc.*, 76, 302–311.

Best, A.C. (1950b). "The size distribution of raindrops." *Q. J. R. Meteorol. Soc.*, 76, 16–36.

Birkeland O. (1965). General report. Rain penetration. RILEM/CIB Symposium on Moisture Problems in Buildings, Rain Penetration, Helsinki, August 16-19, Vol. 3, paper 3-0.

Bitsuamlak, G. T., Chowdhury, A. G., and Sambare, D. (2009). "Application of a full-scale testing facility for assessing wind-driven-rain intrusion." *Building and Environment,* 44, 2430–2441.

Blackall T.N., Baker M.C. (1984). "Rain Leakage of Residential Windows in the Lower Mainland of British Columbia." *Division of Building Research National Research Council of Canada*.

Blocken, B., Abuku, M., Nore, K., Briggen, P.M., Schellen, H.L., Thue, J.V., Roels, S., and Carmeliet, J. (2011). "Intercomparison of wind-driven rain deposition models based on two case studies with full-scale measurements." *Journal of Wind Engineering and Industrial Aerodynamics* 99(4), 448-459.

Blocken, B., Carmeliet, J. (2002). "Spatial and temporal distribution of driving rain on a low-rise building." *Wind and Structures* 5(5), 441-462.

Blocken, B., Carmeliet, J. (2004). "A review of wind-driven rain research in building science." *Journal of Wind Engineering and Industrial Aerodynamics*, 92(13), 1079-1130.

Blocken, B., Carmeliet, J. (2005). "High-resolution wind-driven-rain measurements on a low-rise building – experimental data for model development and model validation." *Journal of Wind Engineering and Industrial Aerodynamics*, 93(12), 905-928.

Blocken, B., Carmeliet, J. (2006a). "On the accuracy of wind-driven rain measurements on buildings." *Building and Environment*, 41(12), 1798-1810.

Blocken, B., Carmeliet, J. (2006b). "The influence of the wind-blocking effect by a building on its wind-driven rain exposure." *Journal of Wind Engineering and Industrial Aerodynamics*, 94(2), 101-127.

Blocken, B., Carmeliet, J. (2007). "On the errors associated with the use of hourly data in wind-driven rain calculations on building facades." *Atmospheric Environment,* 41(11), 2335-2343.

Blocken, B., Deszö, G., van Beeck, J., Carmeliet, J. (2010). "Comparison of calculation methods for wind-driven rain deposition on building facades." *Atmospheric Environment,* 44(14), 1714-1725.

Blocken, B., Roels, S., Carmeliet, J. (2007). "A combined CFD-HAM approach for wind-driven rain on building facades." *Journal of Wind Engineering and Industrial Aerodynamics*, 95(7), 585-607.

Blocken, B., Dezso, G., van Beeck, J. and Carmeliet, J., (2010). "Comparison of calculation models for wind-driven rain deposition on building facades." *Atmospheric Environment*, 44, 1714-1725.

Blocken, B. and Carmeliet, J. (2008). “Guidelines for the required time resolution of meteorological input data for wind-driven rain calculations on buildings.” *Journal of Wind Engineering and Industrial Aerodynamics*, 96, 621-639.

Blocken, B. and Carmeliet, J. (2010). “Overview of three state-of-the-art wind-driven rain assessment models and comparison based on model theory.” *Building and Environment,* 45(3), 691-703.

Blocken, B. and Carmeliet, J. (2012). “A simplified numerical model for rainwater runoff on building facades: possibilities and limitations.” *Building and Environment,* 53, 59-73.

Blocken, B., and Carmeliet, J. (2005). "High-resolution wind-driven rain measurements on a low-rise building—experimental data for model development and model validation." *J. Wind Eng. Ind. Aerodyn.*, 93, 905-928.

Blocken, B., and Carmeliet, J. (2006a). "The influence of the wind-blocking effect by a building on its wind-driven rain exposure." *J. Wind Eng. Ind. Aerodyn.*, 94(2), 101-127.

Briggen, P.M., Blocken, B., Schellen, H.L. (2009). “Wind-driven rain on the facade of a monumental tower: numerical simulation, full-scale validation and sensitivity analysis.” *Building and Environment*, 44(8), 1675–1690.

Choi, E.C.C. (1991). “Numerical simulation of wind-driven-rain falling onto a 2-D building.” *Proc., Asia Pacific Conference on Computational Mechanics*, Hong Kong. 1721-1728.

Choi, E.C.C. (1993). “Simulation of wind-driven rain around a building.” *Journal of Wind Engineering and Industrial Aerodynamics,* 46-47, 721-729.

Choi, E.C.C. (1994a). “Determination of wind-driven rain intensity on building faces.” *Journal of Wind Engineering and Industrial Aerodynamics*, 51, 55-69.

Choi, E.C.C. (1994b). “Characteristics of the co-occurrence of wind and rain and the driving-rain index.” *Journal of Wind Engineering and Industrial Aerodynamics*, 53, 49-62.

Choi, E.C.C. (2008). “The Effect of Wind-Driven Rain on Cladding Pressure of Buildings Under Wind and Rain Conditions.” *BBAA VI International Colloquium on: Bluff Bodies Aerodynamics & Applications*. Milano, Italy. 20-24 July 2008.

Chowdhury, A. G., Bitsuamlak, G. T., Fu, T.-C., and Kawade, P. (2011). "A study on roof vents subjected to simulated hurricane effects." *Natural Hazards Review, ASCE* 12(4), 158-165.

Cook, N. J., Keevil, A. P., and Stobart, R. K. (1988). "BRERWULF—The big bad wolf." *J. Wind Eng. Ind. Aerodyn.*, 29, 99-107.

Crandell, J. (1998). “Statistical assessment of construction characteristics and performance of homes in Hurricanes Andrew and Opal.” *Journal of Wind Engineering and Industrial Aerodynamics,* 77, 695-701.

Crandell, J., Nowak, M., Laatsch, E., van Overeem, A., Barbour, C., Dewey, R., Reigel, H., and Angleton, H. (1993). “Assessment of Damage to Single-Family Homes caused by Hurricanes Andrew and Iniki.” NAHB Research Center. Technical Report prepared for U.S. Dept. of Housing and Urban Development – Office of Policy Development. Report HUD-0006262.

Crandell, J., Gibson, M., Laatsch, E., Nowak, M. and van Overeem, J. (1994). “Statistically-Based Evaluation of Homes Damaged by Hurricanes Andrew and Iniki.” In Cook, R. and Sotani M. (ed.) (1994). *Hurricanes of 1992: Lessons Learned and Implications for the Future*. New York: ASCE. 519-528.

Dalgliesh, W.A., Surry D. BLWT, CFD and HAM modelling vs. the real world: Bridging the gaps with full-scale measurements. Journal of Wind Engineering and Industrial Aerodynamics 2003; 91(12-15): 1651-1669.

Dao, T. N. , and van de Lindt, J. W. (2012). “Loss Analysis of Woodframe Buildings During Hurricanes. I: Structure and Hazard Modeling”. *ASCE Journal of Performance of Constructed Facilities*, (In press).

Dao, T. N. and van de Lindt, J. W (2008), “New nonlinear roof sheathing fastener model for use in finite element wind load applications”, *Journal of Structural Engineering, ASCE*, 134(10), 1668-1674.

Dao, T. N. and van de Lindt, J. W. (2010). “Methodology for Wind-Driven Rain Water Intrusion Fragilities for Light-Frame Wood Roof Systems.” *Journal of Structural Engineering, ASCE*, 136(6), 700-706.

Dingle, A.N., Lee, Y. (1972). “Terminal fall speeds of raindrops.” *Journal of Applied Meteorology,* 11, 877-879.

Dunne, T., Leopold, L.B. (1995). “Water in Environmental Planning.” W.H. Freeman Publisher.

Ellingwood, B. R., Rosowsky, D. V., Yue Li, S., and Kim, J. H. (2004). “Fragility Assessment of Light-Frame Wood Construction Subjected to Wind and Earthquake Hazards.” *Journal of Structural Engineering*, 130(12), 1921 - 1930.

Engineering, University of Waterloo, Ontario, Canada, 318 pp.

Fazio, P., Athienitis, A., Marsh, C., Rao, J. (1997). “Environmental Chamber for Investigation of Building Envelope Performance.” *Journal of Architectural Engineering*, 3(2), 97-102.

Federal Emergency Management Agency. (2005). “FEMA 490 Summary Report on Building Performance, 2004 Hurricane Season.” Federal Emergency Management Agency, Washington, DC.

Federal Emergency Management Agency. (2006). “FEMA 549, Summary Report on Building Performance: Hurricane Katrina 2005.” Federal Emergency Management Agency, Washington, DC.

FEMA-HAZUS. (2006). “HAZUS-MH-MR3.” *Multi-hazard Loss Estimation Methodology Hurricane Model Technical Manual*. Department of Homeland Security, Federal Emergency Management Agency, Mitigation Division, Washington, D.C.

Florida Public Hurricane Loss Model, v5.0 Submission document to the Florida Commission on Hurricane Loss Projection Methodology, 2013, www.sbafla.com

Flower, J.W., Lawson, T.V. (1972). “On the laboratory representation of rain impingement on buildings.” *Atmospheric Environment*, 6, 55-60.

Franklin, J., Black, M., and Valde, K. (2003). “GPS Dropwindsonde Wind Profiles in Hurricanes and their Operational Implications.” *Weather and Forecasting*, 18(1), 32-44.

Fuchs, N. 1964. The mechanics of aerosols. Oxford: Pergamon Press.

Gjelsvik T. (1983). “Apparatus for Accelerated Weathering of Building Materials and Components.” *Materials and Structures*, 16(3), 209-211.

Guillermo, F., Green, R., Khazai, B., Smyth, A., and Deodatis, G. (2010). “Field Damage Survey of New Orleans Homes in the Aftermath of Hurricane Katrina.” *Natural Hazards Review*, 11, 7-18.

Gunn, R. and Kinzer, G.D. (1949). “The terminal velocity of fall for water droplets in stagnant air.” *J. Meteor.*, 6, 243-248.

Gurley K. and Masters F. (2011). “Post 2004 Hurricane Field Survey of Residential Building Performance.” *Natural Hazards Review*, 12(4), 177-183.

Hamid, S., Pinelli, J.-P., Cheng, S.-C., and Gurley, K. (2011). “Catastrophe Model Based Assessment of Hurricane Risk and Estimates of Potential Insured Losses for the State of Florida.” *Natural Hazard Review,* 12(4), 171-183.

Hendry, I.W.L. (1964). "Comparison between two types of wall rain gauges." Building Research Station, Internal note, SL/IN.1.

Högberg, A.B., Kragh, M.K., van Mook, F.J.R. (1999). “A comparison of driving rain measurements with different gauges.” *Proc., 5th Symposium on Building Physics in the Nordic Countries*, Gothenburg, 361-368.

Holland, G. (1980). “An Analytic Model of the Wind and Pressure Profiles in Hurricanes.” *Monthly Weather Review*, 108(8), 1212-1218.

Inculet, D. and Surry, D. (1995). “Simulation of wind-driven rain and wetting patterns on buildings.” BLWT-SS30-1994, Boundary Layer Wind Tunnel, University of Western Ontario.

Inculet, D. R. (2001). "The design of cladding against wind-driven rain." *PhD dissertation*, University of Western Ontario.

ISO. (2009). “Hygrothermal performance of buildings – Calculation and presentation of climatic data – Part 3: Calculation of a driving rain index for vertical surfaces from hourly wind and rain data.” ISO 15927-3:2009 International Organization for Standardization.

Jameson, A. R., Kostinski, A. B., and Kruger, A. (1999). “Fluctuation properties of precipitation. Part IV: Finescale clustering of drops in variable rain.” *J. Atmos. Sci.,* 56**,** 82–91.

Jameson, A.R. and Kostinski, A.B. (2000). “Fluctuation Properties of Precipitation. Part VI: Observations of Hyperfine Clustering and Drop Size Distribution Structures in Three-Dimensional Rain.” *Journal of the Atmospheric Sciences*, 57(3), 373-388.

Janssen, H., Blocken, B., Carmeliet, J. “Conservative modelling of the moisture and heat transfer in building components under atmospheric excitation*.”* *International Journal of Heat and Mass Transfer*, 50(5-6): 1128-1140.

Katsaros, J.D., Hardman, B.G. (2007). “Failed Fenestration: New Materials Require New Techniques.” *Proc., Thermal Performance of the Exterior Envelopes of Whole Buildings X International Conference, ASHRAE*.

Kennedy, Charles E. (1999). “*Feasability Study for a Full-Scale Wind Test Facility*.” MS thesis. Clemson University, Clemson, Print.

Keyser, D. and Shapiro, M.A. (1986). “A Review of the Structure and Dynamics of Upper-Level Frontal Zones.” *Monthly Weather Review*, 114, 452-499.

Knasiak, K., Schick, R. J., and Kalata, W. (2005). "Multiscale design of rain simulator." *Spray Analysis and Research Services, Spray Systems Co.*, Wheaton, IL.

Kopp, G. A., Morrison, M. J., Gavanski, E., Henderson, D. J., and Hong, H. P. (2010). "“Three Little Pigs” project: Hurricane risk mitigation by integrated wind tunnel and full-scale laboratory tests." *Natural Hazards Review,* 11(4), 151-161.

Kragh, M. K. (1998). "Microclimatic conditions at the external surface of building envelopes." *Ph.D. Thesis.* Department of Buildings and Energy Technical University of Denmark.

Lacy, R. (1965). "Driving-rain maps and the onslaught of rain on buildings." *RILEM/CIB symposium on moisture problems in buildings, rain penetration*, Helsinki, Finland, 3-4.

Lindgren O. Climate Data OS Parameters for The Design of an Equipment for Accelerated Ageing of Windows and Other Wood-Based Products. Swedish Council for Building Research, 1984; 1: 195-199.

Liu, Z., Brown, T. M., Cope, A. D., and Reinhold, T. A. (2011). "Simulation wind conditions/events in the IBHS research center full-scale test facility." *Proc., 13 Int'l Congress on Wind Engineering (13ICWE)*, Amsterdam, Netherlands.

Lonfat, M., Marks Jr, F. and Chen, S. (2004). "Precipitation distribution in tropical cyclones using the Tropical Rainfall Measuring Mission (TRMM) microwave imager: A global perspective." *Monthly Weather Review*, 132(7), 1645-1660.

Lonfat, M., Rogers, R., Marchok, T. and Marks, F. (2007). "A parametric model for predicting hurricane rainfall." *Monthly Weather Review*, 135(9), 3086-3097.

Lopez, C., Masters, F. J., and Bolton, S. (2011b). "Water penetration resistance of residential window and wall systems subjected to steady and unsteady wind loading." *Building and Environment*, 46, 1329-1342.

Lopez, C., Masters, F., and Friedrich, K. (2011a). "Capturing and characterization of wind-driven rain during tropical cyclones and supercell thunderstorms." *Proc., 13 Int'l Congress on Wind Engineering (13ICWE)*, Amsterdam, Netherlands.

Lopez, C.R., Masters, F.J. and S. Bolton, (2011). "Water Penetration Resistance of Residential Window and Wall Systems Subjected to Steady, Rapid Pulsed and Fluctuating Wind Load Pressures." *Building and Environment*, 46, 1329-1342.

Marks, F., Atlas, D. and Willis, P. (1993). "Probability-matched reflectivity: rainfall relations for a Hurricane from aircraft observations." *Journal of Applied Meteorology*, 32(6), 1134-1141.

Marshall, J.S. and Palmer, W.M. (1948). "The distribution of raindrops with size," *J. Meteor.*, 5, 165-166.

Masters, F.J., Gurley, K.R., Prevatt, D.O. (2008). "Full-scale simulation of turbulent wind-driven rain effects on fenestration and wall systems." *Proc., 3rd International Symposium on Wind Effects on Buildings and Urban Environment, Tokyo, Japan*.

Masters, F.J., Vickery, P.J., Bacon, P. and Rappaport, E.N. (2010). "Toward Objective, Standardized Intensity Estimates from Surface Wind Speed Observations." Bulletin of the American Meteorological Society, 91(12), 1665-1682.

Masters, Forrest, David Prevatt, and Kurt Gurley. 2010. *Reduction of Wind-Driven Rain Intrusion through the Building Envelope*.

Mensah, A.F., Datin, P.L., Prevatt, D.O., Guptab, R., and van de Lindt, J.W. (2011). "Database-assisted design methodology to predict wind-induced structural behavior of a light-framed wood building." *Engineering Structures*, 33, 674-684.

Mileti, D. (1999). “Disasters by design: A reassessment of natural hazards in the United States.” National Academy Press.

Min, S-K, Zhang, X., Zwiers, F.W. and Hegerl, G.C. (2011). “Human contribution to More-Intense Precipitation Extremes.” *Nature*, 470, 378-381.

Moore, J.T. and Smith, K.F. (1989). “Diagnosis of Anafronts and Katafronts.” *Weather and Forecasting*, 4, 61-72.

Mulvin, L., Lewis, J.O. (1994). “Architectural detailing, weathering and stone decay.” *Build Environ*, 29(1), 113-138.

Natarajan, D., and Hangan, H. (2010). "Preliminary numerical simulation of axi-symmetric flows in WindEEE dome facility." *Proc., The Fifth International Symposium on Computational Wind Engineering (CWE2010)*, Chapel Hill, North Carolina, USA.

National Institute of Standards and Technology. (2005). “Performance of Physical Structures in Hurricane Katrina and Hurricane Rita: A Reconnaissance Report.” NIST Technical Note 1476 2005.

NWS. (1977). Five- to 60-minute precipitation frequency for the eastern and central United States. NOAA Technical Memorandum NWS HYDRO-35. National Weather Service.

Orville, R.E., Huffines, G.R., Burrows, W.R., and Cummins, K.L. (2011). “The North American Lightning Detection Network (NALDN)—Analysis of Flash Data: 2001-09.” *Monthly Weather Review*, 139, 1305-1322.

Pinelli, J.-P., Pita, G., Gurley, K., Torkian, B., Hamid, S., and Subramanian, C. (2011). “Damage Characterization: Application to Florida Public Hurricane Loss Model.” *Natural Hazard Review*, 12(4), 190-195.

Pita, G. (2012). “Hurricane Vulnerability of Commercial-Residential Buildings.” Ph.D. Dissertation. Department of Civil Engineering. Florida Institute of Technology.

Pita, G.L., Pinelli, J.-P. , Cocke, S., Gurley, K., Mitrani-Reiser, J., Weekes, J., and Hamid, S. (2012). “Assessment of hurricane-induced internal damage to low-rise buildings in the Florida Public Hurricane Loss Model.” *Journal of Wind Engineering & Industrial Aerodynamics*, 104-106, 76-87.

Polovkas, V.G and R.A Thompson. (1952). “A storm protection laboratory for testing buildng components and other materials under hurricane conditions.” Department of Aeronautical Engineering, University of Florida, Bulletin Series No. 56.

Proc. of the International Building Physics Conf., Eindhoven, The Netherlands.

Rayment R, and Hilton M. (1977). “The use of bubbles in a wind tunnel for flow-visualisation and the possible representation of raindrops.” *Journal of Industrial Aerodynamics*, 2, 149-157.

Quarles, S.L., Brown, T.M., Cope, A.D., Lopez, C., and Masters, F.J. (2012). “Water Entry through Roof Sheathing Joints and Attic Vents: A Preliminary Study.” *Proc., ATC-SEI, Miami, FL, USA.*

S. Twomey. (1977). “Atmospheric aerosols.” Elsevier Scientific Publishing Company, Amsterdam.

Salzano, C.T., Masters, F.J., and Katsaros, J.D. (2010). “Water Penetration Resistance of Residential Window Installation Options for Hurricane-Prone Areas.” *Building and Environment*, 45(6), 1373-1388.

Sanders C. (1996). “Heat, air and moisture transfer in insulated envelope parts: Environmental conditions.” International Energy Agency, Annex 24. Final report, volume 2. Acco, Leuven.

Schick, R.J., (1997). “Spray Technology Reference Guide: Understanding Drop Size.” Spray Analysis and Research Analysis.

Schick, R. J. (2007a). "General guidelines on drop size measurement techniques and terminology." *Spray Analysis and Research Services, Spray Systems Co.*, Wheaton, IL.

Schick, R. J. (2007b). "Spray technology reference guide: Understanding drop size." *Spray Analysis and Research Services, Spray Systems Co.*, Wheaton, IL.

Sheffield, J. (1994). “Survey of building performance in Hurricane Iniki and Typhoon Omar.” In Cook, R. and Sotani M. (ed.) (1994). *Hurricanes of 1992: Lessons Learned and Implications for the Future*. New York: ASCE. 446-455.

Simiu, E. and Miyata, T. (2006). “Design of buildings and bridges for wind: a practical guide for ASCE-7 standard users and designers of special structures.” Wiley.

Simiu, E. (2011). "Design of buildings for wind: A guide for ASCE 7-10." John Wiley.

Smith, T. (1994). “Causes of Roof Coverage Failure and Damage Modes: Insights provided by Hurricane Andrew.” In Cook, R. and Sotani M. (ed.) (1994). *Hurricanes of 1992: Lessons Learned and Implications for the Future*. New York: ASCE. 303-312.

Sparks, P. (1991).” Development of the South Carolina Coast 1959-1989: Prelude to a Disaster.” In Sill, B. and Sparks, P. (eds.). *The Symposium and Public Forum on Hurricane Hugo One Year Later*, 1-7.

Sparks, P. (2003). “Wind speeds in tropical cyclones and associated insurance losses.” *Journal of Wind Engineering and Industrial Aerodynamics*, 91(12-15), 1731-1751.

Sparks, P. and Bhinderwala, S. (1994). "Relationship between residential insurance losses and wind conditions in Hurricane Andrew." In Cook, R. and Sotani M. (ed.) (1994). *Hurricanes of 1992: Lessons Learned and Implications for the Future*. New York: ASCE. 111-124.

Sparks, P., Schiff, S., and Reinhold, T. (1994). "Wind damage to envelopes of houses and consequent insurance losses." *Journal of Wind Engineering and Industrial Aerodynamics*, 53(1-2), 145-155.

Straube, J.F., Burnett, E.F.P. (2000). "Simplified prediction of driving rain on buildings." *Proc. of the International Building Physics Conference, Eindhoven, The Netherlands*, 375-382.

Straube, J.F. (1998). "Moisture control and enclosure wall systems." Ph.D. thesis, Civil Engineering, University of Waterloo, Ontario, Canada, 318 p.

Straube, J. and Burnett, E. (2000). "Simplified prediction of driving rain on buildings." *Proc., International Building Physics Conference*, 375-382.

Surry, D., Inculet, D.R., Skerlj, P.F., Lin, J.X., and Davenport A.G. (1994). "Wind, rain and the building envelope: a status report of ongoing research at the University of Western Ontario." *Journal of Wind Engineering and Industrial Aerodynamics,* 53: 19-36.

Surry, D., Sinno, R. R., Nail, B., Ho, T. C. E., Farquhar, S., and Kopp, G. A. (2007). "Structurally effective static wind loads for roof panels." *Journal of Structural Engineering,* 133(6), 871-885.

Sutton, O.G. (1942). "Investigations on falling drops carried out at the Chemical Defense Experimental Station, Porton." *Meteor. Res. Paper*, 40, 9.

Tang, W., Davidson, C.I., Finger, S., and Vance, K. (2004). "Erosion of limestone building surfaces caused by wind-driven rain. 1. Field measurements." *Atmospheric Environment*, 38(33), 5589-5599.

Ulbrich, C.W. (1983). "Natural Variations in the Analytical Form of the Raindrop Size Distribution." *Journal of Climate and Applied Meteorology* 22, 1764-1775.

Unanwa C.O., McDonald, J.R., Mehta, K.C., Smith, D.A. (2000). "The development of wind damage bands for buildings." *Journal of Wind Engineering and Industrial Aerodynamics*, 84, 119-149.

Underwood and Meentemeyer, (1998). "Climatology of wind-driven rain for the contiguous United States for the period 1971 to 1995." *Physical Geography*, 19(6), 445-462.

US-HUD – United States Department of Housing and Urban Development (1993). "Assessment of Damage to Single-Family-Homes Caused by Hurricanes Andrew and Iniki." Report HUD-PDandR – 1432.

van de Lindt, J.W., A. Graettinger, R. Gupta, T. Skaggs, S. Pryor, and K. Fridley. 2007. “Performance of Woodframe Structures During Hurricane Katrina.” *Journal of Performance of Constructed Facilities*; 21(2); 108-116.

van Mook, F.J.R. (1999). "Full-scale measurements and numeric simulations of driving rain on a building." *Proc., 10th International Conference on Wind Engineering*, Kobenhavn, 21-24.

van Mook, F.J.R. (2002). "Driving rain on building envelopes." *Ph.D. Thesis, Building Physics Group (FAGO)*, Eindhoven University of Technology, Eindhoven University Press, Eindhoven, the Netherlands.

van Mook, F.J.R., de Wit, M. H. and Wisse J. A. (1997). “Computer Simulation of Driving Rain on Building Envelopes.” *Proc., 2nd European and African Conference on Wind Engineering*, Genova, 22–26.

van Straaten, R.A., Kopp, G.A., and Straube, J.F. (2010). "Testing water penetration resistance of window systems exposed to “realistic” dynamic air pressures." *Proc., International Conference on Building Envelope Systems and Technologies (ICBEST 2010)*, Vancouver, Canada, 299-305.

Vickery, P. (2005). “Simple empirical models for estimating the increase in the central pressure of tropical cyclones after landfall along the coastline of the United States.” *Journal of Applied Meteorology*, 44(12), 1807-1826.

Vickery, P. and Skerlj, P. (2005). “Hurricane gust factors revisited.” *Journal of Structural Engineering*, 131, 825-832.

Willis, P.T., Tattelman, P. (1989). “Drop-Size Distribution Associated With Intense Rainfall.” *Journal of Applied Meteorology,* 28, 3-15.

Appendix
Research Summary Performed for Task 3

Introduction

The following text was excerpted from the first draft of the thesis of the graduate student supported by this project (Brian Rivers), which will be defended on July 2, 2013. Findings should be considered preliminary until the thesis is finalized. A copy of the thesis will be forwarded to the program manager when it becomes available (late summer).

Scope of Research

A variable wetting rain rack was added to the high airflow pressure loading actuator (HAPLA) to simulate realistic wind-driven rain conditions to determine if the water ingress caused by a real, time-varying event can be estimated from the results of simplified test methods, i.e. tests that apply a steady pressure and wetting rate. Only minor modification to the test methods (e.g., ASTM E331-00, TAS 202-94) would be necessary to collect these data.

The first phase of testing subjected window assemblies to steady wind load and wetting conditions. Four dynamic pressure sequences were then applied to the window specimen at each wetting rate to study the correlation between water ingress behavior under static and dynamic load scenarios. The final testing phase replicated pressure and wind-driven rain sequences derived from Hurricane Ike (2008).

Specimen Construction

8 ft x 8 ft light-framed wood walls were built to match the dimensions of the pressure chamber, with the subjected window centered on the wall. The wall was constructed of 1/2” plywood fastened to 2x4 studs spaced at 16 in o.c. and covered with a vapor barrier to allow the wall to shed water quickly. Each window was installed and sealed into a 2x4 frame that could be interchanged in the test wall. The test frame was sealed with GE Clear Silicone Window and Door Caulk (Model LW5000) around its perimeter on both the exterior and interior to prevent water from migrating around the window. Flashing tape was then applied over the perimeter of the window frame and the test wall to prevent water from entering through the vapor barrier. Thus water can only migrate through the window and not through the window-wall interface.

Window Specimens

Dimension of each window specimen were recorded so that comparisons can be made with the amount of water ingress with respect to each design. The dimensions of primary concern are difference between interior and exterior sill dam height on the bottom of the window, and the difference in elevation of the top of the bottom siding frame, and the bottom of the top widow frame. The location of the seal at the locking mid-section of the window varies greatly, and is assumed to have little effect on the amount of water ingress due to the lack of continuity to the edges of the window where the water typically penetrates, instead of the middle.

The specimens were as follows:

Specimen B-1

Window specimen B-1 was 62 inches tall and 36 inches wide and had a positive design pressure of 56.7 psf. Per the fenestration industry standard AAMA/ WDMA/CSA 101/I.S.2/A440-05, the water penetration resistance requirement for this window is 8.5 psf of static pressure before leakage begins. The elevation difference that the pressure must overcome to move water over the top of the lower window assembly is 0.625 inches. The applied static pressure equivalent to 0.625 inches of water column is 3.25 psf. The difference in elevation the water is required to overtop the bottom sill dam is 1.625 inches. The applied static pressure equivalent to 1.625 inches of water column is 8.45 psf.

Specimen B-2

Window specimen B-2 was 59-3/4 inches tall and 35-7/8 inches wide and had a positive design pressure of 50 psf. Per the fenestration industry standard AAMA/ WDMA/CSA 101/I.S.2/A440-05, the water penetration resistance requirement for this window is 7.5 psf of static pressure before leakage begins. The elevation difference that the pressure must overcome to move water over the top of the lower window assembly is 1.875 inches. The applied static pressure equivalent to 1.875 inches of water column is 9.75 psf. The difference in elevation the water is required to overtop the bottom sill dam is 1.125 inches. The applied static pressure equivalent to 1.125 inches of water column is 5.85 psf.

Specimen C-1

Window specimen C-1 was 62-1/2 inches tall and 43-1/2 inches wide and had a positive design pressure of 35 psf. Per the fenestration industry standard AAMA/ WDMA/CSA 101/I.S.2/A440-05, the water penetration resistance requirement for this window is 5.25 psf of static pressure before leakage begins. The elevation difference that the pressure must overcome to move water over the top of the lower window assembly is 0.875 inches. The applied static pressure equivalent to 0.875 inches of water column is 4.55 psf. The difference in elevation the water is required to overtop the bottom sill dam is 1.625 inches. The applied static pressure equivalent to 1.625 inches of water column is 8.45 psf.

Specimen C-2

Window specimen C-2 was 62-1/2 inches tall and 43-1/2 inches wide and had a positive design pressure of 65 psf. Per the fenestration industry standard AAMA/ WDMA/CSA 101/I.S.2/A440-05, the water penetration resistance requirement for this window is 9.75 psf of static pressure before leakage begins. The elevation difference that the pressure must overcome to move water over the top of the lower window assembly is 1.625 inches. The applied static pressure equivalent to 1.625 inches of water column is 8.45 psf. The difference in elevation the water is required to overtop the bottom sill dam is 1.1875 inches. The applied static pressure equivalent to 1.1875 inches of water column is 6.18 psf.

This information is summarized below:

Window Specimen	Height (in.)	Width (in.)	Design Pressure (psf)
B-1	62	36	56.7
B-2	59 – 3/4	35 – 7/8	50
C-1	62 – 1/2	43 – 1/2	35
C-2	62 – 1/2	43 – 1/2	65

Testing Apparatus

Loads were applied using the high airflow pressure loading actuator (HAPLA) described in the previous report. The HAPLA is powered by two backward inclined 75 horsepower centrifugal blowers connected in series. The fans connect to an air valve with five ports: intake from the fans, exhaust to the fans, atmospheric intake, atmospheric exhaust, and a service port that connects to the test chamber. A circular aluminum disc with two sections cut out rotates between the ports to adjust the density of the air in the test chamber, thus changing the static pressure in the test chamber. The valve can oscillate the static pressure in the test chamber at a frequency up to 3 Hz.

The HAPLA incorporates a two-phase spray rack, which enables both high and lower wetting rates to be simulated. For this testing only one rack was used, which is composed of a three by three grid of 120 degree nozzles. The spray racks are regulated using mechanical ball valves, and monitored with flow meters to ensure consistent wetting rates throughout all testing. Excess water collecting in the base of the test chamber is evacuated using a submersible 1/3 horsepower pump, which recirculates the water back to the storage tank. An emergency evacuation valve is also installed at the base of the chamber to reduce the load on the submersible pump. A V-shaped channel approximately four inches wide is welded the length of the test chamber below the specimen to collect any water that escapes through the gasket between the specimen and the bottom of the test chamber.

Water is collected in a shallow V-shaped trough at the base of the window, which is then directed into a bucket. A ¼” thick sheet of polycarbonate is fastened to the exterior of the wall behind the window to deflect water droplets into the basin at the bottom. An aluminum lip at the bottom of the polycarbonate sheet ensures that all water droplets are collected and do not evade the basin. The bucket that the basin drains into is suspended from a load cell with a 25 lb. capacity.

The program for the static and dynamic pressure sequences operates in the National Instruments Labview environment. Static pressure readings in the test chamber are taken at a frequency of 50 Hz in conjunction with load cell output. The wetting rate and valve position for the rain rack was recorded at the beginning and end of each test and then recorded to ensure that it remained constant throughout.

Testing Procedure

The experimental testing procedure was divided into four phases. The first phase of testing was carried out determine the pressure at which leakage begins. The second phase of applied multiple wetting rates at four pressures evenly spaced between the pressure associated with the threshold of leakage and 75% of the design pressure of the window. The third phase applied dynamic loading over four intensity levels. The final phase was conducted using dynamic pressure traces representative of conditions during Hurricane Ike (2008). Boundary Layer Wind Tunnel data were used to derive the dynamic pressure load sequence.

A total of 172 tests were performed:

Phase	Pressure Levels	Wetting Rates	Windows	Total Tests
I	4	1	4	16
II	4	4	4	64
III	4	4	4	64
IV	7	-	4	28

Phase I: Determination of the threshold of leakage

The primary goal of the initial phase of testing is to determine the minimum applied static pressure at which each window will begin leaking. A constant wetting rate of 8 in/hr was chosen following the recommendation in AAMA/WDMA/CSA 101/I.S.2/A440-2005. The pressure was manually increased in increments of 0.5 psf, pausing for 30 seconds at each level to check for ingress. The test terminated when leakage was noted. This pressure was recorded.

Phase II: Variable Wetting Rate and Pressure Levels

Windows were subjected to four wetting rates and static pressures (16 total tests). The lower and upper bounds of the pressures corresponded to the initial leakage pressure and 75% of the positive design pressure of the window. The middle two values for pressure were chosen such that the pressure difference between levels equaled 1/3 of the range. Each window was subjected to a 10 minute duration load sequence at four wetting rates: 150, 200, 250 and 300 mm/hr.

Phase III – Dynamic Pressure Sequences of Specified Interval

The first phase of dynamic pressure testing incorporates the procedure described above. The pressure trace was specified to four levels with evenly distributed mean static pressures of 0.36, 0.44, 0.52 and 0.60 kPa. The peak pressure load in each trace was approximately three times the mean value. The wetting rates were identical to Phase II. A detailed description of the method to compute the pressure sequence follows.

The dynamic pressure loading sequences were produced using wind tunnel modeling pressure sequence for building SS20 – Test 4, from the NIST Aerodynamic Database, with modeling and testing performed by the University of Western Ontario. The subject building selected was a 1:12 slope gable-end structure with an eave height of 7.3 m (24 ft), and plan dimensions of 19 m x 12.2 m (62.5ft x 40 ft), constructed at a scale of 1:100. The condition of the upwind wind tunnel terrain was modeled to open country. For this study internal pressure measurements were due to distributed leakage. A Scanivalve pressure scanning system sampled the static pressure at 500 Hz. Pressure coefficient data was taken at wind angles divided into 5° increments.

The complete dataset for the model was analyzed to locate the highest mean positive pressure coefficient, C_p, defined as:

$$C_p = \frac{p - p_{ref}}{\frac{1}{2}\rho {U_{ref}}^2} \tag{1}$$

where p is the pressure measured at the location on the model that exhibited the highest mean positive pressure, p_{ref} is the pressure measured at the reference location, U_{ref} is the velocity taken at the reference height, and ρ is the air density. The roof height was used as the reference location, using referencing factors provided on the NIST website. The record was derived from tap 3901 at an approach angle of 55°, which produced the maximum mean C_p = 0.96, with a C_p maxima of 2.84. This peak C_p value of 2.84, $C_{p,max}$ is assumed to provide an accurate estimate of the peak load acting on the wall. Using this assumption, the design pressure, P_f, can then be calculated using the following equation:

$$P_f = \tfrac{1}{2}\rho {U_h}^2 C_{p,max} \tag{2}$$

where U_h is the mean velocity at the eave height and the full scale pressure. P_f is a predetermined vector of four static pressures based on the design pressures of the particular window to produce evenly distributed pressure levels. In this case the desired or target peak pressures that will be used are 1.08, 1.32, 1.56, and 1.80 kPa.

The full-scale frequency of the record must be solved for using the reduced frequency relationship to determine the time step size required for the full scale pressure time history.

$$\frac{f_f L_f}{U_f} = \frac{f_m L_m}{U_m} \tag{3}$$

Solving for f_f,

$$f_f = f_m \frac{L_m}{L_f} \frac{U_f}{U_m} \tag{4}$$

Where f_f is the frequency at full scale, f_m is the sampling frequency at model scale, L_m is the test building scale, L_f is the building component scale, U_f is the velocity at the full scale reference height, and U_m is the velocity at the model reference height. The time increment dt is the inverse of f_f and used to create the pressure sequence. The time increment is found from:

$$\Delta t_f = \frac{1}{f_f}$$

The data are then resampled to 50 Hz for compatibility with the HAPLA control system and desired rate of sampling for recording ingress data. The resulting pressure sequence was then subjected to a 3-Hz Butterworth filter to improve the controllability of the HAPLA.

The pressure loading sequence was constructed using the desired P_f level and the f_f calculated for that particular case of P_f. The load sequence begins with a short ramp to 50% of the desired pressure level and then begins a 10 minute dynamic pressure sequence before returning to 50% of the desired static pressure for a very brief period before ramping down. The figure below shows the resulting target time history for pressure level 3.

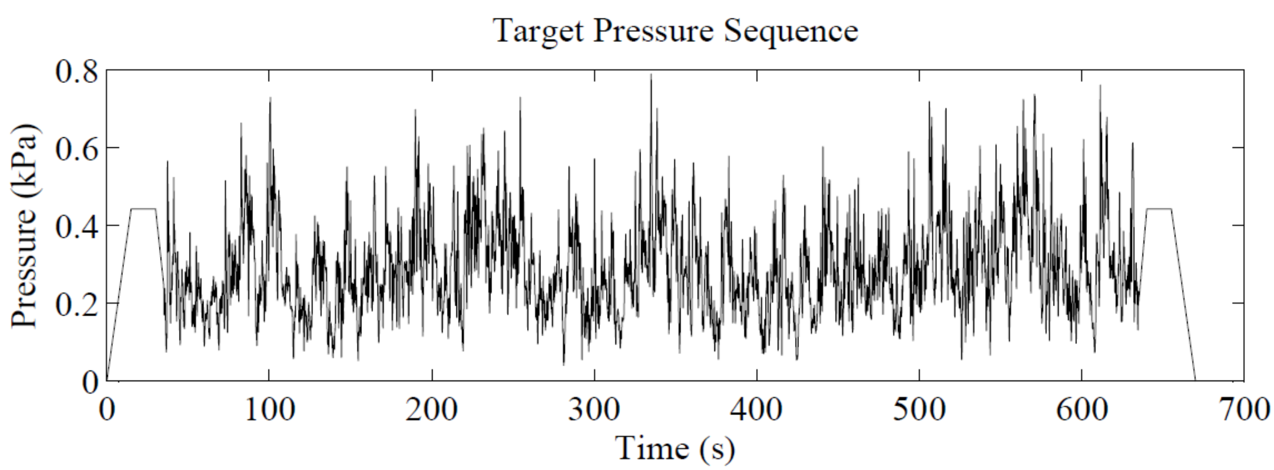

Phase IV – Hurricane Ike Representative Pressure Sequences

This phase of testing used data collected from a FCMP portable weather station during Hurricane Ike in 2008 to derive site-specific velocity records and wetting rates that replicate the conditions during an actual storm. Wind tunnel modeling data from a boundary layer wind tunnel was incorporated to compute time-varying pressure sequences.

Data from FCMP weather station T3 in Hurricane Ike was used to develop a time history to simulate a segment of an actual hurricane event. The Contractor deployed T3 in Baytown, TX. It recorded data throughout the approach, passage and departure of the storm, including the passage of the eyewall.

Wind-speed and direction was recorded for 18 hours at a height of 10 m. Because this study is only concerned with the wind and rain as it interacts with a windward facing window, a segment of data about 3 hours long will be selected. This segment is of importance because it represents the time at which the direction of the wind and rain as it impacts the window is approximately perpendicular to the wall. This remaining segment of data will then be separated into segments of 11 to 13 minutes, depending on the length of the corresponding rainfall data, of which the mean wind speed will be extracted and applied to pressure coefficient sequences of 10 minutes.

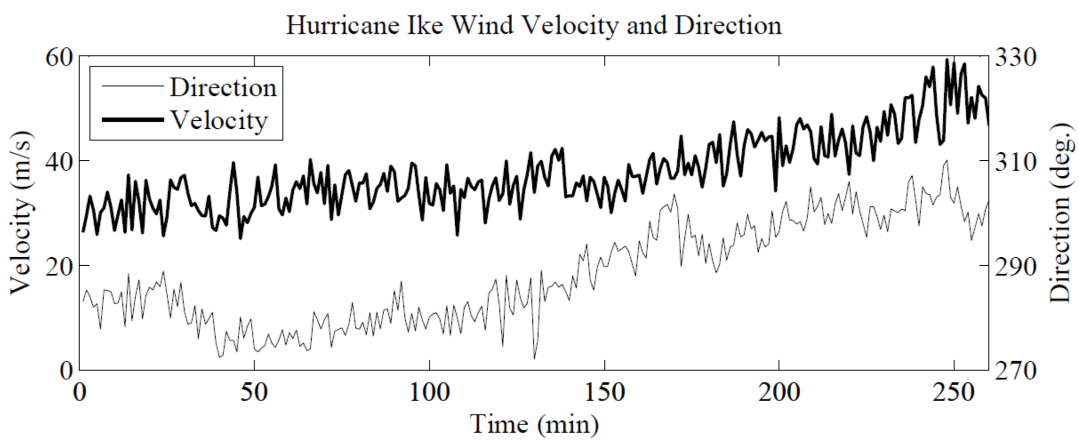

The pressure coefficient data from the above procedure will again be used to produce the pressure sequence. To do so, the velocity which is measured at 10 m must be referenced to the eave height of the model building, which is 7.3 m, using the log law relationship.

$$u_z = \frac{u_*}{k} ln\left(\frac{z}{z_0}\right) \tag{5}$$

Equating the full scale and model scale values, and then solving for the full scale velocity yields:

$$U_{7.3} = U_{10} \frac{ln\left(\frac{7.3}{0.03}\right)}{ln\left(\frac{10}{0.03}\right)} = 0.946\, U_{10} \tag{6}$$

where U_{10} is the velocity measured from the tower at a height of 10 m, $U_{7.3}$ is the velocity at the eave height of the building at a height of 7.3 m, and the roughness length is taken as 0.03 m.

The C_p data from the wind tunnel testing will be extracted and scaled from the reference height to the full scale height of the building using the conversion factors provided in the NIST Aerodynamic Database. To match the full scale wind velocity data taken from the FCMP tower, C_p must be scaled using the following relationship:

$$C_{p,f} = C_{p,m} \left(\frac{U_m}{U_f}\right)^2 \tag{7}$$

where $C_{p,f}$ is the full scale pressure coefficient, $C_{p,m}$ is the pressure coefficient signal taken from the wind tunnel, U_m is the mean wind speed from the wind tunnel taken at the eave height, and U_f is the full scale velocity taken from the FCMP data analysis. The pressure sequence can now be constructed using the following:

$$P_f = C_{p,f} P_{v,h} \tag{8}$$

Taking P_f as the static pressure applied to the test specimen, and:

$$P_{v,h} = \frac{1}{2} \rho \, U_f^{\,2} \tag{9}$$

The time scale for each pressure sequence must be calculated independently because it is dependent upon the velocity used to create the pressure time history. The reduced frequency relationship can be used, as done previously, and this process can be performed for each 10 minute segment of wind data to create multiple pressure sequences that can be used in conjunction with wetting rate histories that simulate the wind driven rain intensity during the velocity record. The construction of these wind driven rain simulations is outlined in the following section.

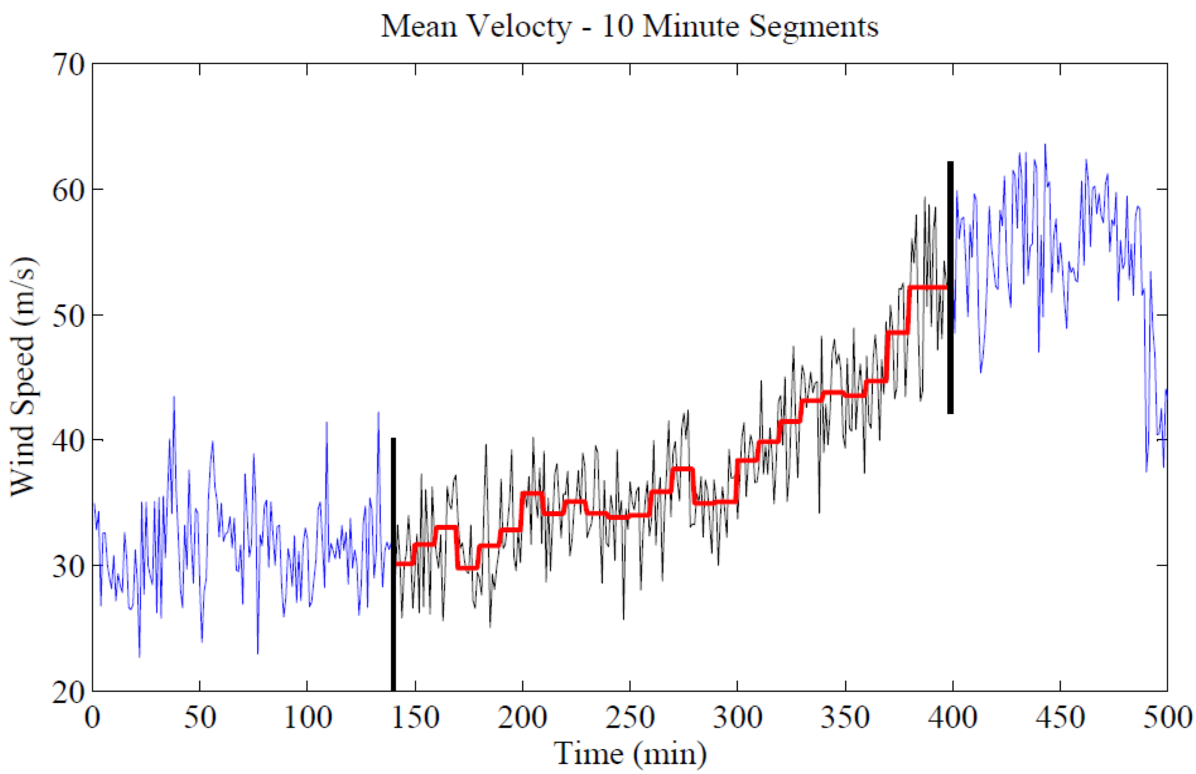

Wind Driven Rain Sequence Generation Using Radar Data

Rainfall intensity estimates from Hurricane Ike were obtained using reflectivity measurements from the National Weather Service WSR-88D Doppler Radar KHGX. The average rainfall intensity is taken for each ten minute velocity segment to produce an average wetting rate for the pressure sequence. The horizontal rainfall intensity is determined using Z-R relationships that convert the average reflectivity for that particular location into an estimated rainfall rate.

The rain racks inside the test chamber of the HAPLA are connected to servo-valves that can adjust the flow rate to the racks to control the wetting rate of the test specimen. Data was collected near FCMP tower T3 during Hurricane Ike to determine horizontal rainfall intensity over the duration of the storm. The data must first be separated into 11 to 13 minute segments with time scales that match the 10 minute velocity segments. Using the following relationship, the wind driven rain intensity, R_{wdr}, can be determined using the known mean wind velocity, U_h, and horizontal rainfall intensity, R_h.

$$R_{wdr} = 0.22\, R_h^{\,0.88} U_h \qquad (10)$$

Once the wind driven rain intensity is determined the equivalent wetting rate, W_r, that should be applied to the specimen can be calculated, and is defined as:

$$W_r = C\, R_{wdr} \cos(\alpha) \qquad (11)$$

where C can range from 0.3 – 0.5. The quantity is multiplied by $\cos(\alpha)$ to correct for the attack angle, α, of the wind relative to the wall. The wetting rate will then be calibrated to the positions of the valves that control flow rate, enabling the rain rack to fluctuate the wind driven rain intensity similar to actual hurricane conditions. Below are figures that show the complete pressure and wetting rate time history for the data extracted from Hurricane Ike.

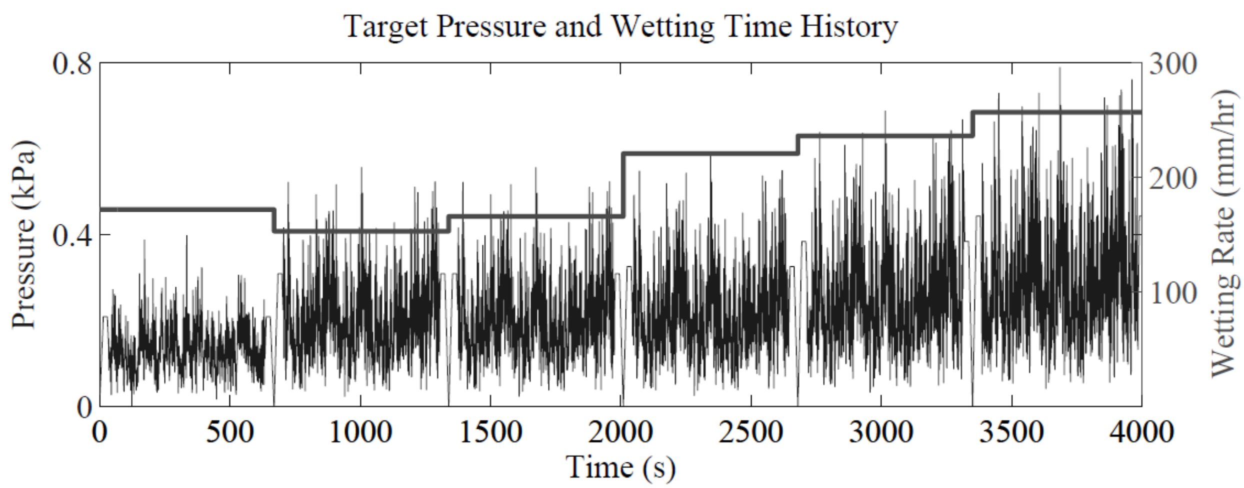

Individual nozzles were tested to determine the nozzle type and spray angle that yielded the most uniform wetting applied to the test specimen. This was carried out using a circular apparatus with bins equally spaced around the center. Nozzles were investigated at varying distances from the target to determine the distance at which greatest uniformity could be achieved. Once the appropriate nozzle was selected, multiple variations of spray nozzle arrays were tested to develop a design with the most uniform wetting rate across the entire test specimen. An array with 9 equally spaced nozzles was selected and offset 1.75 ft from the wall to create the most uniform wetting possible in the chamber, in addition to its ability to operate in the desired range of wetting rates.

Mean Velocity, V_{10min_avg} (m/s)	Mean Wind Direction, θ (deg.)	Horizontal Rainfall Intensity, R_h (mm/hr)	Wind-Driven Rain Intensity, R_{wdr} (mm/hr)	Wetting Rate, W_R (mm/hr)
35.8	65	19.1	378.9	171.7
43.5	90	11.9	305.7	152.8
44.7	90	12.7	331.4	165.7
48.6	90	16.0	441.3	220.6
52.2	85	16.0	474.0	236.1
52.2	90	17.5	513.6	256.8

Prediction of Water ingress: Time-Step Analysis

Pressure load and rate of water ingress were recorded and stored for all levels. The file was analyzed at each time step using the following procedure to build a predicted accumulating total of water ingress through the window based on the initial static testing results.

Initially, a sequence of ingress rate, $I(j)$, for each wetting rate as a function of pressure level, j, were produced from the analysis of the static pressure testing results, which are shown in the figure below. The pressure levels for the window being tested are also included. A vector of length n is created from the pressure recorded in the test chamber throughout the simulation, and is denoted $p(i)$, where i is the time step at which the pressure is being evaluated. The wetting rate vector of length n is also imported, and is denoted as $w(i)$, where i is the time step at which the wetting rate is being considered. The time step size is:

$$\Delta t = \frac{1}{f}$$

where f is the frequency at which the data is recorded. A new water ingress rate curve is determined by interpolating between the known curves to produce a curve on which the pressure at time step i can be interpolated between the known pressure levels, yielding an ingress rate, R(i), for that time step. The cumulative water ingress for each time step, $I_{total}(i)$, is then calculated:

$$I_{total}(i) = R(i) * \Delta t$$

The cumulative ingress curve is then produced by summing I_{total} at each time step i, to replicate the output of the load cell during the test.

Testing

Static Testing

Initial static pressure testing was performed with a constant wetting rate of 8 in/hr. The objective of this phase of testing was to determine the initial static pressure required to initiate water ingress through the window. All windows met the requirement set forth by AAMA/WDMA/CSA 101/I.S.2/A440-05, preventing water ingress up to 15% of the design pressure (see table below).

Window Specimen	Design Pressure	Minimum Pressure Threshold for Water Ingress	Percent of Design Pressure
B-1	56.7	14.0	25
B-2	50	9.0	18
C-1	35	7.5	21
C-2	65	10.2	16

Variable Wetting Rate Testing

The windows were subjected to four wetting rates ranging from 150 and 300 mm/hr and four pressure levels determined ranging from the threshold associated with leakage to 75% of the design pressure.

Target Dynamic Pressure Sequences

Each window was subjected to four dynamic pressure sequences with mean pressures of 0.39, 0.47, 0.56, and 0.64 kPa. Each window specimen was subjected to wetting rates of 150, 200, 250, and 300 mm/hr at each pressure level. The pressure sequences used in this phase were repeated in a time step analysis in conjunction with the ingress rate data obtained in the previous phase to predict the amount of ingress based on the behavior of each window specimen under static load conditions.

Ike Pressure Sequences

Pressure sequences were developed using wind velocity and rainfall rate data measured during Hurricane Ike. Six traces of varying wetting rate and mean pressure were simulated on each window specimen. The wetting rate and pressure sequence were then replicated in a time-step analysis, using the data from the second phase of testing to predict the amount of water ingress during the test. The following section examines the performance of each window during each phase of testing.

Windows

Window B-1

The ingress rate with respect to wetting rate at the lowest pressure level is evenly distributed. However, at the three higher pressure levels, ingress rates for wetting rates of 200 and 250 mm/hr are nearly the same. The initial increase in water ingress rate from the first pressure level to the second is rather large for all wetting rates, but tapers between subsequent pressure levels. This indicates there is possibly an upper limit at which the ingress rate ceases to steadily increase as a function of static pressure. The shape of the ingress curves with respect to wetting rate is similar, making it a good candidate for use in predicting the dynamic behavior, as interpolation will likely be a good representative of actual behavior.

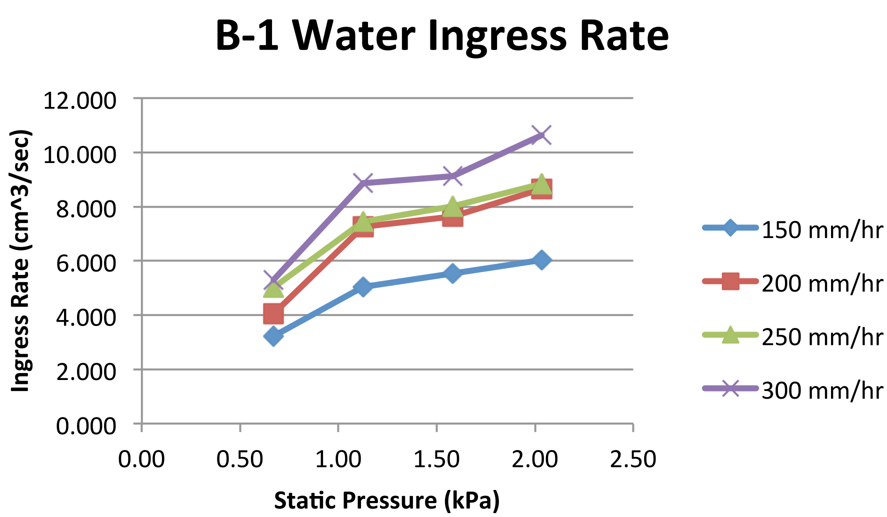

The plot shown in figure below presents the volume of water measured as it accumulates during the dynamic pressure sequence with a mean pressure of 0.64 kPa, and a wetting rate of 250 mm/hr. There is an apparent lag between the predicted and the actual for the first half of the test, possibly due to the accumulation of water that must occur before water overtops the sill. As the test approaches the end, the predicted amount of total ingress falls below the measured ingress, and the final prediction slightly underestimates the actual total.

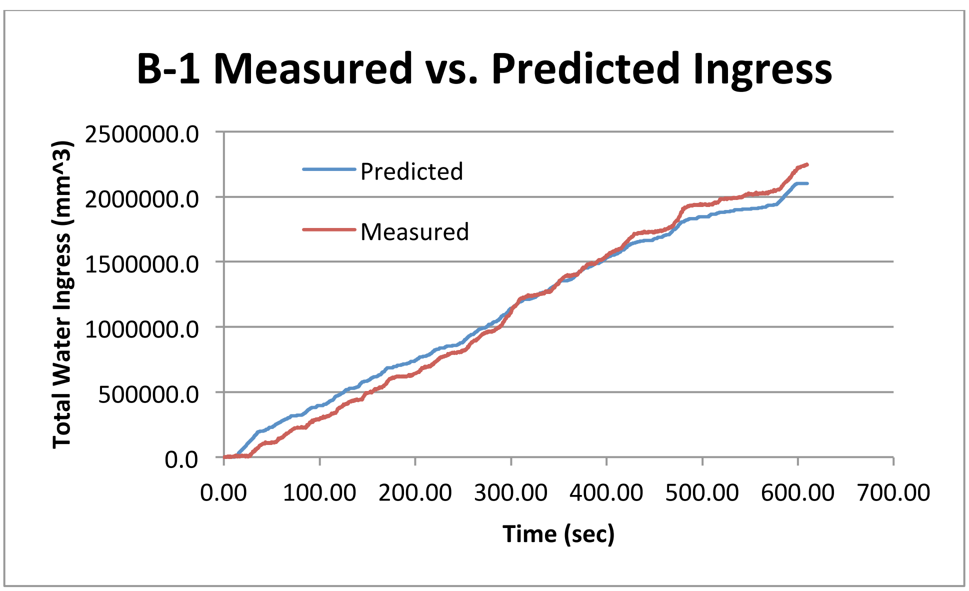

The next figure displays the predicted and measured average ingress rate for the target pressure sequences with multiple wetting rates. For every combination of wetting rate and mean pressure, the predicted ingress rate underestimates the measured ingress rate. One likely possibility is the clustering of the 200 and 250 mm/hr wetting rates during the static testing. The amount that the predicted falls short of the actual is similar for nearly all tests, with the most accurate predictions occurring for the higher wetting rates. The lowest pressure levels yielded the smallest difference in predicted compared to actual for each wetting rate.

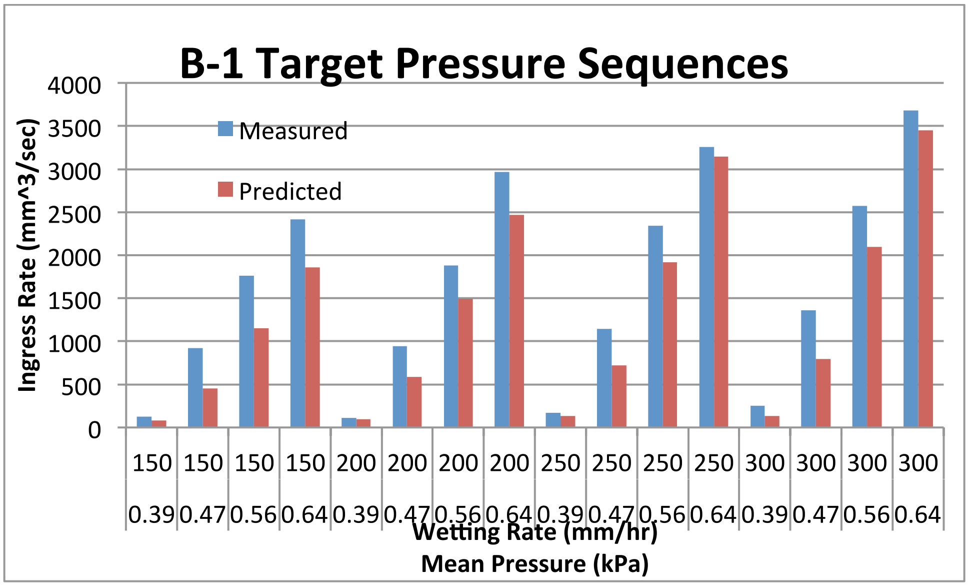

The predicted average ingress rate for the pressure sequence and wetting rate derived from Hurricane Ike are presented in the next figure. There was no measurable water ingress during any of the six pressure sequences. This particular window specimen could withstand the largest static pressure load, 0.67 kPa, before allowing water penetration. No ingress occurred due to the pressures being relatively low, which allows time for the water that accumulates on the sill to drain before the peaks can force it to overtop. The applied static pressure rarely exceeded that value in the two strongest cases, which predicted only a small amount of ingress. The strongest case yielded an average predicted flow rate of approximately 34 mm^3/sec, which is equivalent to a small droplet of water per second. This indicates that the strongest peaks during the pressure sequence rarely exceeded the threshold for ingress to begin.

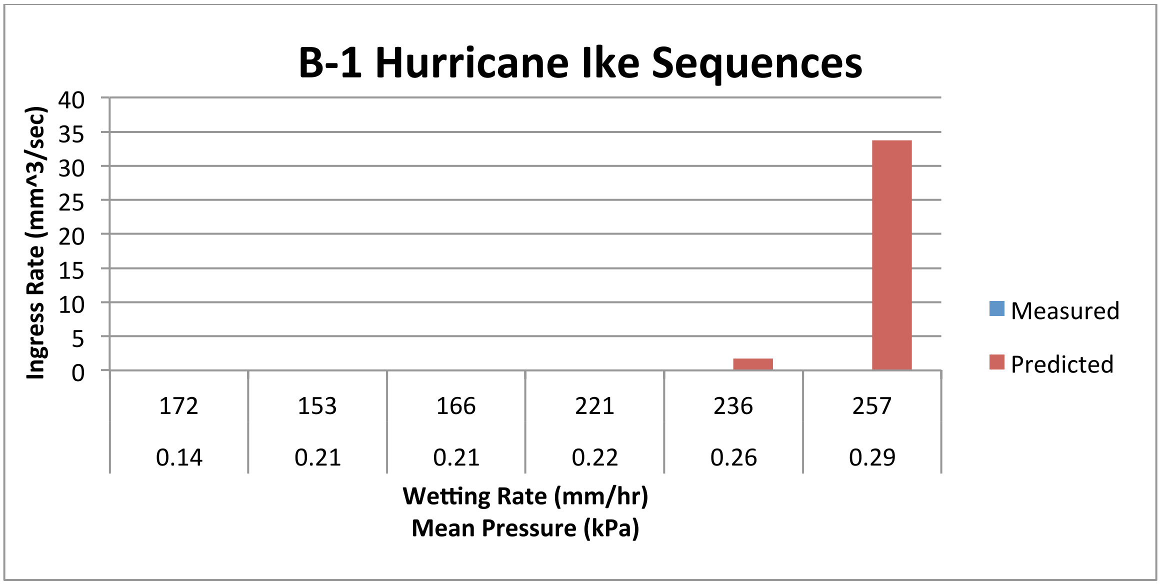

Window B-2

Ingress rates as a function of mean pressure and wetting rate are shown in the figure below for window specimen B-2. At the lowest pressure level, which is the threshold for water ingress, the ingress rate is small, particularly for the 150 mm/hr wetting rate. The rate at which ingress increases with respect to pressure accelerates slightly as the pressure is increased for all wetting rates. The increment in water ingress rate between each wetting rate is similar, with the curves for 200 and 250 mm/hr being slightly closer together, similar to window specimen B-1. The consistency and spacing of the curves would seem to indicate that predictions during the following phase would be very accurate with respect to measured ingress. However, this is not the case, which can be seen in the figure.

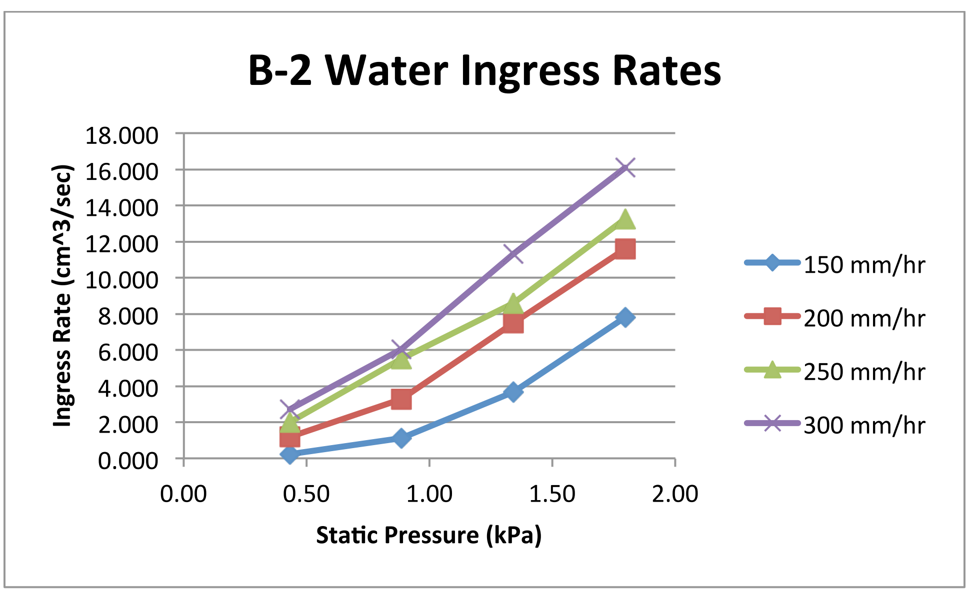

The volume of water ingress measured by the load cell versus the predicted water ingress for a mean pressure of 0.39 kPa and a wetting rate of 300 mm/hr is shown in the figure below. The predicted amount of water ingress has a slightly steeper slope than the measured ingress resulting in an over-estimation that increases with time. The peaks and general shape of the predicted ingress are not apparent in the measured data, which is nearly linear the entire test with slight increases at few points. The portions of the predicted water ingress curve which have a constant slope of zero indicate that the pressure measured during the time history was below the threshold needed for ingress as determined by the first phase of testing.

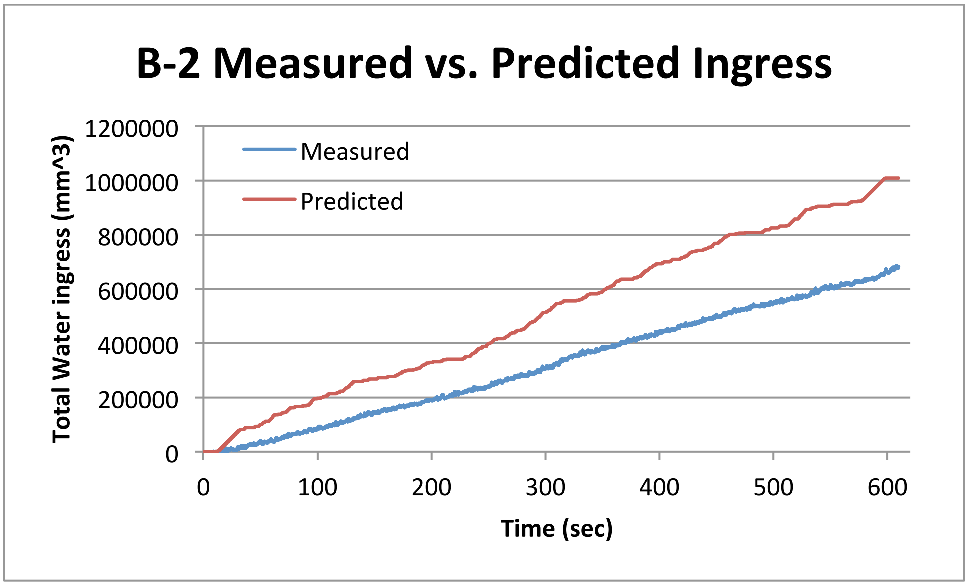

The predicted and measured average ingress rates for the target pressure sequences with multiple wetting rates are shown in the figure below. In all case, the predicted average ingress rate exceeds the measured rate. It is suspected that the over prediction results because the water is able to drain prior to the peaks in the pressure sequence, reducing the total amount of water penetration occurring. The time-step analysis consistently over estimates the measured ingress rate by 30 to 50% for the three highest wetting rates. Very little water ingress occurs at the 150 mm/hr wetting rate compared to the predicted values. The difference between measured and predicted appears to be less severe for higher wetting rates at the lowest mean pressure level.

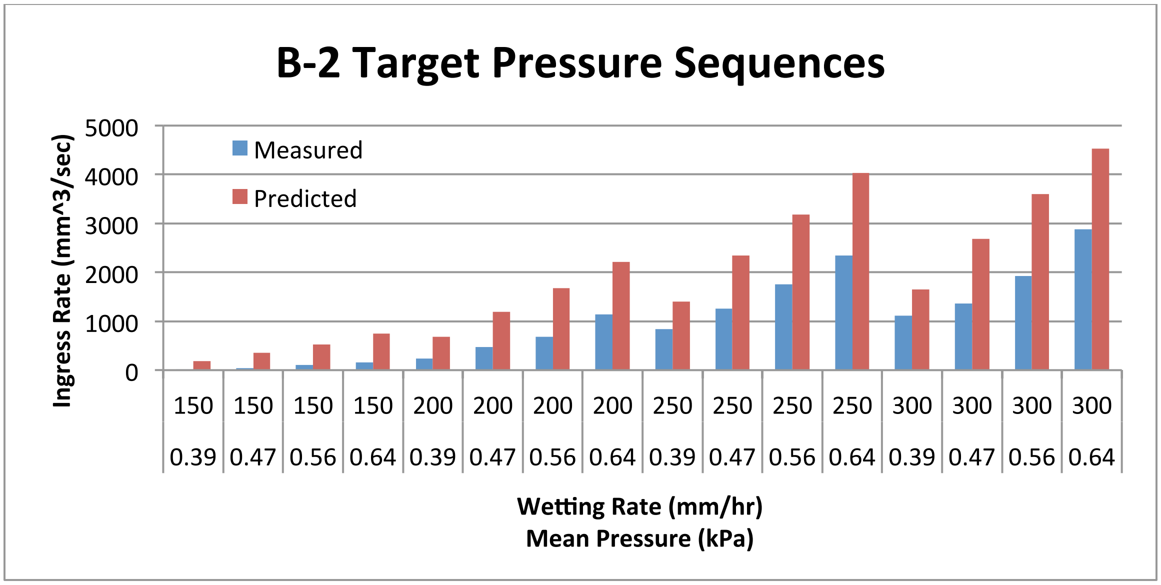

The predicted average ingress rate for the pressure sequences and wetting rates derived from Hurricane Ike are presented in the figure below for window specimen B-2. The predictions are accurate for the fourth and fifth pressure sequence, which have mean pressures of 0.21 and 0.26 kPa respectively, and wetting rates of 221 and 236 mm/hr respectively. However, the prediction for the strongest time-history with a mean pressure of 0.29 kPa and a wetting rate of 257 mm/hr severely over estimates the average water ingress rate. This is likely due to a significant amount of peaks in the pressure sequence that were of short duration, which would prevent water from accumulating and overtopping the bottom window sill. There was little or no predicted water ingress for the three weakest pressure traces, due in part to the low wetting rates, and in part because the pressure rarely exceeded the threshold for ingress during the pressure sequence.

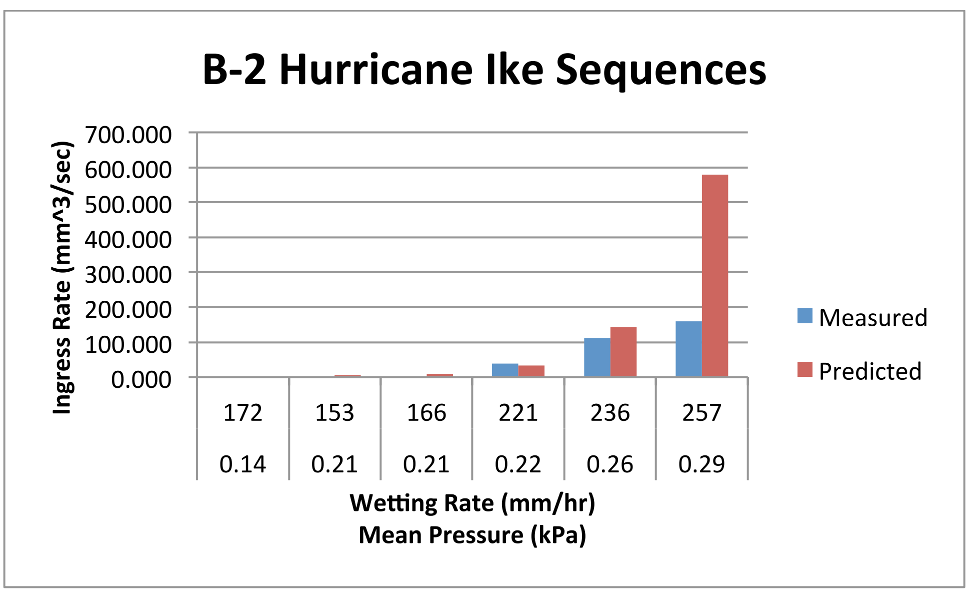

Window C-1

Initial static pressure testing for window C-1 determined that water ingress began at a static pressure of 7.5 psf. Ingress rates as a function of mean pressure and wetting rate are shown in the figure below. At the two lowest pressure levels, the water ingress rare associated with a 150 mm/hr is relatively small. At 75% of the windows design pressure, the water ingress rate due to wetting rates of 150 and 200 mm/hr are nearly identical, and slightly higher for a wetting rate of 250 mm/hr. The peak water ingress rate corresponding to the peak wetting rate and pressure is much higher than would be expected by the next closes pressures and wetting rates. The inconsistency of the general shapes of each curve with respect to water ingress would imply that the predicted water ingress rates associated with dynamic pressure sequences would be inaccurate.

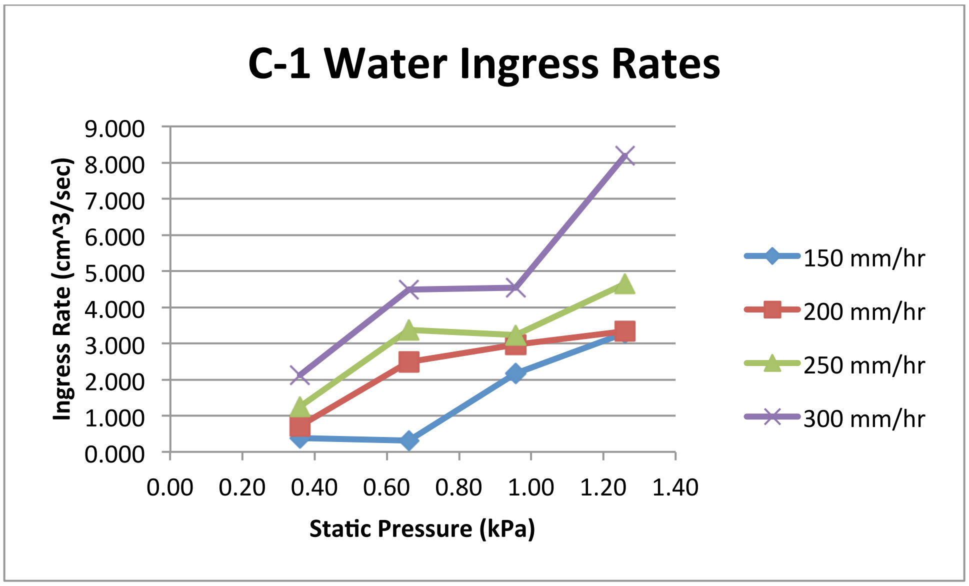

The plot shown in the figure blow presents the volume of water measured as it accumulates during the dynamic pressure sequence with a mean pressure of 0.56 kPa, and a wetting rate of 200 mm/hr. The response of the measured total ingress compared to the predicted water ingress is nearly identical until the end of the trace. There is initial lag in the actual ingress due to the time it takes for water to accumulate in the testing apparatus before accumulating in the bucket suspended from the load cell. This particular trace is an outlier for this window, as the majority of the predicted ingress rates exceeded the measured ingress rates by a considerable amount.

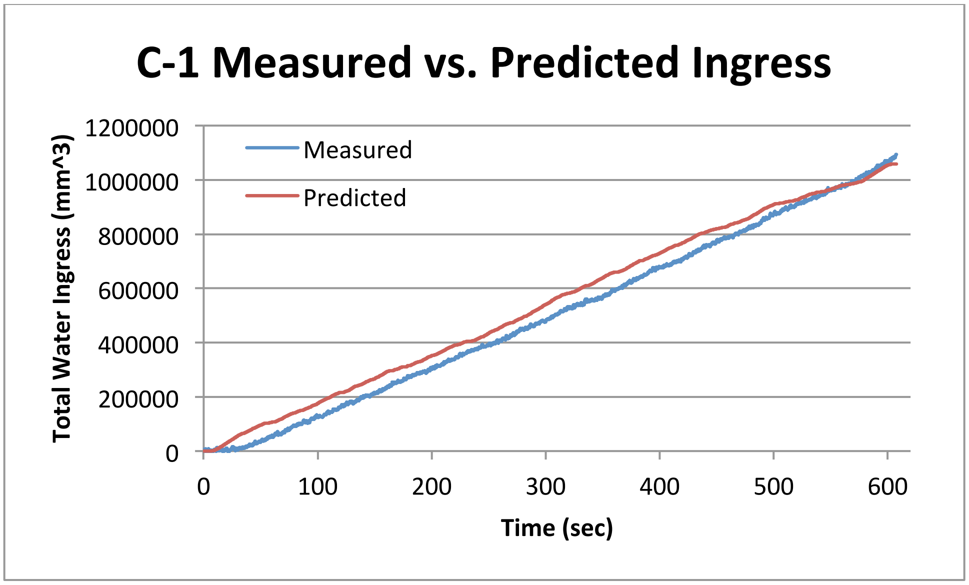

The figure below displays the predicted and measured average ingress rate for the target dynamic pressure sequences with multiple wetting rates. For this particular window, the most intense dynamic pressure sequence was not tested due to concerns of window failure. The measured ingress far exceeded the predicted ingress for wetting rates of 150 and 200 mm/hr. For wetting rates of 250 and 300 mm/hr, the predicted average ingress rates were approximately twice the actual ingress rates. The predicted and measured are nearly identical for the case of 0.56 kPa mean pressure and a wetting rate of 200 mm/hr. This case can most likely be regarded as coincidental, as the rest of the predictions are far from the measured.

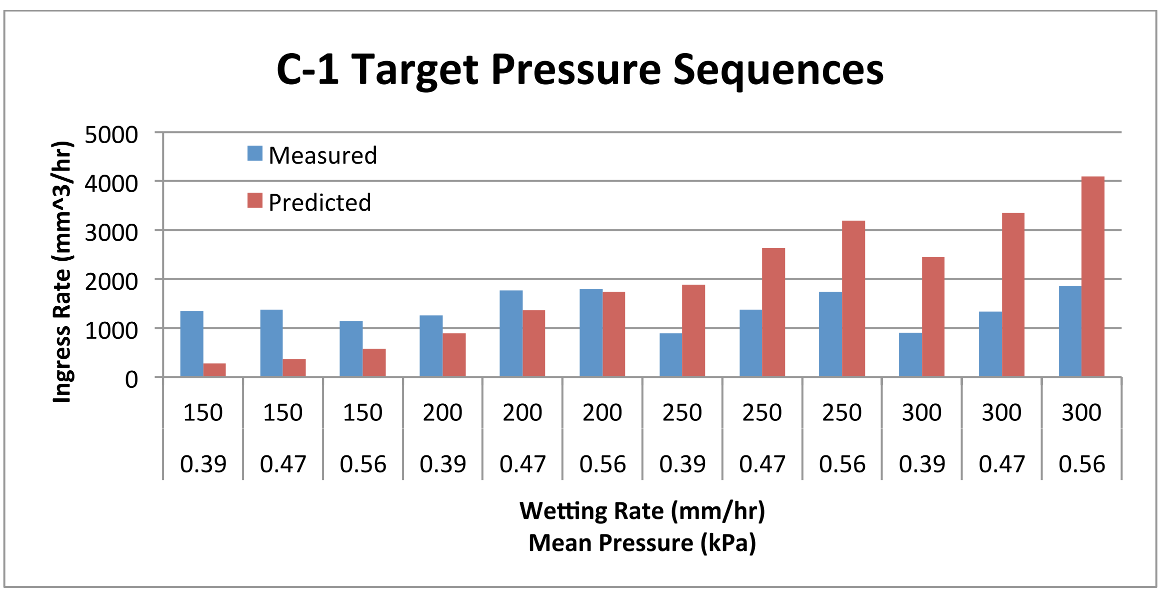

The predicted average ingress rate for the pressure sequences and wetting rates derived from Hurricane Ike are presented in the figure below for window specimen C-1. No water ingress was measured for the first five pressure sequences. A small amount of water ingress, less than a small drop per second, was measured for the strongest pressure sequence, which has a mean of 0.29 kPa, and a wetting rate of 257 mm/hr. The predicted water ingress rate for the two strongest pressure sequences was significantly higher than the actual. This is most likely due to an adequate drainage system of the window assembly, preventing water from accumulating and then penetrating when peaks were reached during the pressure sequence. The design pressure of this particular window was also higher, making ingress less likely at lower pressures.

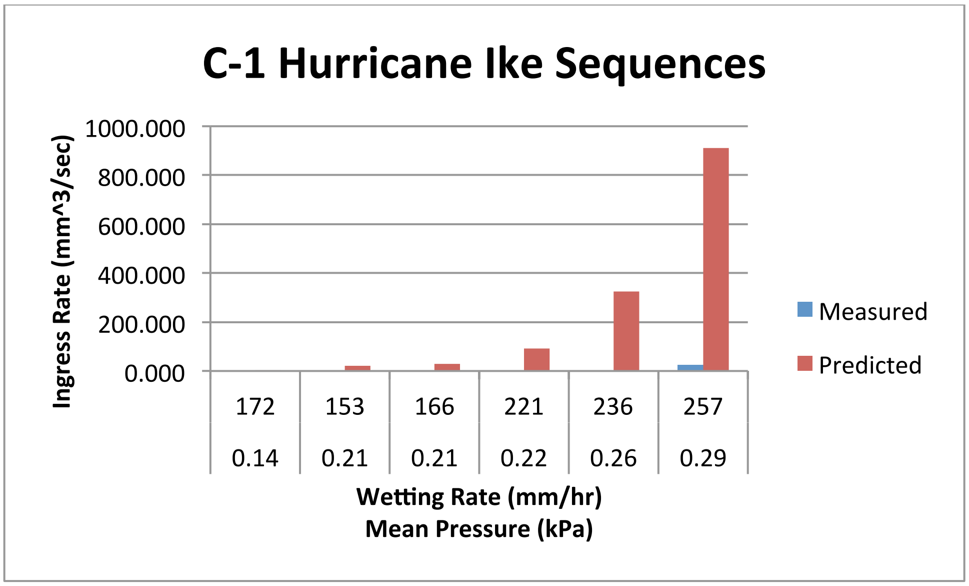

Window C-2

Ingress rates as a function of mean pressure and wetting rate are shown in the figure below for window specimen C-2. The water ingress rate for a wetting rate of 150 mm/hr is nearly zero at the lowest pressure, and slowly increases in a linear fashion. The ingress rate curves for wetting rates of 200 and 250 mm/hr are nearly identical in slope, with the magnitude of the 250 mm/hr wetting rate curve being approximately 0.6 cm^3/sec higher at each pressure level. For the lowest three pressure levels, the ingress rate curve for a wetting rate of 300 m/hr is slightly greater than the values for a wetting rate of 250 mm/hr. The peak water ingress rate corresponding to a wetting rate of 300 mm/hr and largest static pressure is much higher than would be expected compared to the adjacent static pressures and wetting rates.

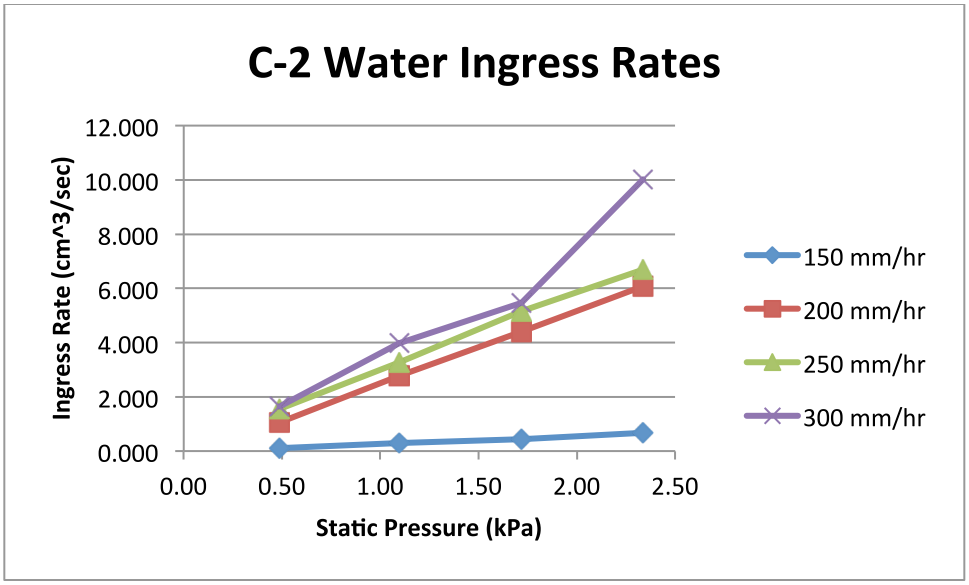

The volume of water ingress measured by the load cell versus the predicted water ingress for a mean pressure of 0.39 kPa and a wetting rate of 300 mm/hr is shown in the figure below. The threshold for water ingress for this window specimen exceeds the mean pressure of the pressure sequence, which is evident by the plateaus and peaks comprising the predicted water ingress curve. As seen with the previous window specimens, the beginning of the predicted curve is sloped steeper than the measured curve. This is partly due to the lag caused by the time it takes for the water to penetrate the window and drain to the bucket suspended from the load cell. This is also caused by the lack of water accumulation on the window sill at the beginning of the pressure sequence. At the very end of the pressure sequence, the presence of two significant peaks in can be seen by the two sharp spikes in both curves.

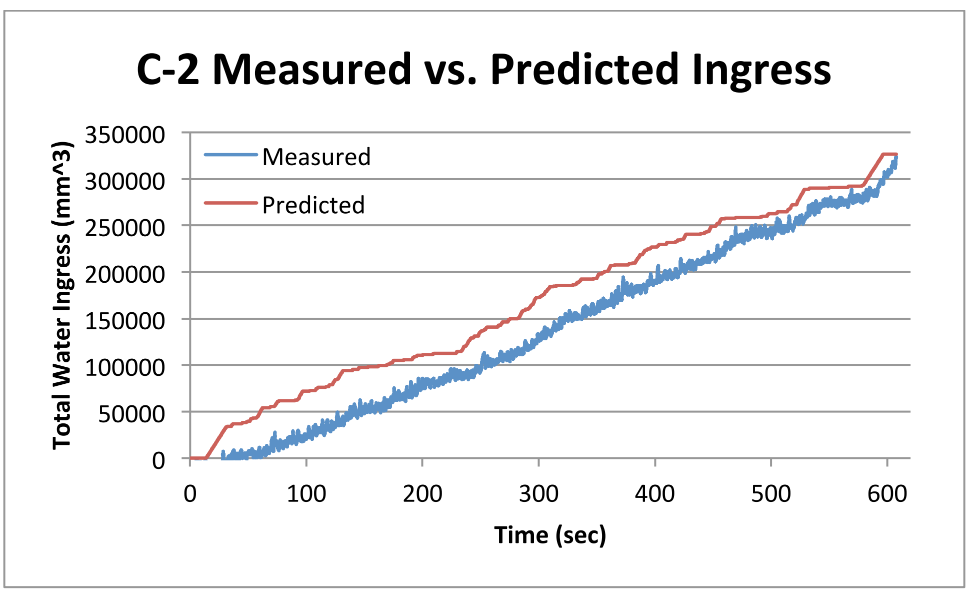

The figure below displays the predicted and measured average ingress rate for the target dynamic pressure sequences with multiple wetting rates for window specimen C-2. It can be seen from the figure that there is good agreement between the predicted and measured water ingress rates for the lowest pressure level at wetting rates of 200, 250, and 300 mm/hr. For all cases, the predicted water ingress rate exceeds the actual ingress rate. At higher pressure levels, the predicted value exceeds twice the measured. Almost no ingress was measured for a wetting rate of 150 mm/hr, which is consistent with the initial static pressure testing.

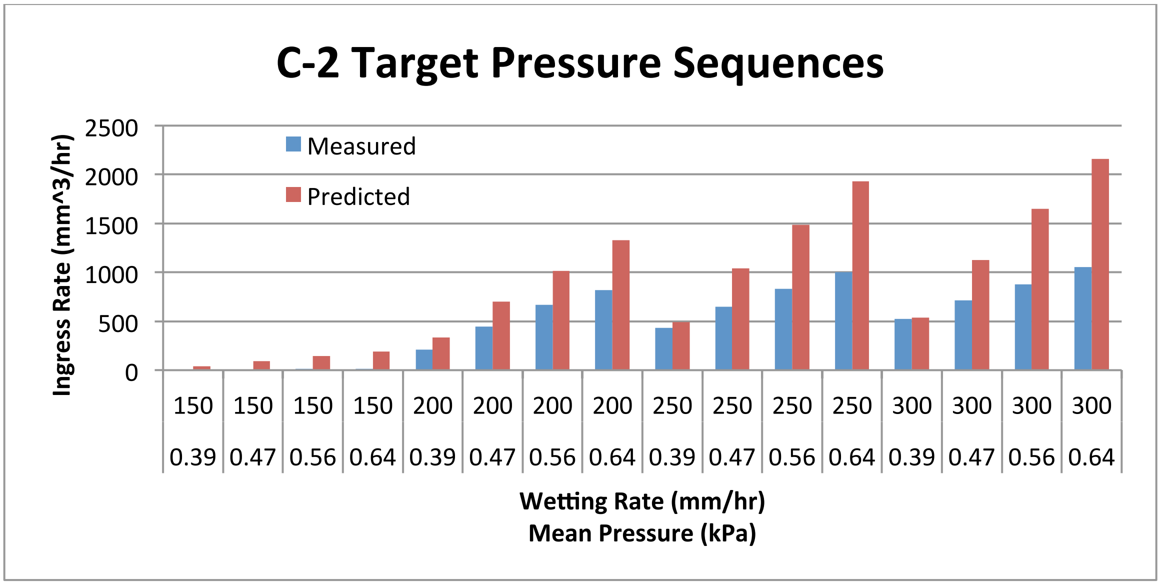

The predicted average ingress rate for the pressure sequences and wetting rates derived from Hurricane Ike are presented in the figure below. The predicted water ingress rate at the highest mean pressure level is relatively accurate, slightly exceeding the measured. For the second strongest case, the predicted is approximately twice the measured average ingress rate. Almost no water ingress was predicted for the intermediate levels, and no ingress was predicted for the lowest levels, evidence that there were no peaks in the pressure sequence that exceeded the threshold for leakage of this window.

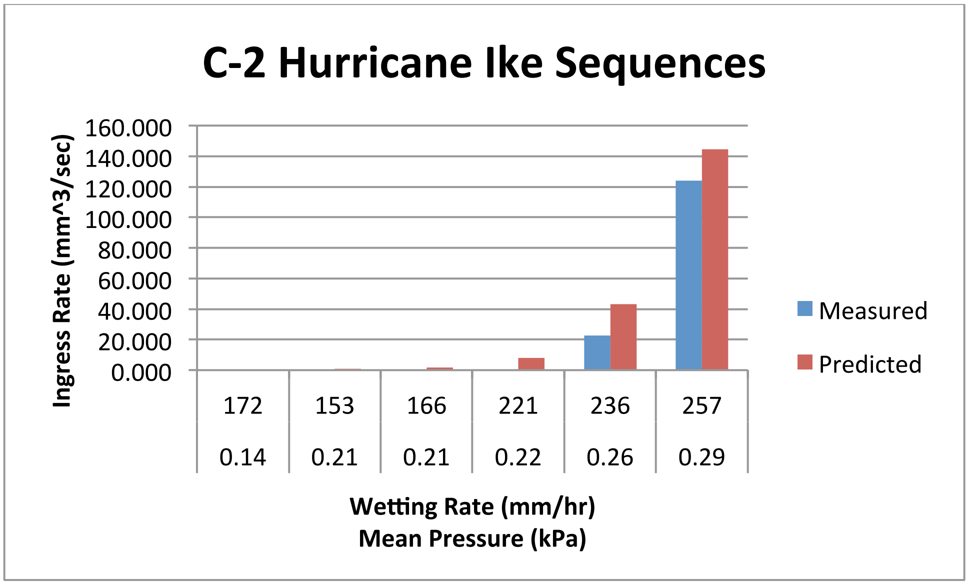

Conclusion

The underlying question this research is whether (or not) real-world performance can be predicted using simplified test methods that apply steady pressures and wetting. More specifically, is it possible to modify TAS 202-94 to predict accumulated water ingress in a real-storm? Prior research (Lopez et al., 2010) performed by the Contractor has shown that using the threshold of leakage as pass/fail criteria for water penetration resistance poorly correlates with the expected performance on a window in a real wind event.

We opted to use the relationship between the steady state pressure and water ingress as a first approximation to estimate accumulated water ingress from time-varying pressure and wetting records. The findings indicate potential for applying the steady ingress rate to calculate accumulated water ingress if the limits of detection are exceeded by a significant margin.

Moreover, this approach was conservative for all cases that were considered. Two of the four windows did not exhibit leakage where predicted for at least part of the pressure range. This difference is attributed to the time-varying nature of the applied loads. In the steady-state case, continuity of the water ingress is maintained. Under dynamic loads, water levels fluctuate. Regardless, the method appears to be generally conservative.